

**UNIVERSITÉ DU QUÉBEC**

**THÈSE PRÉSENTÉ À  
L'UNIVERSITÉ DU QUÉBEC À CHICOUTIMI  
COMME EXIGENCE PARTIELLE  
DU DOCTORAT EN INGÉNIERIE**

**PAR**

**YU-MEI HAN**

**CORROSION DES COMPOSITES À MATRICE METALLIQUE DU  
TYPE Al-B<sub>4</sub>C DANS LES SOLUTIONS AQUEUSES**

**DECEMBRE 2012**

**UNIVERSITY OF QUEBEC**

**A DISSERTATION PRESENTED TO  
THE UNIVERSITY OF QUEBEC AT CHICOUTIMI  
IN PARTIAL FULFILLMENT OF THE REQUIREMENTS FOR THE  
DOCTOR OF PHILOSOPHY IN ENGINEERING**

**BY**

**YU-MEI HAN**

**CORROSION BEHAVIOR OF Al-B<sub>4</sub>C METAL MATRIX  
COMPOSITES IN AQUEOUS SOLUTIONS**

**DECEMBER 2012**

***Dedicated to the memory of my grandpa***

## RÉSUMÉ

Au cours des dernières années, les composites à matrice métallique (CMM) du type Al-B<sub>4</sub>C ont reçu une attention considérable en raison de leur légèreté, de leur conductivité thermique supérieure, de leur grande rigidité et de leur dureté. Grâce à la capacité particulière de l'isotope B<sup>10</sup> à agir comme capteurs des neutrons, les composites Al-B<sub>4</sub>C ont été utilisés par l'industrie nucléaire à titre de matériaux absorbeurs de neutrons pour la fabrication de la section interne de contenants de transport et de stockage des combustibles nucléaires périmés.

Bien que l'incorporation de particules céramiques dans la matrice d'aluminium permet d'améliorer les propriétés physiques et mécaniques de l'alliage de base, elle peut également modifier son comportement en corrosion. En outre, en tant que matériau absorbeur de neutrons utilisé dans les contenants de transport et de stockage pour les combustibles nucléaires usés, en particulier pour les applications de stockage humide, les composites Al-B<sub>4</sub>C sont continuellement en contact avec l'eau du bassin du réacteur (l'un d'eux contenant de l'acide borique avec une concentration de B ~ 2500 ppm), un milieu généralement considéré comme étant légèrement corrosif. Ainsi, pour des raisons de sécurité évidentes, il devient très important de comprendre leur comportement en corrosion dans un milieu d'acide borique.

Cependant, à ce jour, force est de constater que très peu d'études ont été consacrées à la détermination de la tenue en corrosion des composites Al-B<sub>4</sub>C, et ce en particulier dans l'acide borique, contrairement au nombre considérable de travaux de recherche dédiés à la corrosion des composites Al-SiC et Al-Al<sub>2</sub>O<sub>3</sub> dans divers environnements. Parmi la littérature traitant des phénomènes de corrosion, les solutions 3.5% NaCl et 0.5 M K<sub>2</sub>SO<sub>4</sub> sont celles les plus couramment utilisées pour l'étude du comportement en corrosion des matériaux composites à matrice métallique. Par conséquent, la présente recherche a visé l'étude du comportement en corrosion des composites CMM du type Al-B<sub>4</sub>C dans trois solutions, soit H<sub>3</sub>BO<sub>3</sub> contenant 2500 ppm B, 3.5% NaCl et 0.5 M K<sub>2</sub>SO<sub>4</sub>.

Parmi les solutions considérées, celle de NaCl a été identifiée comme étant celle induisant le plus de dommages au composite Al-B<sub>4</sub>C suivie, dans l'ordre, des solutions de K<sub>2</sub>SO<sub>4</sub> et de H<sub>3</sub>BO<sub>3</sub>. Aucune corrosion appréciable n'a été observée dans les solutions d'acide borique et de K<sub>2</sub>SO<sub>4</sub>. Cependant, des piqûres apparentes ont été observées suite aux essais réalisés dans la solution de NaCl, et ce pour tous les matériaux étudiés. Pour l'alliage de base, le site préférentiel de piqûration était l'interface Al/Fe générée par la présence de particules intermétalliques. Pour le composite, l'interface Al/B<sub>4</sub>C était celle la plus favorable au développement de la corrosion localisée. Par ailleurs, il a été constaté que la

résistance à la corrosion des matériaux composites diminue lorsque la fraction volumique de  $B_4C$  est augmentée.

Dans le but de contrer l'agressivité des phénomènes de corrosion observés pour le CMM dans la solution de NaCl, une partie des travaux réalisés s'est intéressée à l'inhibition de la corrosion du composite dans cet environnement. À cette fin, le benzotriazole (BTAH) a été utilisé comme inhibiteur de corrosion, et son effet a été systématiquement étudié en fonction de sa concentration, de la fraction volumique des particules de  $B_4C$  et du temps d'inhibition, en utilisant la polarisation potentiodynamique, l'impédance électrochimique et la spectroscopie infrarouge de réflexion-absorption. Les résultats montrent que le BTAH est un inhibiteur efficace pour contrer la corrosion du composite Al- $B_4C$  dans une solution de 3,5 g/L NaCl, et son efficacité s'accroît lorsque sa concentration augmente. Pour une concentration de BTAH fixe et pour une même durée d'inhibition, l'augmentation de la fraction volumique de  $B_4C$  dans le composite conduit à une plus grande efficacité d'inhibition du BTAH. L'efficacité du processus d'inhibition par le benzotriazole est également influencée par la durée d'immersion dans la solution: l'efficacité d'inhibition augmente durant les 18 premières heures d'immersion, alors qu'une prolongation de la durée d'immersion entraîne une diminution de l'efficacité du BTAH. Puisque le BTAH est un inhibiteur à caractère cathodique, il agit en s'adsorbant physiquement sur les particules de  $B_4C$  à la surface du composite, lequel processus obéit à un isotherme d'adsorption de Freundlich.

Le mécanisme de corrosion dans la solution de  $K_2SO_4$  a également été étudié en utilisant la spectroscopie d'impédance électrochimique et les méthodes de polarisation potentiodynamique. La microscopie optique, la microscopie électronique à balayage, ainsi que la profilométrie ont été utilisées pour étudier la morphologie de la surface des matériaux avant et après corrosion. De plus, la spectroscopie infrarouge de réflexion-absorption et la spectroscopie de photoélectrons X ont été utilisées pour identifier les produits de corrosion. Tel que révélé par les analyses de surface, l'espèce  $SO_4^{2-}$  n'a pas induit de piqûres à la surface du composite. Puisque les particules de  $B_4C$  ont un caractère cathodique par rapport à la matrice périphérique d'aluminium, la corrosion galvanique entre les particules de  $B_4C$  et la matrice Al a été considérée comme étant le principal mécanisme de corrosion. Les spectroscopies IRRAS et XPS ont montré que la bayerite ( $Al(OH)_3$ ) est le principal produit de corrosion généré durant une immersion prolongée dans la solution de  $K_2SO_4$ .

À titre de matériaux non structuraux utilisés pour la fabrication de contenants de transport et de stockage pour les combustibles nucléaires usés, les composites AA1100- $B_4C$  sont souvent assemblés à des matériaux structuraux tels que l'alliage d'aluminium AA6061 ou l'acier inoxydable 304 (SS304). Par conséquent, les composites AA1100- $B_4C$  deviennent couplés galvaniquement aux alliages AA6061 ou SS304, ce qui peut avoir comme effet d'accélérer la corrosion du matériau le moins noble du couple. Pour cette

raison, les phénomènes de corrosion galvanique associés aux couples AA1100-B<sub>4</sub>C/AA6061 et AA1100-B<sub>4</sub>C/SS304 dans les solutions 3.5% NaCl et H<sub>3</sub>BO<sub>3</sub> contenant 2500 ppm de bore, ont été étudiés en utilisant un ampèremètre de résistance nulle (ZRA). Les effets dus à la dissimilarité des matériaux, à la solution d'immersion, et au rapport des aires des surfaces couplées galvaniquement ont été investigués. Dans la solution de NaCl, il a été déterminé que peu importe la nature du matériau structural couplé avec le CMM (SS304 ou AA6061), l'alliage de base (AA1100) ou les composites agissent toujours comme anode et les courants galvaniques mesurés sont directement proportionnels à la surface de la cathode. En revanche, dans la solution de H<sub>3</sub>BO<sub>3</sub>, les composites corrodent de façon préférentielle en présence de SS304, tandis que le AA6061 protège les composites de la dissolution. Bien que la corrosion galvanique soit contrôlée par la diffusion de l'oxygène à la cathode dans les solutions de NaCl et de H<sub>3</sub>BO<sub>3</sub>, son intensité est de loin inférieure dans la solution de H<sub>3</sub>BO<sub>3</sub>, en comparaison avec la solution de NaCl. Le contenu en B<sub>4</sub>C du composite joue également un rôle clé dans la corrosion galvanique, son influence étant modulée par la composition de la solution et les matériaux avec lesquels le composite est couplé.

Toutes les expériences ont été réalisées à température ambiante. Cependant, les composites Al-B<sub>4</sub>C sont immergés dans l'acide borique à une température élevée en situation réelle. Alors, l'auteur propose d'étudier le comportement à la corrosion des composites Al-B<sub>4</sub>C dans l'acide borique à une température élevée et d'enquêter sur la corrosion galvanique associés aux couples composites Al-B<sub>4</sub>C / SS304 et composites Al-B<sub>4</sub>C / AA6061 dans l'acide borique à une température élevée.

## ABSTRACT

In recent years, Al-B<sub>4</sub>C metal matrix composites (MMCs) have received considerable attention due to their light weight, superior thermal conductivity, high stiffness and their hardness. Owing to the special capturing neutron ability of isotope B<sup>10</sup>, Al-B<sub>4</sub>C MMCs have been increasingly used as excellent neutron absorber materials to fabricate the inside basket of transport and storage casks for spent nuclear fuels in the nuclear industry.

Although the incorporation of the ceramic particles into the Al matrix can enhance the physical and mechanical properties of the base material, it may also change its corrosion behavior. Besides, as neutron absorber material used in the spent fuels storage racks or transportation casks, especially in the wet storage application, Al-B<sub>4</sub>C MMCs are continuously in contact with the reactor pool water (*i.e.* one of them is the boric acid with B concentration of ~2500 ppm), which is generally considered to be mildly corrosive. Thus, from the safety point of view, it is of paramount importance to understand their corrosion behavior in boric acid solution.

However, up to date, very limited studies have been devoted to the corrosion behavior of the Al-B<sub>4</sub>C MMCs, especially in boric acid, in contrast to considerable research in the corrosion behavior of Al-SiC and Al-Al<sub>2</sub>O<sub>3</sub> composites in various environments. Among literature on corrosion, 3.5% NaCl and 0.5 M K<sub>2</sub>SO<sub>4</sub> are the most commonly used solutions in studying the corrosion behavior of the composites. Therefore, the present research aimed at investigating the corrosion behavior of Al-B<sub>4</sub>C MMCs in three solutions, *i.e.* 2500 ppm boron-containing H<sub>3</sub>BO<sub>3</sub> solution, 3.5% NaCl and 0.5 M K<sub>2</sub>SO<sub>4</sub>.

Al-B<sub>4</sub>C MMCs corroded most in the NaCl solution followed by K<sub>2</sub>SO<sub>4</sub> and H<sub>3</sub>BO<sub>3</sub> in order. No appreciable corrosion was observed in boric acid and sulfate solutions, while apparent pitting was observed in the NaCl solution for all materials studied. The preferential pitting sites were the Al/Fe intermetallics interfaces for the base alloy and the Al/B<sub>4</sub>C interfaces for the composites. Besides, it is observed that the corrosion resistance of the composites decreases with increase in B<sub>4</sub>C volume fraction.

The corrosion inhibition of Al-B<sub>4</sub>C MMCs in the NaCl solution was consequently investigated. Benzotriazole (BTAH) was tentatively used as a corrosion inhibitor for Al-B<sub>4</sub>C composites in the NaCl solution and its corrosion inhibition effect was systematically investigated as function of its concentration, volume fraction of B<sub>4</sub>C particles and inhibition time by using potentiodynamic polarization, electrochemical impedance and

infrared reflection adsorption spectroscopy techniques. Results show that BTAH is an efficient corrosion inhibitor for the Al-B<sub>4</sub>C MMCs in a 3.5 g/L NaCl solution, and its inhibition efficiency increased when increasing the BTAH concentration. For the same BTAH concentration and immersion time, higher B<sub>4</sub>C volume fraction leads to higher corrosion inhibition efficiency. The inhibition efficiency of benzotriazole was also influenced by the inhibition time: The inhibition efficiency increases with the immersion time in the first 18 hours. However, prolonging the immersion time leads to a decrease in the inhibition efficiency. As BTAH was an inhibitor with a cathodic character, it inhibited corrosion by physically adsorbing on B<sub>4</sub>C particles at the composite surface, which obeyed the Freundlich adsorption isotherm.

The corrosion mechanism in K<sub>2</sub>SO<sub>4</sub> solution was also studied by employing electrochemical impedance spectroscopy and potentiodynamic polarization methods. Optical and scanning electron microscopes as well as profilometry were employed to study the surface morphology of the material before and after corrosion. Moreover, infrared reflection-absorption spectroscopy (IRRAS) and x-ray photoelectron spectroscopy (XPS) were used to identify the corrosion products. SO<sub>4</sub><sup>2-</sup> species did not induce pitting of the AA1100-16 vol. % B<sub>4</sub>C. Since B<sub>4</sub>C particles showed a cathodic character with respect to the peripheral matrix, therefore, the galvanic corrosion between B<sub>4</sub>C particles and the Al matrix was considered to be the premier corrosion mechanism. IRRAS and XPS results showed that bayerite Al(OH)<sub>3</sub> was the principal corrosion product.

As non-structural neutron absorber materials used to fabricate the inside basket of spent fuel storage racks or transportation casks, AA1100-B<sub>4</sub>C MMCs are often assembled to structural materials AA6061 or SS304. Consequently, the AA1100-B<sub>4</sub>C MMCs are galvanically coupled to AA6061 or SS304, which could potentially accelerate the corrosion of the less noble material. Therefore, the galvanic corrosion associated with AA1100-B<sub>4</sub>C MMCs/AA6061 and AA1100-B<sub>4</sub>C MMCs/SS304 couples in 3.5% NaCl and 2500 ppm boron-containing H<sub>3</sub>BO<sub>3</sub> solutions was investigated by using a zero resistance ammeter (ZRA). The effects of dissimilar materials, immersion solution, and ratio of the coupled material areas are reported. In the NaCl solution, depending on the nature of the coupling agent (SS304 or AA6061), the composite or base alloy always acts as an anode and the measured galvanic currents are directly proportional to the cathode area. In contrast, in the H<sub>3</sub>BO<sub>3</sub> solution, the composites preferentially dissolve in the presence of SS304, while AA6061 protects the metal matrix composites from dissolution. Although galvanic corrosion is controlled by oxygen diffusion at the cathode in both NaCl and H<sub>3</sub>BO<sub>3</sub> solutions, its intensity is appreciably lower in the H<sub>3</sub>BO<sub>3</sub> solution in comparison with the NaCl solution. The B<sub>4</sub>C content is also found to play a key role in galvanic corrosion; its influence is modulated by the solution composition and the materials to which the composite is galvanically coupled.

Above all experiments were carried out in room temperature. However, Al-B<sub>4</sub>C composites are immersed in boric acid at elevated temperature in the real situation. In the future work, the author suggests to studying the corrosion behavior of Al-B<sub>4</sub>C composites in boric acid at elevated temperature and investigating the galvanic corrosion associated with Al-B<sub>4</sub>C MMCs/SS304 and Al-B<sub>4</sub>C MMCs/AA6061 couples in boric acid at elevated temperature.

## PUBLICATIONS

### *Journal articles and conference paper*

1. Y. Han, D. Gallant and X-G. Chen, “*Investigation on Corrosion Behavior of the Al-B<sub>4</sub>C Metal Matrix Composite in a Mildly Oxidizing Aqueous Environment*”, *Corrosion*, 67(2011), No.115005.
2. Y.-M. Han, D. Gallant and X-G. Chen, *Corrosion Behaviour of Al-B<sub>4</sub>C Metal Matrix Composites in H<sub>3</sub>BO<sub>3</sub>, K<sub>2</sub>SO<sub>4</sub> and NaCl Solutions*, *Proceedings of the Light Metal , MetSoc*, 2011, pp. 415-425.
3. Y.M. Han, D. Gallant and X-G. Chen, “*Galvanic corrosion associated with Al-B<sub>4</sub>C composites/6061 and Al-B<sub>4</sub>C composites/SS304 couples in NaCl and H<sub>3</sub>BO<sub>3</sub> solutions*”, accepted by *Electrochim. Acta.*, 2012.
4. Y.-M. Han, D. Gallant and X-G. Chen, “*Corrosion Inhibition of Al-B<sub>4</sub>C Metal Matrix Composites in NaCl Solution by Benzotriazole (BTA)*”, accepted by *Mater. Chem. Phys.*, 2012.
5. Y.-M. Han, D. Gallant and X-G. Chen, “*Corrosion Characterization of Al-B<sub>4</sub>C Metal Matrix Composites in NaCl Solution*”, submitted to *Electrochim. Acta.*, 2012, in revision.
6. Y.-M. Han, D. Gallant and X-G. Chen, *Corrosion Characterization of Al-B<sub>4</sub>C Metal Matrix Composites in H<sub>3</sub>BO<sub>3</sub> Solutions*, submitted to *Corros. Sci.*, 2012, in revision.

### *Scientific posters*

7. Y.M. Han, D. Gallant and X.-G. Chen, *Galvanic corrosion associated with Al-B<sub>4</sub>C/AA6061 and Al-B<sub>4</sub>C/SS304 couples in NaCl solution*, the *Encyclopedia of Research on Aluminum in Quebec*, Les Presses de l’aluminium (PRAL), Trois-Riviere, 2012.
8. Y.M. Han, D. Gallant and X.-G. Chen, *Inhibition by Benzotriazole of Al-B<sub>4</sub>C Metal Matrix Composites Corrosion in NaCl Solution*, the *Encyclopedia of Research on Aluminum in Quebec*, Les Presses de l’aluminium (PRAL), Montreal, 2011.
9. Y.M. Han, D. Gallant, B. Arsenault and X.-G. Chen, *Investigation on Corrosion Behavior of Al-B<sub>4</sub>C Metal Matrix Composite in a Mildly Oxidizing Aqueous Environment*, the *Encyclopedia of Research on Aluminium in Quebec*, Les Presses de l’aluminium (PRAL), Quebec, 2010.
10. Y.M. Han, D. Gallant, B. Arsenault and X.-G. Chen, *Corrosion Mechanisms of Al-B<sub>4</sub>C Metal Matrix Composites in Sulfate Solution*, the *Encyclopedia of Research on Aluminum in Quebec*, Les Presses de l’aluminium (PRAL), Montreal, 2009.

## ACKNOWLEDGEMENTS

It is a great pleasure to have the chance to convey my thanks to all those who were involved, directly or indirectly, in making this project a success. First and foremost, I would like to express my special thanks to my director, Professor X.-Grant Chen and co-director, Dr. Danick Gallant, for giving me the opportunity to undertake this research, for their expertise guidance, continuous encouragement, and patience during my Ph. D study. Without them, I wouldn't have come so far.

I would like to express my appreciation to all members of Natural Research Council Canada (NRC)-Saguenay site for creating such a comfortable studying and experimental environment during my five years of research. Particularly, I would like to express my profound gratitude to Ms. Amélie Ruest, Ms. Sandy Laplante, Ms. Geneviève Simard and Ms. Hélène Grégoire, not only for their professional technical assistance during experiments, but also for the happy time that they shared with me. I would also like to thank Mr. Bernard Arsenault, the director of NRC-Saguenay site, who introduced me to NRC-Saguenay site and gave generous encouragement in my research work. Many thanks also go to Mr. Stephan Simard, Mr. Mojtaba Eskandarian and Ms. Saleema Noormohammed.

I am grateful for all members of NESERC Industry Chair in Metallurgy of Innovative Aluminum Transformation at the University of Quebec in Chicoutimi, for

stimulating discussions at the half-month meetings and all the fun that we have had during the last five year.

I wish to express my grateful acknowledgement to the financial support from the Natural Sciences and Engineering Research Council of Canada (NSERC), from Rio Tinto Alcan and from the Natural Research Council Canada (Saguenay site) through the NSERC Industrial Research Chair in Metallurgy of Innovative Aluminium Transformation at the University of Quebec in Chicoutimi.

Finally, my endless thanks go to my beloved parents, grandparents, brother and husband for their love and immense support-both spiritually and practically. I also would like to thank my son for all the laughs gifted to me.

## TABLE OF CONTENTS

|  |             |
|--|-------------|
| <b>RESUMÉ .....</b>  | <b>i</b>    |
| <b>ABSTRACT.....</b>   | <b>iv</b>   |
| <b>PUBLICATIONS.....</b>   | <b>vii</b>  |
| <b>ACKNOWLEDGEMENTS .....</b>  | <b>viii</b> |
| <b>TABLE OF CONTENTS .....</b>   | <b>x</b>    |
| <b>LIST OF TABLES.....</b>   | <b>xv</b>   |
| <b>LIST OF FIGURES.....</b>  | <b>xvii</b> |
| <br>   |             |
| <b>CHAPTER 1</b>   |             |
| <b>INTRODUCTION .....</b>  | <b>1</b>    |
| 1.1 Definition of the Problem.....   | 2           |
| 1.2 Objectives.....  | 5           |
| References.....  | 6           |
| <br>   |             |
| <b>CHAPTER 2</b>   |             |
| <b>LITERATURE REVIEW .....</b>   | <b>8</b>    |
| 2.1 Al-B <sub>4</sub> C Composites.....  | 9           |
| 2.1.1 Fabrication Process of Al-B <sub>4</sub> C MMCs.....                         | 11          |
| 2.1.2 Interfacial Reactions Between Al matrix and B <sub>4</sub> C Composites..... | 13          |

|       |   |    |
|-------|---|----|
| 2.1.3 | Applications of Al-B <sub>4</sub> C MMCs in the Nuclear Industry.....                       | 15 |
| 2.2   | Forms of Corrosion .....  | 19 |
| 2.3   | Corrosion of Aluminum Metal Matrix Composites .....   | 23 |
| 2.4   | Galvanic Corrosion of Metal Matrix Composites Associated With Dissimilar<br>Materials ..... | 27 |
| 2.5   | Corrosion Prevention.....   | 28 |
| 2.6   | Basic Aspects of Electrochemical Processes .....  | 32 |
| 2.6.1 | Electrical Double Layer .....   | 32 |
| 2.6.2 | Three-Electrode Cell.....   | 34 |
| 2.7   | Corrosion testing and evaluation techniques.....  | 35 |
| 2.7.1 | Potentiodynamic Polarization .....  | 37 |
| 2.7.2 | Electrochemical Impedance Spectroscopy (EIS).....   | 40 |
| 2.7.3 | Zero Resistance Ammetry.....  | 48 |
|       | References.....   | 49 |

### CHAPTER 3

|                                      |   |    |
|--------------------------------------|---|----|
| <b>EXPERIMENTAL PROCEDURES .....</b> | <b>55</b>   |    |
| 3.1                                  | Sample Preparation and Solutions.....             | 56 |
| 3.2                                  | Electrochemical Experiments.....                  | 59 |
| 3.3                                  | Microstructural Analysis .....                    | 60 |
| 3.4                                  | Infrared Reflection-Absorption Spectroscopy ..... | 61 |
| 3.5                                  | X-Ray Photoelectron Spectroscopy .....            | 61 |
|                                      | References.....                                   | 61 |

### CHAPTER 4

|   |           |
|---|-----------|
| <b>CORROSION BEHAVIOUR OF Al-B<sub>4</sub>C METAL MATRIX COMPOSITES IN<br/>H<sub>3</sub>BO<sub>3</sub>, K<sub>2</sub>SO<sub>4</sub> AND NaCl SOLUTIONS.....</b> | <b>62</b> |
|---|-----------|

|   |    |
|---|----|
| Abstract.....                                     | 63 |
| 4.1 Introduction.....                             | 64 |
| 4.2 Materials and Methods.....                    | 65 |
| 4.3 Results and Discussion.....                   | 67 |
| 4.3.1 Potentiodynamic Polarization.....           | 67 |
| 4.3.2 Electrochemical Impedance Spectroscopy..... | 72 |
| 4.4 Conclusions.....                              | 77 |
| References.....                                   | 78 |

## CHAPTER 5

### INVESTIGATION ON CORROSION BEHAVIOR OF THE Al-B<sub>4</sub>C METAL MATRIX COMPOSITES IN A MILDLY OXIDIZING AQUEOUS ENVIRONMENT..... 81

|   |     |
|---|-----|
| Abstract.....   | 82  |
| 5.1 Introduction.....   | 83  |
| 5.2 Experimental Procedure.....   | 85  |
| 5.2.1 Material Preparation.....   | 85  |
| 5.2.2 Electrochemical Experiments.....  | 86  |
| 5.2.3 Microstructural Analysis.....   | 88  |
| 5.2.4 Infrared Reflection-Absorption Spectroscopy.....  | 88  |
| 5.2.5 X-Ray Photoelectron Spectroscopy.....   | 89  |
| 5.3 Results and Discussion.....   | 89  |
| 5.3.1 Potentiodynamic Polarization of Al-B <sub>4</sub> C MMC in K <sub>2</sub> SO <sub>4</sub> and NaCl Solutions.....             | 89  |
| 5.3.2 Electrochemical Impedance Spectroscopy Investigation of Al-B <sub>4</sub> C MMC in 0.5 M K <sub>2</sub> SO <sub>4</sub> ..... | 93  |
| 5.3.3 Morphology and Characterization of Corrosion Products.....  | 101 |

|     |                   |     |
|-----|-------------------|-----|
| 5.4 | Conclusions ..... | 110 |
|     | References.....   | 111 |

## **CHAPTER 6**

### **CORROSION INHIBITION OF Al-B<sub>4</sub>C METAL MATRIX COMPOSITES IN A NaCl SOLUTION BY BENZOTRIAZOLE .....**

|       |   |     |
|-------|---|-----|
|       | Abstract.....   | 115 |
| 6.1   | Introduction .....  | 116 |
| 6.2   | Experimental Procedures.....  | 118 |
| 6.2.1 | Preparation of Samples and Electrolytes .....   | 118 |
| 6.2.2 | Electrochemical Measurements .....  | 119 |
| 6.2.3 | Infrared Reflection-Absorption Spectroscopy .....                                     | 120 |
| 6.3   | Results and Discussion.....   | 120 |
| 6.3.1 | Effect of BTAH on the Inhibition Efficiency .....                                     | 120 |
| 6.3.2 | Effect of B <sub>4</sub> C Particle Volume Fraction on The inhibition Efficiency..... | 124 |
| 6.3.3 | Effect of Immersion Time.....   | 128 |
| 6.3.4 | Electrochemical Impedance Spectroscopy (EIS) Measurements.....                        | 131 |
| 6.3.5 | Infrared Reflection Absorption Spectroscopy (IRRAS) .....                             | 135 |
| 6.3.6 | Adsorption Isotherm .....   | 137 |
| 6.4   | Conclusions .....   | 139 |
|       | References.....   | 140 |

## **CHAPTER 7**

### **GALVANIC CORROSION ASSOCIATED WITH Al-B<sub>4</sub>C COMPOSITES/SS304 AND Al-B<sub>4</sub>C COMPOSITES/AA6061 COUPLES IN NaCl AND H<sub>3</sub>BO<sub>3</sub> SOLUTIONS.....**

|   |     |
|---|-----|
| Abstract.....   | 145 |
| 7.1 Introduction.....                                     | 146 |
| 7.2 Experimental Procedure.....                           | 147 |
| 7.2.1 Sample Preparation.....                             | 147 |
| 7.2.2 Galvanic Coupling Measurement.....                  | 148 |
| 7.3 Results and Discussion.....                           | 149 |
| 7.3.1 Open Circuit Potentials of Uncoupled Materials..... | 149 |
| 7.3.2 Effect of Dissimilar Materials.....                 | 151 |
| 7.3.3 Effect of Solution.....                             | 155 |
| 7.3.4 Effect of Area Ratio.....                           | 160 |
| 7.4 Conclusions.....                                      | 170 |
| References.....   | 171 |

## **CHAPTER 8**

### **CONCLUSIONS & RECOMMENDATIONS FOR FUTURE WORK..... 173**

|   |     |
|---|-----|
| 8.1 Conclusions.....                      | 174 |
| 8.2 Recommendations for Future Works..... | 177 |

## LIST OF TABLES

|           |   |     |
|-----------|---|-----|
| Table 2.1 | Typical composition of AA1100-B <sub>4</sub> C composites.....  | 11  |
| Table 3.1 | Designate chemical composition of the base alloy AA1100.....  | 57  |
| Table 4.1 | Chemical composition of the base alloy AA1100.....  | 66  |
| Table 4.2 | Electrochemical parameters derived from polarization curves. ....   | 70  |
| Table 5.1 | Typical chemical composition of AA 1100 – 15 wt. % B <sub>4</sub> C composite.....  | 86  |
| Table 5.2 | Corrosion parameters calculated from polarization curves. ....  | 91  |
| Table 5.3 | Electrochemical parameters calculated from the equivalent circuit in Figure 5.7.....  | 97  |
| Table 5.4 | Electrochemical parameters calculated from the equivalent circuit in Figure 5.9.....  | 99  |
| Table 6.1 | Designated chemical composition of the base AA1100 alloy.....   | 118 |
| Table 6.2 | Electrochemical parameters obtained from PDP measurements of AA1100-16 vol.% B <sub>4</sub> C in 3.5 g/L NaCl with different concentrations of BTAH. ....   | 123 |
| Table 6.3 | Electrochemical parameters obtained from PDP measurements of AA1100, AA1100-16 vol.% B <sub>4</sub> C, and AA1100-30 vol.% B <sub>4</sub> C in a 3.5 g/L NaCl solution in the presence and absence of 0.05M of BTAH. .... | 127 |
| Table 6.4 | Electrochemical parameters obtained from PDP measurement of AA1100-16 vol.% B <sub>4</sub> C in a 3.5 g/L NaCl solution with different immersion times. ....  | 130 |
| Table 6.5 | Electrochemical parameters obtained from PDP measurement of AA1100-16 vol.% B <sub>4</sub> C in a 3.5 g/L NaCl + 0.05M of BTAH solution with different immersion times. ....  | 130 |
| Table 6.6 | Electrochemical parameters obtained from EIS measurements of Al composites in a 0.35 % NaCl solution with different BTAH concentrations.....  | 134 |
| Table 7.1 | Chemical composition of the base alloy AA1100.....  | 148 |
| Table 7.2 | Open circuit potential ( $\varphi_{ocp}$ ) of materials investigated in 3.5% NaCl   |     |

|           |   |     |
|-----------|---|-----|
|           | and 2500 ppm B-containing $\text{H}_3\text{BO}_3$ solutions.....  | 150 |
| Table 7.3 | Average galvanic current $\overline{I}_g$ of different couples and potential difference $\Delta\phi^S$ of uncoupled dissimilar material in 3.5% NaCl solution.....                                      | 154 |
| Table 7.4 | Average galvanic current $\overline{I}_g$ of different couples and potential difference $\Delta\phi^S$ of uncoupled dissimilar materials in 2500 ppm B-containing $\text{H}_3\text{BO}_3$ solution..... | 159 |

## LIST OF FIGURES

|             |   |    |
|-------------|---|----|
| Figure 2.1  | Classification of composite materials with metal matrixes.....  | 9  |
| Figure 2.2  | Schematic diagram showing three types of metal matrix component materials. ....   | 10 |
| Figure 2.3  | General steps in the powder metallurgy process. <sup>[8]</sup> .....  | 12 |
| Figure 2.4  | General steps in liquid mixing process.....   | 13 |
| Figure 2.5  | (a) Microstructure of AA1100-15 vol.% B <sub>4</sub> C and (b) Ti Mapping showing the Ti barrier layer at B <sub>4</sub> C and matrix interfaces. ....  | 15 |
| Figure 2.6  | Optical micrographs showing (a) large clusters of secondary phases and (b) the uniform distribution of boron carbide in the matrix with the addition of Ti in AA6351-15 vol. % B <sub>4</sub> C composite obtained after 30 min processing time. .... | 15 |
| Figure 2.7  | Spent nuclear fuel wet storage pool. ....   | 16 |
| Figure 2.8  | Cross section of a typical PWR storage cell. ....   | 17 |
| Figure 2.9  | Multiple purpose canister of dry storage. ....  | 18 |
| Figure 2.10 | Schematic diagram showing the uniform corrosion.....  | 19 |
| Figure 2.11 | Schematic diagram showing the galvanic corrosion. ....  | 20 |
| Figure 2.12 | Schematic diagram showing the pitting corrosion. ....   | 20 |
| Figure 2.13 | Schematic diagram showing the crevice corrosion. ....   | 21 |
| Figure 2.14 | Schematic diagram showing stress corrosion cracking .....   | 21 |
| Figure 2.15 | Schematic diagram showing intergranular corrosion.....  | 22 |
| Figure 2.16 | Schematic diagram showing selective corrosion.....  | 22 |
| Figure 2.17 | Schematic diagram showing erosion corrosion.....  | 23 |
| Figure 2.18 | Scanning electron micrographs of samples corroded in sea water at 300 K (a) base alloy (6061 A1) and (b) as-cast composite. ....  | 24 |
| Figure 2.19 | Schematic diagram showing the microstructure (a) 7075-SiCp MMC and (b) 7075 alloy. <sup>1</sup> .....   | 26 |
| Figure 2.20 | Chemical structure of BTAH. ....  | 32 |
| Figure 2.21 | Proposed model of the double-layer region under conditions where anions specially adsorbed.....   | 33 |
| Figure 2.22 | Three-electrode cell and notation for the difference electrodes. ....   | 34 |

|             |   |    |
|-------------|---|----|
| Figure 2.23 | Theoretical anodic polarization scan. ....  | 38 |
| Figure 2.24 | Potentiodynamic polarisation diagrams for C/AS41 and C/AS41(0.5% Ca) Mg MMCs in 100 ppm NaCl solution, pH 12. <sup>[26]</sup> .....   | 39 |
| Figure 2.25 | Tafel slope calculation.....  | 40 |
| Figure 2.26 | Sinusoidal current response in a linear system.....   | 42 |
| Figure 2.27 | (a) Nyquist and (b) Bode plot for the Randle cell. ....   | 43 |
| Figure 2.28 | Simple equivalent circuit with one time constant. ....  | 44 |
| Figure 2.29 | Nyquist plot showing the ideal semicircle (curve 1, $\alpha=1.0$ ) and depressed semicircle (curve 2, $\alpha=0.8$ ).....   | 45 |
| Figure 2.30 | Nyquist plot of Al/0.16M $\text{NH}_4^+$ tartrate at (a) $\text{P}^{\text{H}} = 6$ and $T = 298\text{K}$ with electrode potentials: - 670 mV ( $\square$ ); - 470 mV ( $\Delta$ ); - 270 mV ( $\diamond$ ); - 70 mV ( $\bullet$ ); + 330 mV ( $\circ$ ); (b) $T = 298\text{K}$ , $E = 330\text{ mV}$ , $\text{P}^{\text{H}} = 5$ ( $\circ$ ); 6 ( $\Delta$ ); 7( $\square$ )..... | 46 |
| Figure 2.31 | Equivalent circuit used to interpret the Nyquist plot in Figure 2.30. ....  | 46 |
| Figure 2.32 | (a) Equivalent circuit for the total electrode impedance; (b) Nyquist plot for the circuit in (a) when $1/\text{CR}_3 < \text{R}_2/\text{L}$ . ....   | 47 |
| Figure 3.1  | EG&G PAR flat cell used in the present study and the three-electrode system. ....   | 60 |
| Figure 3.2  | Image of scanning electron microscope used in the present study.....  | 60 |
| Figure 4.1  | Potentiodynamic polarization curves recorded on AA1100-16 vol. % $\text{B}_4\text{C}$ in 2500 ppm boron-containing $\text{H}_3\text{BO}_3$ , 0.5 M $\text{K}_2\text{SO}_4$ and 3.5% NaCl. ....  | 68 |
| Figure 4.2  | Potentiodynamic polarization curves recorded on AA1100-30 vol. % $\text{B}_4\text{C}$ in 2500 ppm boron-containing $\text{H}_3\text{BO}_3$ , 0.5 M $\text{K}_2\text{SO}_4$ and 3.5% NaCl. ....  | 69 |
| Figure 4.3  | Potentiodynamic polarization curves recorded on base alloy AA1100 in 2500 ppm boron-containing $\text{H}_3\text{BO}_3$ , 0.5 M $\text{K}_2\text{SO}_4$ and 3.5% NaCl. ....  | 70 |
| Figure 4.4  | Tafel plot of AA1100-16 vol. % $\text{B}_4\text{C}$ in 0.5 M $\text{K}_2\text{SO}_4$ showing that $j_{\text{corr}}$ value is obtained by the intersection of the extrapolated cathodic branch at the corrosion potential. ....  | 71 |
| Figure 4.5  | SEM image presenting the surface morphology of AA1100-16 vol. % $\text{B}_4\text{C}$ (a) before and (b) after polarization in 3.5% NaCl. Initiation of pitting (marked as black arrows) is observed at the Al/ $\text{B}_4\text{C}$ interfaces after being polarized to $1\text{ mA}\cdot\text{cm}^{-2}$ . ....   | 72 |

|             |   |    |
|-------------|---|----|
| Figure 4.6  | SEM image presenting the surface morphology of AA1100 alloy (a) before and (b) after polarization in 3.5% NaCl. Initiation of pitting (marked as black arrows) at Al/intermetallic phase is observed after polarization. EDS result shows that the intermetallic is Fe-containing phases. ....  | 72 |
| Figure 4.7  | Typical Bode plots of AA1100, -16 vol. % B <sub>4</sub> C and -30 vol. % B <sub>4</sub> C composites obtained after a 3-hour immersion in 2500 ppm B-containing H <sub>3</sub> BO <sub>3</sub> solution. ....   | 74 |
| Figure 4.8  | Typical Bode plots of AA1100, -16 vol. % B <sub>4</sub> C and -30 vol. % B <sub>4</sub> C composites obtained after a 1-hour immersion in 0.5 M K <sub>2</sub> SO <sub>4</sub> solution. ....   | 74 |
| Figure 4.9  | Typical Bode plots of AA1100, AA1100-16 vol. % B <sub>4</sub> C and AA1100-30 vol. % B <sub>4</sub> C obtained after a 1-hour immersion in 3.5% NaCl solution. ....   | 75 |
| Figure 4.10 | Average impedances measured in three solutions in the frequency range 0.01 ~ 0.04 Hz as a function of B <sub>4</sub> C percent in the MMCs. ....  | 75 |
| Figure 4.11 | Damage function as function of B <sub>4</sub> C percent for materials investigated in 2500 ppm B-containing H <sub>3</sub> BO <sub>3</sub> , 0.5 M K <sub>2</sub> SO <sub>4</sub> and 3.5% NaCl solutions. ....   | 77 |
| Figure 5.1  | Typical potentiodynamic polarization curve of AA1100-16 vol. % B <sub>4</sub> C composite in a 0.5 M K <sub>2</sub> SO <sub>4</sub> solution after a 3-hour immersion period. (Inset: Tafel plot showing the corrosion current $j$ was obtained at the intercept of the extrapolation of cathodic branch. $j_{\text{corr}} = 74 \text{ nA.cm}^{-2}$ , $E_{\text{corr}} = -400.7 \text{ mV}$ ). .... | 90 |
| Figure 5.2  | Typical potentiodynamic polarization curve of AA1100-16 vol. % B <sub>4</sub> C composite in a 3.5% NaCl solution after a 3-hour immersion period. (Inset: Tafel plot showing the corrosion current $j_{\text{corr}}$ was obtained at the intercept of the extrapolation of cathodic branch. $j_{\text{corr}} = 11.50 \text{ }\mu\text{A.cm}^{-2}$ , $E_{\text{corr}} = -595.5 \text{ mV}$ ). ....  | 90 |
| Figure 5.3  | SEM image comparing the surface morphology of the composite (a) before and (b) after polarization in a 0.5 M K <sub>2</sub> SO <sub>4</sub> solution. ....  | 92 |
| Figure 5.4  | SEM image presenting the occurrence of pitting at the interface of Al/B <sub>4</sub> C particles on an AA1100-16 vol. % B <sub>4</sub> C MMC surface during polarization in a 3.5% NaCl solution. ....  | 93 |
| Figure 5.5  | Optical micrographs showing (a) uniform B <sub>4</sub> C particle distribution and (b) defects on an AA1100-16 vol. % B <sub>4</sub> C MMC surface; topographic profile of (c) uniform surface and (d) defective surface. ....  | 94 |
| Figure 5.6  | Typical (a) Nyquist and (b) Bode plots of AA1100-16 vol. % B <sub>4</sub> C MMC samples with uniform surfaces obtained after a 3-hour immersion period in a 0.5 M K <sub>2</sub> SO <sub>4</sub> solution (experimental data and  |    |

|             |  |     |
|-------------|--|-----|
|             | fitted curves are respectively presented by points and lines). .....   | 96  |
| Figure 5.7  | Equivalent circuit to interpret EIS spectra obtained from samples with uniform surface. ....   | 96  |
| Figure 5.8  | Typical (a) Nyquist and (b) Bode plots of AA1100-16 vol. % B <sub>4</sub> C MMC samples with defective surfaces obtained after a 3-hour immersion period in a 0.5 M K <sub>2</sub> SO <sub>4</sub> solution (experimental data and fitted curves are respectively presented by points and lines). .....  | 98  |
| Figure 5.9  | Equivalent circuit to interpret EIS spectra obtained from samples with defective surfaces (the pore section was taken from Figure 5.5; RE: reference electrode; WE: working electrode). ....   | 99  |
| Figure 5.10 | (a) Nyquist plots of the composite with uniform surface obtained after 3, 24, 48, 96 and 120 hours' immersion times in a 0.5 M K <sub>2</sub> SO <sub>4</sub> solution; (b) plot showing polarization resistance varying with time. ....   | 100 |
| Figure 5.11 | Optical and SEM micrographs showing the surface morphology of AA1100 – 16 vol. % B <sub>4</sub> C MMC (a) before corrosion and after a 120-hour immersion in a 0.5 M K <sub>2</sub> SO <sub>4</sub> solution (b) with agitation and (c) without agitation. ....  | 102 |
| Figure 5.12 | Corresponding EDS results of Figure 5.11: “Spectrum 1” points the B <sub>4</sub> C particle; “Spectrum 2” reveals that the B <sub>4</sub> C boundaries are rich in Ti, Al, O and trace elements; “Spectrum 3” exhibits the Al matrix under the cracked layer, “Spectrum 4” and “Spectrum 5” indicate the cracked and uncracked layer as Al oxide. .... | 103 |
| Figure 5.13 | IRRAS spectra of AA1100-16 vol. % B <sub>4</sub> C MMCs obtained from different conditions: (a) before and after 120-hour corrosion, (b) the difference of the two spectra seen in (a) with a corrected baseline. ....   | 105 |
| Figure 5.14 | X-ray photoelectron Al2p spectra of AA1100 -16 vol. % B <sub>4</sub> C samples (a) before corrosion and (b) after 120 hours corrosion in a 0.5 M K <sub>2</sub> SO <sub>4</sub> solution. ....   | 106 |
| Figure 5.15 | (a) SEM image showing the preferential deposition of small nodules over B <sub>4</sub> C particles; (b) and (c) EDS elemental mappings showing that the small nodules contained within the circle in (a) are essentially composed of Cu and O. ....  | 108 |
| Figure 5.16 | The schematic diagram showing the preferential deposition mechanism of copper oxide over B <sub>4</sub> C particles. ....  | 110 |
| Figure 6.1  | Chemical structure of BTAH. ....   | 117 |
| Figure 6.2  | Potentiodynamic polarization curves of AA1100-16 vol.% B <sub>4</sub> C in a 3.5 g/L NaCl solution containing different BTAH concentrations. ....  | 121 |
| Figure 6.3  | Variation of inhibition efficiency IE (%) as a function of BTAH  |     |

|             |  |     |
|-------------|--|-----|
|             | concentration in a 3.5 g/L NaCl solution. ....   | 124 |
| Figure 6.4  | Potentiodynamic polarization curves of AA1100, AA1100-16 vol.% B <sub>4</sub> C and AA1100-30 vol.% B <sub>4</sub> C immersed in (a) 3.5 g/L NaCl and (b) 3.5 g/L NaCl +0.05M of BTAH solution for one hour..... | 126 |
| Figure 6.5  | Plot showing the inhibition efficiency of 0.05 M of BTAH in a 3.5g/L NaCl solution as a function of the B <sub>4</sub> C particles volume fraction.....  | 127 |
| Figure 6.6  | Potentiodynamic polarization curves of AA1100-16 vol.% B <sub>4</sub> C in (a) 3.5 g/L NaCl and (b) 3.5 g/L NaCl +0.05M of BTAH with different immersion times. ....   | 129 |
| Figure 6.7  | Plot showing that the $E_b-E_{corr}$ obtained in the solution with BTAH has a linear relationship with the immersion times. ....   | 131 |
| Figure 6.8  | Nyquist plots of AA1100-16 vol.% B <sub>4</sub> C in 3.5 g/L NaCl with different concentrations of BTAH (experimental data and fitted curves are respectively presented by points and lines).....                | 132 |
| Figure 6.9  | The equivalent circuit used to interpret the experimental data obtained in a 3.5 g/L solution in the presence of BTAH at different concentrations.....   | 133 |
| Figure 6.10 | IRRAS spectra of AA1100-16 vol.% B <sub>4</sub> C MMCs obtained after immersion in a 3.5 g/L NaCl with different BTAH concentrations.....  | 136 |
| Figure 6.11 | Band area of Al(OH) <sub>3</sub> centered at 3500 cm <sup>-1</sup> as a function of inhibition efficiency. ....  | 136 |
| Figure 6.12 | Plot of log $\theta$ vs log CBTAH (Freundlich adsorption isotherm) obtained from the BTAH surface coverage values presented in Table 6.2.....  | 138 |
| Figure 7.1  | Time behavior of galvanic current $I_g$ for AA1100 coupled to SS304 and AA6061 in 3.5% NaCl. ....  | 152 |
| Figure 7.2  | Time behavior of galvanic current $I_g$ for AA1100-16 vol.% B <sub>4</sub> C coupled to SS304 and AA6061 in 3.5% NaCl. ....  | 153 |
| Figure 7.3  | Time behavior of galvanic current $I_g$ for AA1100-30 vol. % B <sub>4</sub> C coupled to SS304 and AA6061 in 3.5% NaCl. ....   | 153 |
| Figure 7.4  | Time behavior of galvanic current $I_g$ for AA1100 coupled to SS304 and AA6061 in 2500 ppm B-containing H <sub>3</sub> BO <sub>3</sub> .....   | 156 |
| Figure 7.5  | Time behavior of galvanic current $I_g$ for AA1100-16 vol. % B <sub>4</sub> C coupled to SS304 and AA6061 in 2500 ppm B-containing H <sub>3</sub> BO <sub>3</sub> .....  | 156 |

|             |   |     |
|-------------|---|-----|
| Figure 7.6  | Time behavior of galvanic current $I_g$ for AA1100-30 vol.% B <sub>4</sub> C coupled to SS304 and AA6061 in 2500 ppm B-containing H <sub>3</sub> BO <sub>3</sub> .....  | 157 |
| Figure 7.7  | Time behavior of galvanic potential for AA1100, AA1100-16 vol.% B <sub>4</sub> C and AA1100-30 vol.% B <sub>4</sub> C composites coupled to SS304 in 2500 ppm B-containing H <sub>3</sub> BO <sub>3</sub> solution..... | 157 |
| Figure 7.8  | Surface morphology of the AA1100-16 vol.% B <sub>4</sub> C composite coupled to SS304 after 24 h immersion in (a) 3.5% NaCl and (b) 2500 ppm B-containing H <sub>3</sub> BO <sub>3</sub> solution (100×).....           | 158 |
| Figure 7.9  | Average galvanic current density $\overline{I_g}$ as function of $\Delta\phi^s$ of uncoupled dissimilar materials in 2500 ppm B-containing H <sub>3</sub> BO <sub>3</sub> solution.....                                 | 160 |
| Figure 7.10 | Galvanic current $I_g$ as function of time and area ratio $A^C / A^A$ for AA1100-16 vol. % B <sub>4</sub> C coupled to SS304 in 3.5% NaCl solution.....   | 162 |
| Figure 7.11 | Galvanic potential $\phi_g$ as function of time for AA1100-16 vol. % B <sub>4</sub> C/SS304 couple with different area ratios in 3.5% NaCl solution.....  | 162 |
| Figure 7.12 | Galvanic current $I_g$ as function of time with oxygen purging during the test for AA1100-16 vol. % B <sub>4</sub> C/SS304 couple in 3.5% NaCl solution ( $A^C / A^A=1:1$ ).....  | 164 |
| Figure 7.13 | Galvanic current density $i_g^A$ with respect to anode (AA1100-16 vol. % B <sub>4</sub> C) as function of time and area ratio for AA1100-16 vol. % B <sub>4</sub> C/SS304 couple in 3.5% NaCl solution.....             | 166 |
| Figure 7.14 | Galvanic current density $i_g^C$ with respect to cathode (SS304) as function of time and area ratio for AA1100-16 vol. % B <sub>4</sub> C/ SS304 couple in 3.5% NaCl solution.....                                      | 166 |
| Figure 7.15 | Dependence of $i_g^A$ on area ratio $A^C/A^A$ in 3.5% NaCl solution.....  | 167 |
| Figure 7.16 | Dependence of corrosion rate $r_A$ of AA1100-16 vol. % B <sub>4</sub> C on area ratio $A^C/A^A$ in 3.5% NaCl solution.....  | 168 |
| Figure 7.17 | Galvanic current $I_g$ as function of time and area ratio $A^C / A^A$ for Al-16 vol. % B <sub>4</sub> C coupled to SS304 in 2500 ppm B-containing H <sub>3</sub> BO <sub>3</sub> solution.....                          | 169 |
| Figure 7.18 | Galvanic potential as function of time for Al-16 vol. % B <sub>4</sub> C/SS304 couple with different area ratios in 2500 ppm B-containing H <sub>3</sub> BO <sub>3</sub> solution.....                                  | 169 |

## **CHAPTER 1**

### **INTRODUCTION**

# CHAPTER 1

## INTRODUCTION

### 1.1 Definition of the Problem

Al-B<sub>4</sub>C metal matrix composites (MMCs) have received considerable attention due to their light weight, superior thermal conductivity, high stiffness and their hardness.<sup>[1]</sup> Owing to the special capturing neutron ability of isotope B<sup>10</sup>, Al-B<sub>4</sub>C MMCs have been increasingly used as excellent neutron absorber materials to fabricate the inside basket of transport and storage casks for spent nuclear fuels in the nuclear industry.<sup>[2-5]</sup>

However, although the incorporation of the particles into the Al matrix can enhance the physical and mechanical properties of the base material, it may also change its corrosion behavior.<sup>[6]</sup> Bhat *et al.*<sup>[7]</sup> investigated the corrosion behavior of the 6061 Al-SiCp composite and its base alloy in seawater using the potentiodynamic polarization technique. It was found that the composite corroded faster than its base alloy and that composite corrosion was mainly confined to the interface as opposed to the uniform corrosion observed for the base alloy. Sun *et al.*<sup>[8]</sup> also studied the corrosion behavior of 6061 Al-SiCp MMCs in a NaCl solution. With the observation that the pitting degree rose with an increase of SiC content, it is presumed that the occurrence of pitting corrosion depends on the local SiC distribution and the surface film integrity. According to the authors, larger

volume percentages of SiC could result in more opportunities for film disruption formation and consequently more pit initiation sites. Singh *et al.*<sup>[9]</sup> similarly studied the influence of SiC additions on the corrosion behavior of 2014 alloy in a 3.5% NaCl solution at 30 °C. It was revealed that the addition of 10 wt. % SiC into the base alloy considerably increases its corrosion resistance, while the addition of 25 wt. % SiC into the base alloy decreases the overall corrosion resistance of the material. From a more general perspective, Roepstorff *et al.*<sup>[10]</sup> reported that the corrosion resistance of metal matrix composites can essentially be affected by three processes: (1) galvanic coupling of the metal and reinforcement, (2) crevice attack at the metal/reinforcement interface, and (3) preferential localized attack on possible reaction products between metal and ceramic. According to Hihara *et al.*<sup>[11]</sup>, among these corrosion mechanisms, the galvanic corrosion between aluminum and reinforcement particles is of primary concern when studying MMC corrosion behavior.

As neutron absorber material used in the spent fuel storage racks or transportation casks, Al-B<sub>4</sub>C MMCs are placed between spent nuclear fuel assemblies. In the wet storage application, Al-B<sub>4</sub>C MMCs are continuously in contact with the reactor pool water (*i.e.* one of them is the boric acid with B concentration of ~2500 ppm), which is generally considered to be mildly corrosive.<sup>[12]</sup> Thus, from the safety point of view, it is of paramount importance to understand their corrosion behavior in boric acid solution. However, up to date, very limited studies have been devoted to the corrosion behavior of the Al-B<sub>4</sub>C MMCs, especially in boric acid, in contrast to considerable research in the corrosion behavior of Al-SiC and Al-Al<sub>2</sub>O<sub>3</sub> composites in various environments. Among literature on corrosion, 3.5% NaCl and 0.5 M K<sub>2</sub>SO<sub>4</sub> are the most commonly used solutions in studying

the corrosion behavior of the composites. Therefore, the present research aimed at investigating the corrosion behavior of Al-B<sub>4</sub>C MMCs in three solutions, *i.e.* 2500 ppm Boron-containing H<sub>3</sub>BO<sub>3</sub> solution, 3.5% NaCl and 0.5 M K<sub>2</sub>SO<sub>4</sub>.

A variety of methods such as anodizing and rare earth chloride inhibition have been suggested for the protection of aluminum metal matrix composites from corrosion. The organic compounds containing heteroatoms N, O, and S in the molecules were reported to be effective inhibitors for Al alloys in an environment containing aggressive ions [13-15]. It is believed that organic compounds inhibit the corrosion of Al alloys in some aggressive media by adsorbing on the material surface and forming a physical barrier between the material surface and the aggressive media. Benzotriazole, conveniently abbreviated as BTAH, has been known to be an effective inhibitor for copper and its alloys for more than sixty years.<sup>[16-18]</sup> It has been recently reported to be an effective corrosion inhibitor for iron and aluminum alloys. In the present research, benzotriazole was tentatively used as a corrosion inhibitor for Al-B<sub>4</sub>C composites in a NaCl solution.

As non-structural neutron absorber materials used to fabricate the inside basket of spent fuel storage racks or transportation casks, AA1100-B<sub>4</sub>C MMCs are often assembled to structural materials AA6061 aluminum alloy or 304 stainless steel (SS304). Consequently, the AA1100-B<sub>4</sub>C MMCs are galvanically coupled to AA6061 or SS304, which could potentially accelerate the corrosion of the less noble material. Such galvanic corrosion phenomenon is especially at risk when assemblies are used in the wet storage application of spent nuclear fuels that implies immersion in a mildly corrosive reactor pool water containing boric acid with B concentration of ~ 2500 ppm. However, up to date, no

research has been conducted in galvanic corrosion of AA1100-B<sub>4</sub>C MMCs/SS304 and AA1100-B<sub>4</sub>C MMCs/AA6061 couples. Accordingly, we have also investigated the galvanic corrosion of AA1100-B<sub>4</sub>C MMCs with different B<sub>4</sub>C levels (16 and 30 vol.%) coupled to AA6061 or SS304 in 3.5% NaCl and 2500 ppm boron-containing H<sub>3</sub>BO<sub>3</sub> solutions considering the effect of dissimilar materials, solution and area ratios of coupled materials.

## 1.2 Objectives

The present research aims to study the corrosion behavior of Al-B<sub>4</sub>C MMCs in a lab-scale condition that simulates the environment to which neutron absorber materials are exposed. This general objective could be achieved by four sub-objectives:

- (1) Investigating the corrosion susceptibility of Al-B<sub>4</sub>C MMCs in 2500 ppm boron-containing H<sub>3</sub>BO<sub>3</sub> in comparison with those in 0.5 M K<sub>2</sub>SO<sub>4</sub> and 3.5% NaCl solutions and finding out the influence of B<sub>4</sub>C particle levels on the corrosion resistance of the composites;
- (2) Studying the corrosion mechanism of Al-B<sub>4</sub>C MMCs in a 0.5 M K<sub>2</sub>SO<sub>4</sub> solution, 2500 ppm boron-containing H<sub>3</sub>BO<sub>3</sub> and 3.5% NaCl solutions;
- (3) Systematically investigating the inhibitive effect of BTAH on the corrosion of Al-B<sub>4</sub>C composites in a 3.5 g/L NaCl solution as a function of BTAH concentrations, B<sub>4</sub>C particle volume fractions and immersion times.

(4) Investigating the galvanic corrosion of Al-B<sub>4</sub>C MMCs associated with AA6061 or SS304 in 3.5% NaCl and 2500 ppm boron-containing H<sub>3</sub>BO<sub>3</sub> solutions considering the effect of dissimilar materials, solution and area ratios of coupled materials.

## References

- [1] X.-G. Chen, "Application of Al-B<sub>4</sub>C Metal Matrix Composites in the Nuclear Industry for Neutron Absorber Materials", in: *Proceedings of the Symposium on Solidification Processing of Metal Matrix Composites*, W.H. Hunt and N. Gupta (Eds.), TMS, 2006, pp. 343-350.
- [2] X.-G. Chen, R. Hark, "Development of Al-30%B<sub>4</sub>C Metal Matrix Composites for Neutron Absorber Material", in: *Proceedings of Aluminium Alloys: Fabrication, Characterization and Applications* W. Yin and S.K. Das (Eds.), TMS, 2008, pp. 3-9.
- [3] G. Bonnet, V. Rohr, X.-G. Chen, J.L. Bernier, R. Chiocca, H. Issard, "Use of Alcan's Al-B<sub>4</sub>C Metal Matrix Composites as Neutron Absorber Material in TN International's Transportation and Storage Casks", *Packaging, Transport, Storage and Security of Radioactive Material*, 20 (2009) 98-102.
- [4] A.R. Kennedy, "The Microstructure and Mechanical Properties of Al-Si-B<sub>4</sub>C Metal Matrix Composites", *Journal of Materials Science*, 37 (2002) 317-323.
- [5] C. Brown, C.G. Interrante, L.R. Abramson, "Neutron Absorbers: Qualification and Acceptance Tests", in: *Proceeding of the 13<sup>th</sup> International Symposium on Packaging and Transportation of Radioactive Materials (PATRAM)*, (Eds.), 2001, pp. 201-205.
- [6] L.H. Hihara, R.M. Latanision, "Corrosion of Metal Matrix Composites", *International Materials Review*, 39 (1994) 245-263.
- [7] M.S.N. Bhat, M.K. Surappa, H.V.S. Nayak, "Corrosion Behaviour of Silicon Carbide Particle Reinforced 6061/Al Alloy Composites", *Journal of Materials Science*, 26 (1991) 4991-4996.
- [8] H. Sun, E.Y. Koo, H.G. Wheat, "Corrosion Behavior of SiCp/6061 Al Metal Matrix Composites", *Corrosion*, 47 (1991) 741-753.
- [9] I.B. Singh, D.P. Mandal, M. Singh, S. Das, "Influence of SiC Particles Addition on the Corrosion Behavior of 2014 Al-Cu Alloy in 3.5% NaCl Solution", *Corrosion Science*, 51 (2009) 234-241.
- [10] S. Roepstorff, E. Maahn, "Corrosion Resistance of Aluminum-Silicon Carbide Composite Materials", in: *Proceeding of 12th Scandinavian Corrosion Congress and Eurocorr'92*, P.J. Tunturi (Eds.), Corrosion Society of Finland, 1992, pp.

- [11] L.H. Hihara, "Corrosion of Aluminum-Matrix Composites", *Corrosion Reviews*, 15 (1997) 361-386.
- [12] H. Ding, L. Hihara, "Localized Corrosion Currents and pH Profile Over B<sub>4</sub>C, SiC, and Al<sub>2</sub>O<sub>3</sub> Reinforced 6092 Aluminum Composites: I. In 0.5 M Na<sub>2</sub>SO<sub>4</sub> Solution", *Journal of the Electrochemical Society*, 152 (2005) B161-B167.
- [13] G. Bereket, A. Pinarbaşı, "Electrochemical Thermodynamic and Kinetic Studies of the Behaviour of Aluminium in Hydrochloric Acid Containing Various Benzotriazole Derivatives", *Corrosion Engineering Science and Technology*, 39 (2004) 308-312.
- [14] V. Branzoi, F. Golgovici, F. Branzoi, "Aluminium Corrosion in Hydrochloric Acid Solutions and the Effect of Some Organic Inhibitors", *Materials Chemistry and Physics*, 78 (2003) 122-131.
- [15] Z. Grubač, R. Babić, M. Metikoš-Huković, "Application of Substituted N-arylpyrroles in the Corrosion Protection of Aluminium in Hydrochloric Acid", *Journal of Applied Electrochemistry*, 32 (2002) 431-438.
- [16] K.F. Khaled, M.M. Al-Qahtani, "The Inhibitive Effect of Some Tetrazole Derivatives Towards Al Corrosion in Acid Solution: Chemical, Electrochemical and Theoretical Studies", *Materials Chemistry and Physics*, 113 (2009) 150-158.
- [17] T. Kosec, I. Milošev, B. Pihlar, "Benzotriazole As An Inhibitor of Brass Corrosion in Chloride Solution", *Applied Surface Science*, 253 (2007) 8863-8873.
- [18] F.M. Bayoumi, A.M. Abdullah, B. Attia, "Kinetics of Corrosion Inhibition of Benzotriazole to Copper in 3.5% NaCl", *Materials and Corrosion*, 59 (2008) 691-696.

## **CHAPTER 2**

### **LITERATURE REVIEW**

## CHAPTER 2

### LITERATURE REVIEW

#### 2.1 Al-B<sub>4</sub>C Composites

Metal matrix composites (MMCs) are metals reinforced with either particles or fibers and are particularly suited for applications that require strength and stiffness. They are being considered as good candidates for replacing conventional alloys in many industries such as aerospace, automotive, and sport due to their specific strength and stiffness compared to their matrix alloys.<sup>[1]</sup>

Metal matrix composites could be classified in consideration of type and contribution of reinforcement components in particle-, layer-, fiber-, and penetration composite materials (see Figure 2.1). Fiber composite materials could further be classified into continuous fiber composite materials (multi- and monofilament) and short fibers or, rather, whisker component materials, as seen in Figure 2.2.<sup>[2]</sup>

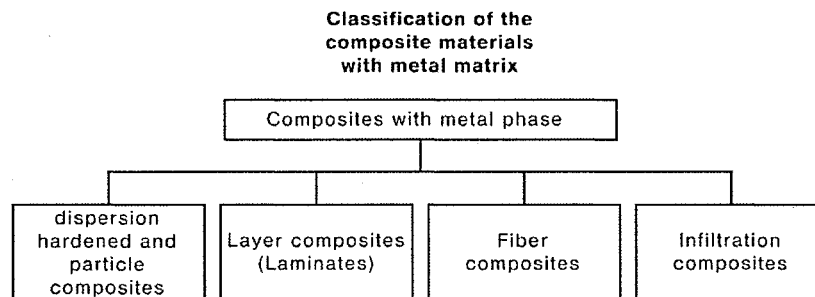


Figure 2.1 Classification of composite materials with metal matrixes.<sup>[1]</sup>

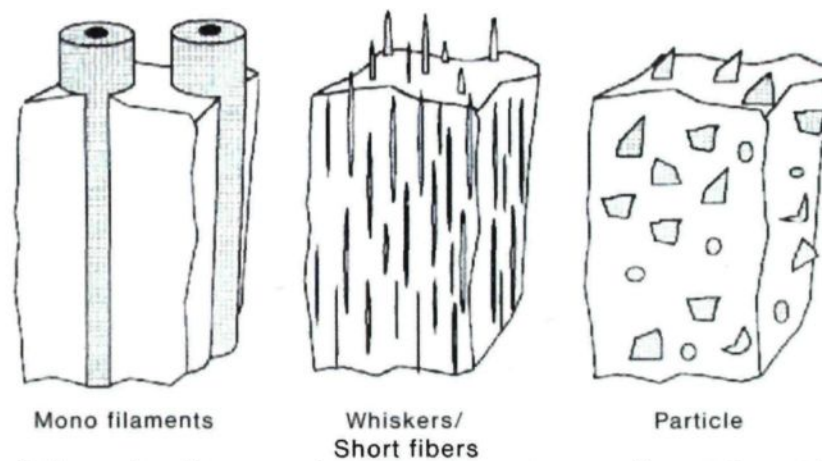


Figure 2.2 Schematic diagram showing three types of metal matrix component materials. <sup>[2]</sup>

Of all metal matrix composites, aluminum matrix composites have been the most popular due to their low cost over most other MMCs. In addition, they offer high strength-to-density ratios, excellent thermal conductivity, high shear strength, excellent abrasion resistance, high-temperature operation, non-flammability, minimal attack by fuels and solvents, and the ability to be formed and treated on conventional equipment. <sup>[1]</sup>

Boron carbide ( $B_4C$ ) appears to be an interesting strengthening agent for aluminum based composites with a low density ( $2.51 \text{ g/cm}^3$ ), a hardness just below that of diamond, excellent thermal stability and remarkable chemical inertness. <sup>[3]</sup> Owing to the specific ability of the  $^{10}B$  isotope to capture neutrons, Al- $B_4C$  composites are being extensively used to fabricate the inside baskets of storage and transport containers of spent nuclear fuels in the nuclear industry. <sup>[4-6]</sup>

Four Al- $B_4C$  composites are produced by Rio Tinto Alcan, as listed below: <sup>[7]</sup>

- (1) AA 6351 -  $B_4C$  composite;
- (2) AA 6063 -  $B_4C$  composite;

- (3) AA 1100 - B<sub>4</sub>C composite; and
- (4) Al - Si - B<sub>4</sub>C composite.

Of all four products, the AA1100-B<sub>4</sub>C composites are very attractive since they provide the highest B<sub>4</sub>C content, up to 30% by volume (28% by weight) and still have good formability for the extrusion and rolling manufacturing processes. However, it is a non-structural material. For this reason, in real applications, AA1100-B<sub>4</sub>C MMCs are often assembled with structural materials AA6061 or SS304. The typical composition of the AA 1100 composite is given in Table 2.1.

Table 2.1 Typical composition of AA1100-B<sub>4</sub>C composites.<sup>[7]</sup>

| Elements         | Amount (wt.%) |
|------------------|---------------|
| Ti               | 0.5 - 2.0     |
| B <sub>4</sub> C | ≤ 28          |
| AA1100           | balance       |

### 2.1.1 Fabrication Process of Al-B<sub>4</sub>C MMCs

Al-B<sub>4</sub>C composites could be produced by many different techniques. Two basic methods are commonly used, *i.e.*, powder metallurgy and liquid metal mixing.

(1) **Powder metallurgy.** The process starts with a blending of the boron carbide, aluminum powder, and alloying constituents. After blending, the mixture is placed in a drum-like vessel and compacted. Following compaction, the mixture is subject to a vacuum degas step and finally vacuum hot pressed into a near maximum theoretically dense billet, which can be further extruded and rolled. The schematic process could be seen in Figure

2.3. This method, however, is found to be expensive due to the high cost of metal powders and time-consuming process.<sup>[8]</sup>

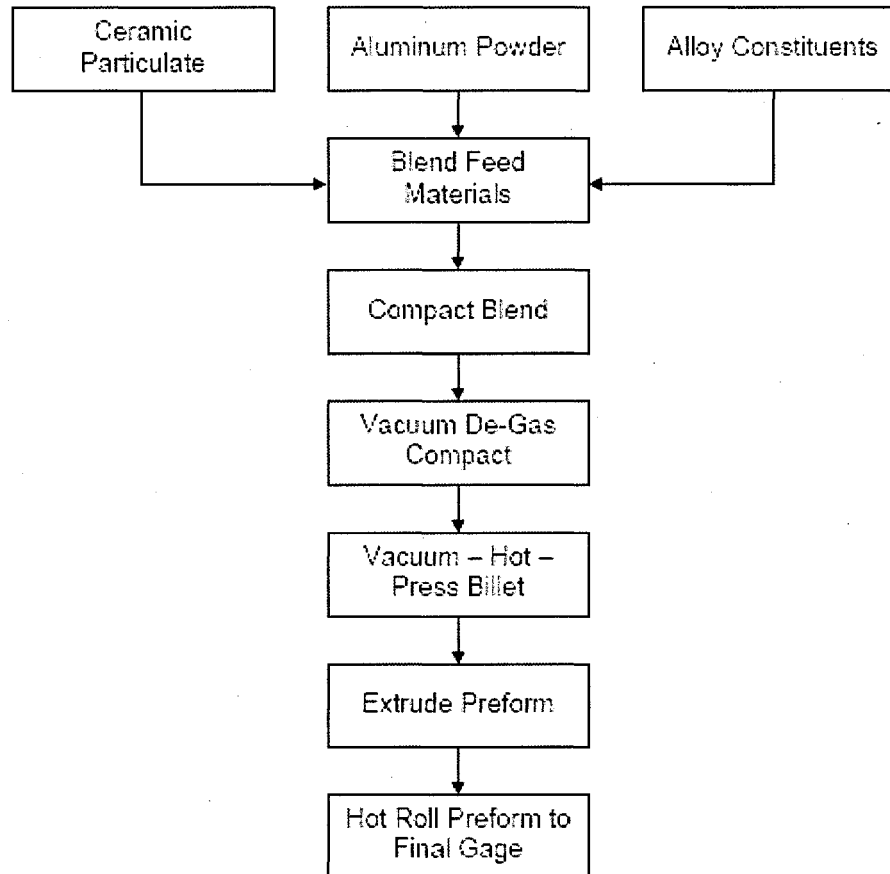


Figure 2.3 General steps in the powder metallurgy process.<sup>[8]</sup>

(2) **Liquid metal mixing.** In this process,  $B_4C$  particles are incorporated into the molten aluminum in a continuously stirred vacuum melt reactor, as depicted in Figure 2.4. It is very attractive due to its efficiency and low cost. Now it becomes a dominant method for producing the most common commercial aluminum MMC materials.<sup>[9]</sup> However, the concentration of reinforcement particles incorporated is limited up to 30 vol. %.

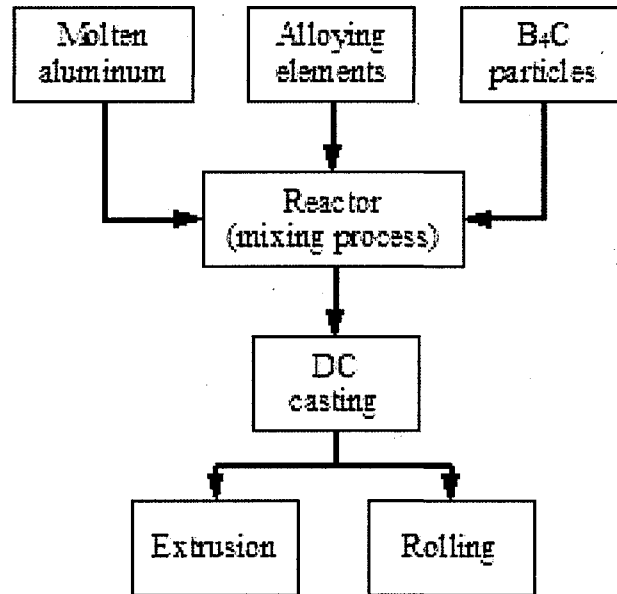
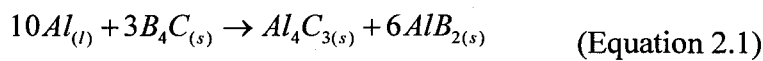
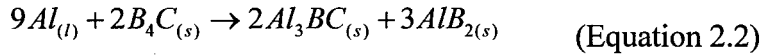


Figure 2.4 General steps in liquid mixing process.

### 2.1.2 Interfacial Reactions Between Al matrix and B<sub>4</sub>C Composites

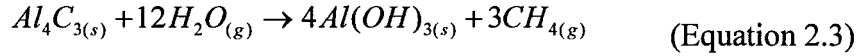
During the manufacturing process of Al-B<sub>4</sub>C, either the powder metallurgy or liquid melting method, the occurrence of interfacial reaction is a common problem. In the liquid mixing process, Al-B<sub>4</sub>C MMCs are manufactured at temperatures well above the liquidus of the Al matrix, and the processing time can be in the order of a few hours. Under these conditions, severe interface reactions between B<sub>4</sub>C particles and Al matrix can occur, and secondary phases Al<sub>4</sub>C<sub>3</sub> and AlB<sub>2</sub> or Al<sub>3</sub>BC (see Figure 2.5a) are formed according to Equations 2.1 and 2.2. These phases tend to aggregate into clusters (see Figure 2.6a) and leads to non-uniform distribution of boron carbide particles.<sup>[10]</sup> It is reported that formation of clusters could reduce the fluidity of the melt, deteriorates certain mechanical and physical properties and lowered the corrosion resistance of the composite.<sup>[11]</sup>



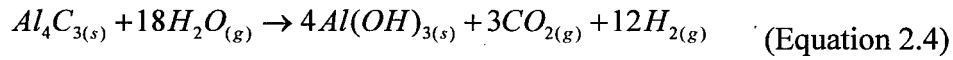


What's worse,  $Al_4C_3$  is water reactive and the reaction between  $Al_4C_3$  and water is thermodynamically favorable, increasing the corrosion sensitivity of the composites. [12]

The reactions are given as follows:

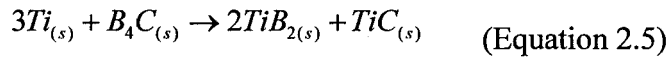


$$\Delta G_{298K} = -1847kJ$$



$$\Delta G_{298K} = -1746kJ$$

In order to protect  $B_4C$  particles from reaction with aluminum matrix, 0.5 ~ 2.0 wt. % titanium is added to the liquid aluminum. A thin, dense layer of  $TiB_2$  and  $TiC$  (as shown in Figure 2.5(b)) is formed *in-situ* on the boron carbide surfaces due to the reaction between Ti and  $B_4C$  that is more favored than the reaction between Al and  $B_4C$ . [13] Figure 2.6 shows the microstructure of Al- $B_4C$  MMCs before and after Ti addition. It is observed that the addition of Ti eliminates the formation of the secondary phases and large clusters, which ensures the uniform distribution of the  $B_4C$  particles during the liquid process. [10, 14]



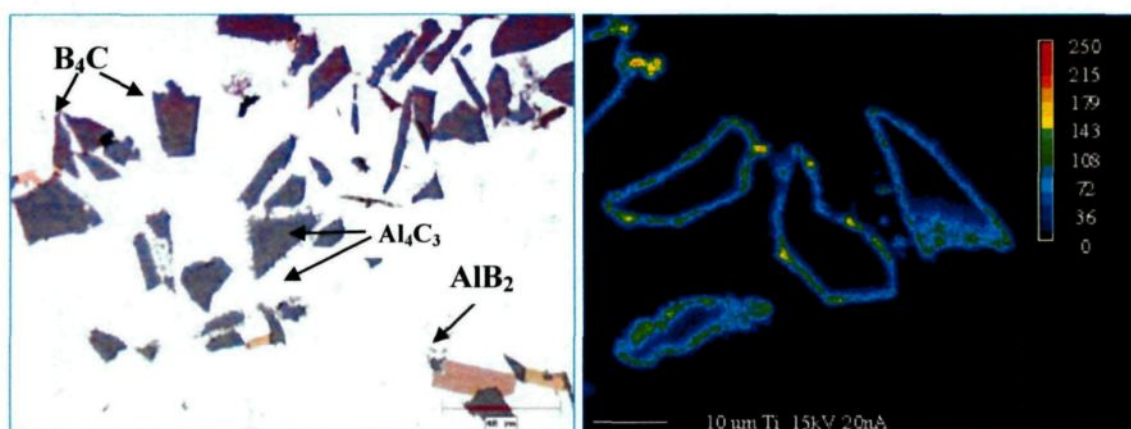


Figure 2.5 (a) Microstructure of AA1100-15 vol.% B<sub>4</sub>C and (b) Ti Mapping showing the Ti barrier layer at B<sub>4</sub>C and matrix interfaces. <sup>[13]</sup>

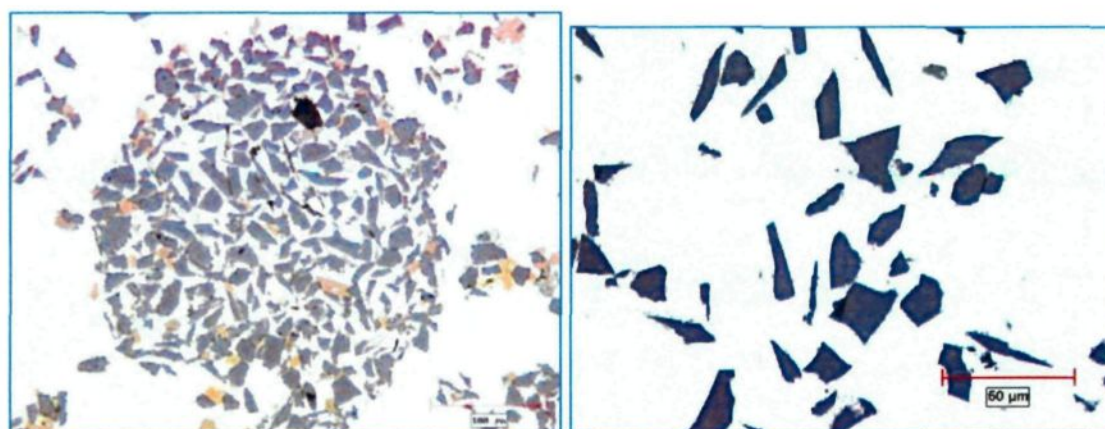


Figure 2.6 Optical micrographs showing (a) large clusters of secondary phases and (b) the uniform distribution of boron carbide in the matrix with the addition of Ti in AA6351-15 vol. % B<sub>4</sub>C composite obtained after 30 min processing time. <sup>[13]</sup>

### 2.1.3 Applications of Al-B<sub>4</sub>C MMCs in the Nuclear Industry

By virtue of the nuclide <sup>10</sup>B that has a large thermal neutron absorption cross section, in excess of 3800 barns, Al-B<sub>4</sub>C composites have been extensively used as the neutron absorbers for wet and dry storage applications.

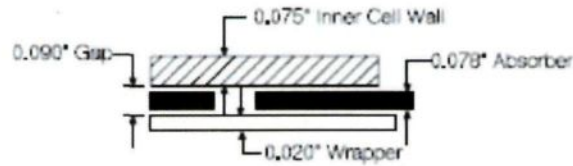
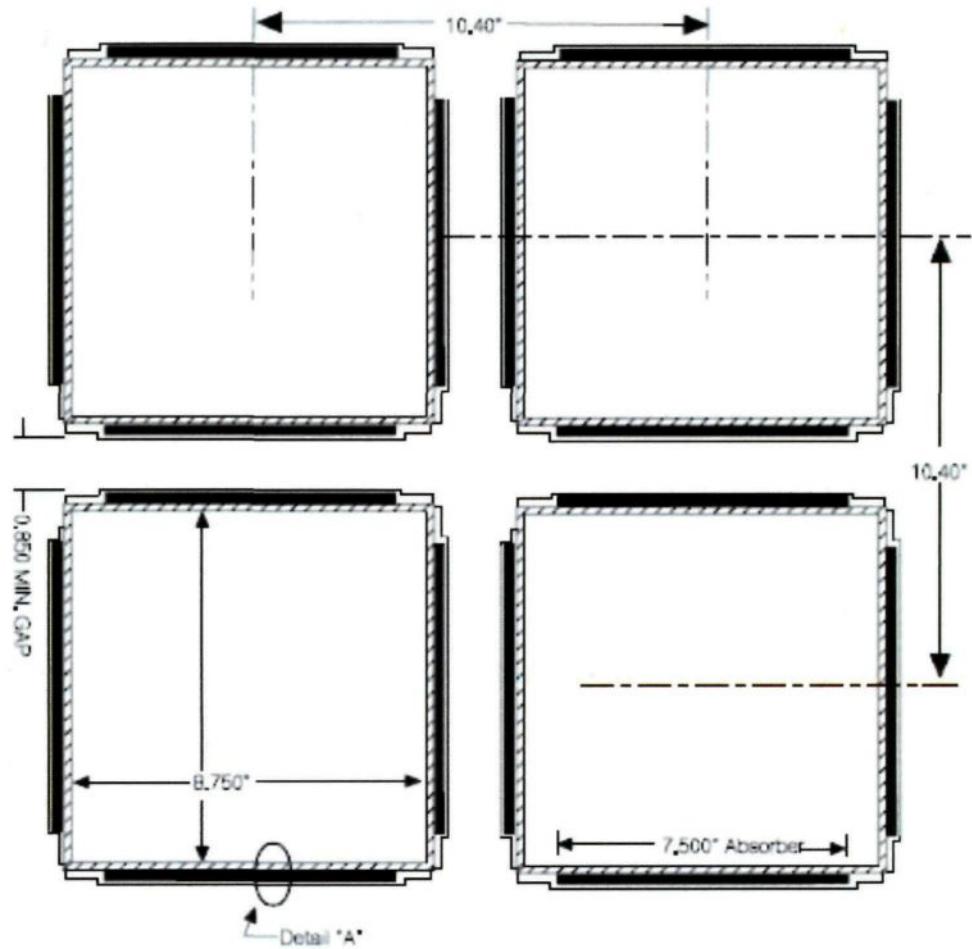
#### (1) Wet Storage – Use in Pool Racks

When the spent nuclear fuel rods are removed from the reactor core, they are extremely hot and must be cooled down in the pool, which is shown in Figure 2.7. Figure

2.8 is a cross section of a typical pressured water reactor (PWR) fuel rack for high reactivity, unburned reload fuel. The absorber plates are positioned on all four faces of the stainless steel cell walls that form a storage cell to keep distance of each and fuel rod and meanwhile to absorb the radiation given off by the nuclei inside the rod.



Figure 2.7 Spent nuclear fuel wet storage pool.<sup>[15]</sup>



**DETAIL "A"**

Figure 2.8 Cross section of a typical PWR storage cell. [7]

**(2) Dry Storage – Use in Multiple Purpose Canisters**

After several years cooling in a pool, spent fuels will be stored in the multiple purpose canisters (MPC) which is shown in Figure 2.9. Neutron absorbers for dry storage applications are positioned between spent fuel assemblies in a basket configuration in a

MPC. In this application, the neutron absorber is sheathed in a thin gage stainless steel to protect it from mechanical impact with fuel assemblies during fuel loading and to provide a means for affixing it to the walls of the MPC.



Figure 2.9 Multiple purpose canister of dry storage. <sup>[16]</sup>

In the wet storage application, the pool is not filled with ordinary water but with boric acid, which helps to absorb some of the radiation given off by the radioactive nuclei inside the spent rods. As we know, boric acid is a weak acid, even it is not aggressive but it still mildly corrosive. This means that the neutron absorber materials are immersed in a mildly corrosive solution for several years in the wet storage application and temporarily contact with this solution during the fuel loading in the dry storage application. Therefore, this risks the occurrence of corrosion in both wet and dry storage. Worse, the neutron absorber materials are usually assembled with structural materials such as SS304 to protect the neutron absorber materials from the mechanical impact, which increases the possibility of corrosion caused by the galvanic coupling effect between these materials. Accordingly, it is

of great importance to investigate the corrosion behavior of the neutron absorber materials (Al-B<sub>4</sub>C MMCs) in the boric acid solution.

## 2.2 Forms of Corrosion

Corrosion could be classified by many ways, the most important of which is by the appearance of the corroded metal. According to this category method, eight basic forms of corrosion are identified: <sup>[17]</sup>

### (1) Uniform corrosion

Uniform corrosion is also called general corrosion. It is characterized by the evenly corrosion over the entire surface area, or a large fraction of the total area (Figure 2.10). General thinning takes place until failure, thus it makes relatively rare disaster. It is the most important but easy-measured and predicted corrosion.

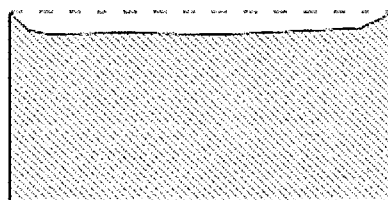


Figure 2.10 Schematic diagram showing the uniform corrosion.

### (2) Galvanic corrosion

Galvanic corrosion is also called “dissimilar metal corrosion”. It occurs when three conditions are satisfied: (1) dissimilar materials; (2) dissimilar materials are electrically coupled; and (3) the coupled dissimilar materials are immersion in an electrolyte, as shown in Figure 2.11. When a galvanic couple forms, the nobler metal becomes the cathode and

corrodes slower than it would all by itself, while the other becomes the anode and corrodes faster than it would alone.

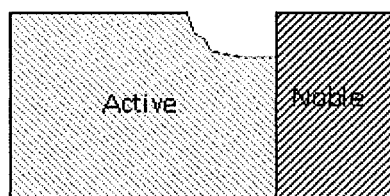


Figure 2.11 Schematic diagram showing the galvanic corrosion.

### (3) Pitting corrosion

Pitting corrosion is characterized by cavities or holes in the material, as depicted in Figure 2.12. It is considered to be more dangerous than uniform corrosion damage because it is more difficult to detect and predict.

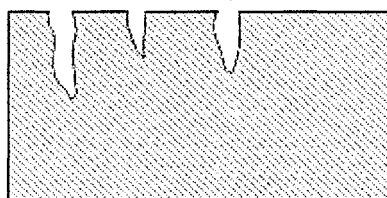


Figure 2.12 Schematic diagram showing the pitting corrosion.

### (4) Crevice corrosion

Crevice corrosion usually occurs in crevices between metals and metals or metals and nonmetals, as shown in Figure 2.13. It is associated with a stagnant solution on the micro-environmental level, in which, oxygen differential cell is easily formed. The stagnant solution in the crevice contains less oxygen than that contains on a surface, thus the lower oxygen content in the crevice forms an anode at the metal surface, and the solution exposed to air forms a cathode.

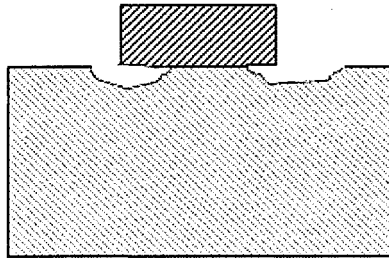


Figure 2.13 Schematic diagram showing the crevice corrosion.

**(5) Stress corrosion cracking**

Stress corrosion cracking (SCC) is the result of the combined effect of tensile stress and a specific corrosive environment. The impact of SCC on a material usually falls between dry cracking and the fatigue threshold of that material. Stresses may be due to applied loads, residual stresses from the manufacturing process, or a combination of both.

Figure 2.14 shows schematic diagram of stress cracking corrosion.

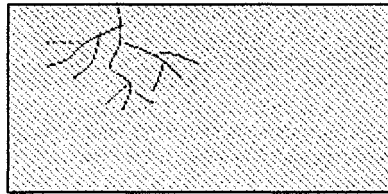


Figure 2.14 Schematic diagram showing stress corrosion cracking.

**(6) Intergranular corrosion**

Intergranular corrosion is, just as its name implies, localized attack along or adjacent to grain boundaries, while the bulk of the grains remain almost unaffected. This form of corrosion is usually associated with chemical segregation effects or specific phases precipitated on the grain boundaries. Figure 2.15 shows schematic diagram of intergranular corrosion.

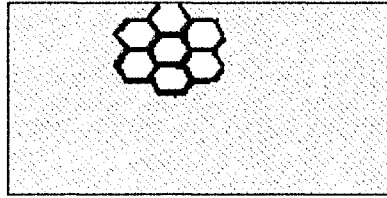


Figure 2.15 Schematic diagram showing intergranular corrosion.

**(7) Selective corrosion**

Selective corrosion can also be called dealloying. It refers to the selective removal of one element from an alloy by corrosion processes. After dealloying, the alloy loses the active component of the metal and retains the more corrosion resistant component in a porous "sponge" on the metal surface. A common example is the dezincification of unstabilized brass, the selective removal of zinc can proceed in a uniform manner or on a plug-type scale, as illustrated in Figure 2.16.

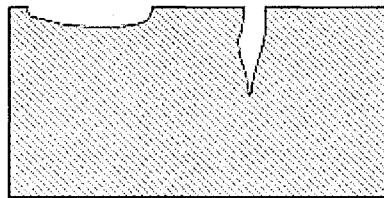


Figure 2.16 Schematic diagram showing selective corrosion.

**(8) Erosion Corrosion**

Erosion corrosion is induced from the combination of an aggressive chemical environment and high fluid-surface velocities, as illustrated in Figure 2.17. The increased turbulence caused by pitting on the internal surfaces of a tube can result in rapidly increasing erosion rates and eventually a leak. Erosion corrosion can also be aggravated by faulty workmanship.

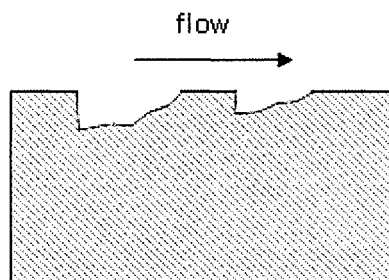


Figure 2.17 Schematic diagram showing erosion corrosion.

It is reported that three corrosion forms are predominant for the aluminum metal matrix composites, they are: (1) galvanic coupling of the aluminum and reinforced particles, (2) crevice corrosion at the aluminum/reinforcement interface, and (3) preferred localized attack at possible reaction products between metal and ceramic. <sup>[18]</sup>

### 2.3 Corrosion of Aluminum Metal Matrix Composites

Although the incorporation of the particles into the Al matrix can enhance the physical and mechanical properties of the base material, it may also change its corrosion behavior. <sup>[19]</sup> It is reported that incorporation of the reinforcement breaks the continuity of the protective aluminum oxide film and increases the number of sites where pitting could be initiated. Bhat *et al.* <sup>[20]</sup> investigated the corrosion behavior of the 6061 Al-SiCp composite and its base alloy in seawater using the potentiodynamic polarization technique. It was found that the composite corroded faster than its base alloy and that composite corrosion was mainly confined to the interface as opposed to the uniform corrosion observed for the base alloy, as shown in Figure 2.18. Sun *et al.* <sup>[21]</sup> also studied the corrosion behavior of 6061 Al-SiCp MMCs in a NaCl solution. They found that pitting degree rose with an increasing SiC content and that pitting corrosion depends on the local

SiC distribution and the surface film integrity. A larger volume percentage of SiC results in more opportunities for film disruption and consequently more pit initiation sites. Singh *et al.* [22] recently studied the influence of SiC additions on the corrosion behavior of 2014 alloy in a 3.5% NaCl solution at 30 °C. It was revealed that the addition of 10 wt. % SiC into the base alloy increases its corrosion resistance considerably, while the addition of 25 wt. % SiC into the base alloy decreases the overall corrosion resistance of the material. Using a scanning micro reference electrode (SMRE) technique, Feng *et al.* [23] found that 2024-SiCp MMCs was more susceptible to pitting corrosion than unreinforced alloy and increasing the volume fraction of SiC particles resulted in a significant decrease in pitting potential.

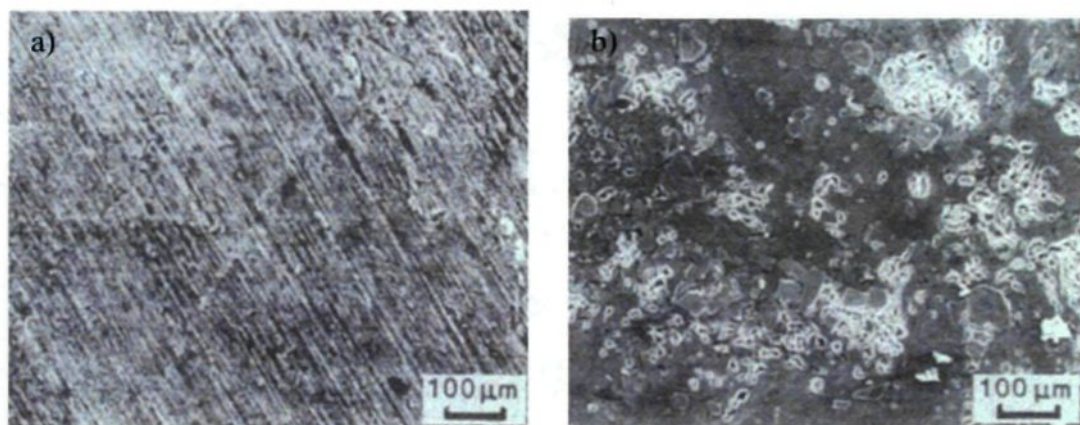


Figure 2.18 Scanning electron micrographs of samples corroded in sea water at 300 K (a) base alloy (6061 Al) and (b) as-cast composite. [20]

Except for pitting, galvanic couple formed between the reinforced ceramic and the matrix alloy could also stimulate the corrosion of the composite and thus decrease its corrosion resistance. According to Hihara *et al.*, [24] galvanic corrosion between aluminum and the reinforcement particles is primary consideration with respect to the corrosion behavior of metal matrix composites. Ding *et al.* [25] investigated the galvanic corrosion of B<sub>4</sub>C reinforced 6092-T6 alloys by soaking the composite in a 0.5 M Na<sub>2</sub>SO<sub>4</sub> solution

containing 3-5 ppm  $\text{H}_2\text{PtCl}_6$  for 5 hours (platinization method). They concluded that  $\text{B}_4\text{C}$  particles were cathodic sites and induced galvanic effects on the corrosion of the 6092- $\text{B}_4\text{C}$  composites. Bakkar and Neubert<sup>[26]</sup> investigated the corrosion behavior of carbon fibers reinforced magnesium metal matrix composite (MMC) in alkaline aqueous solutions containing 100 ppm NaCl. They assumed that the galvanic coupling formed between Mg and C-fibers causes the shift of the corrosion potential in the noble direction by more than 1000 mV compared to their monolithic counterparts.

However, the galvanic couple effect of Al and SiC particles is controversial. In general, silicon carbide reinforced aluminum alloy composites (MMCs) are considered to be more susceptible to corrosion attack than their monolithic counterparts.<sup>[27]</sup> In aqueous solution, SiC can serve as inert electrode and therefore galvanic cell is formed.<sup>[19]</sup> Dikici *et al.*<sup>[28]</sup> found that the galvanic cells between SiC particles and aluminum matrix could be formed and are responsible for the decrease in high corrosion potential and pitting potential. While Cheng *et al.*<sup>[29]</sup> reported that SiC particles are nonmetallic and thus could not form the galvanic cell with the Al matrix. Instead, the existence of SiC particles minimize the effective corrosion area of the matrix, leading to less galvanic corrosion cells formed between secondary phases and the matrix, which is schematically shown in Figure 2.19. Pardo *et al.*<sup>[30]</sup> studied the corrosion behavior of silicon carbide particle (SiCp) reinforced AZ92 magnesium alloy manufactured by a powder metallurgy process in 3.5 wt.% NaCl solution, neutral salt fog (ASTM B 117) and high relative humidity (98% RH, 50 °C) environments. They believed that the SiC is an insulator and is not expected to have any galvanic interaction with the AZ92 matrix. It was likely that the reinforcement increased

the corrosion rate due to the presence of Mg matrix/SiCp interfaces breaking the continuity of the Mg matrix and creating preferential locations for corrosion attack.

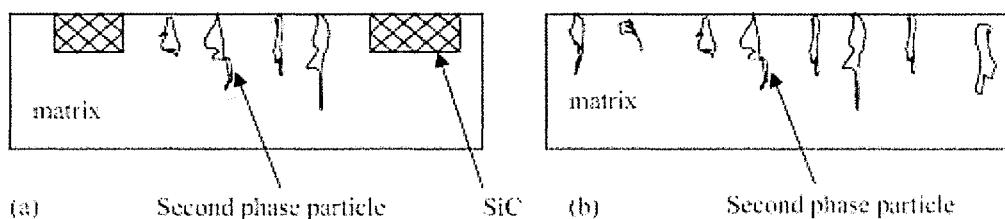


Figure 2.19 Schematic diagram showing the microstructure (a) 7075-SiCp MMC and (b) 7075 alloy.<sup>[29]</sup>

Secondary phases formed during the metallurgy process and the crevices existing at the vicinity of reinforcement may also be the preferred sites of corrosion.<sup>[31, 32]</sup> In the case of AA2009/SiC<sub>w</sub>, Yue *et al.*<sup>[33]</sup> proved that it was Al<sub>2</sub>Cu rather than SiC reinforcement that played a dominant role in the pitting process. They also explained that after the chloride ions broke into the air-formed oxide layer at the particle/matrix interface, the Al around the Al<sub>2</sub>Cu particles started to dissolve, which leads to the formation of micro-crevices at the interfaces, with increasing immersion time, the crevice would be gradually enlarged and eventually led to open pits. Ding and Hihara<sup>[34]</sup> investigated the effect of B<sub>4</sub>C particles on the corrosion behavior of 6092-T6 Al MMCs with 20 vol. % B<sub>4</sub>C in a 0.5 M Na<sub>2</sub>SO<sub>4</sub> solution at room temperature. They found that corrosion initiation and propagation are related to the formation of microcrevices caused by reinforcement particles left in relief, to localized acidification and alkalization of the solution, and to aluminum containing amphoteric oxides. Ahmad *et al.*<sup>[11]</sup> found that less cluster of the composites and more homogeneous distribution of the secondary phases led to a better corrosion resistance for the composite 6013-20SiC. Winkler *et al.*<sup>[35]</sup> studied the pitting corrosion of 50 vol. % Altex (15%SiO<sub>2</sub>-Al<sub>2</sub>O<sub>3</sub>) reinforced 7XXX alloys. It was observed that pitting occurred

preferentially not only in cast-defects, but also at grain boundaries and fiber/interface regions.

In contrast to the considerable amount of research work dedicated to a better understanding of the corrosion behavior of Al-SiC composites, there are only a few studies devoted to the corrosion behavior of Al-B<sub>4</sub>C composites. Emmerich *et al.* [36] performed electrochemical polarization measurements on pure aluminum and borated AA1100 in the as-received surface condition in two different electrolytes at 90 °C. The first solution contained 0.15 mg/L fluoride and 0.15 mg/L chloride, while the second contained the same quantity of fluoride but a higher chloride ion concentration (*i.e.* 1.0 mg/L). The applied potential was increased from -300 mV to +400 mV during a potentiodynamic polarization experiment. For borated aluminum, current transients (*i.e.*, metastable depassivation events) were observed and attributed to locally thinner and/or less stable passivation layers on the surface. The cause for such inhomogeneous passive layers could be mechanical surface defects or inclusions in the alloy. It was also presumed that both AlB<sub>2</sub> and AlB<sub>12</sub> particles present in the alloy could act as nucleation sites.

#### **2.4 Galvanic Corrosion of Metal Matrix Composites Associated With Dissimilar Materials**

As non-structural neutron absorber materials used to fabricate the inside basket of spent fuels storage racks or transportation casks, AA1100-B<sub>4</sub>C MMCs are often assembled with structural materials AA6061 or SS304. Consequently, the AA1100-B<sub>4</sub>C MMCs are galvanically coupled with AA6061 or SS304, which accelerates the corrosion of the less

noble material, especially when they are used in the spent nuclear fuel wet storage application, where the assemblies are immersed in the mildly corrosive reactor pool water (one of which is the boric acid with B concentration of ~2500 ppm).

As reported, the potential difference of two materials is considered to be the driving force of the galvanic corrosion. The extent of galvanic corrosion between two or more dissimilar materials also depends on the effective area ratio of coupled dissimilar materials, the cathodic efficiency and polarization characteristics of the nobler material, solution conductivity, oxygen content in the solution, the temperature and stability of passive films. [37, 38] Mansfeld *et al.* [39, 40] studied the galvanic corrosion of Al alloys and other dissimilar metals or alloys to establish the galvanic series based on the quantitative measurements of dissolution rate of the metals in a galvanic couple. In a consequent series studies, they investigated the effect of the corrosive environment, (*i.e.* distilled water, tap water and 3.5% NaCl solution) [41] and effect of area ratio on the galvanic corrosion. [42]

## 2.5 Corrosion Prevention

There are lots of methods used to prevent corrosion. In fact, these methods could not prevent the corrosion completely, but they do reduce the corrosion to a minimum value. Here gives a brief introduction to several of them.

(1) Coatings. Coatings are the most widely used corrosion control technique. Essentially, this technique is a means for separating the surfaces that are susceptible to corrosion from the factors in the environment which cause corrosion. However, that protective coating can never provide 100 percent protection of 100 percent of the surface.

According to the coating materials, it is divided into three types: (1) metallic coatings, it includes electroplating, galvanising, metal spray coatings; (2) non-metallic coatings, like anodizing and conversion coatings; (3) organic coatings, such as claddings and paint.

(2) Cathodic protection. This corrosion prevention method is based on the concepts of an electrochemical cell, in which the metal to be protected is a cathode in the cell. This could be achieved by using a sacrificial anode or by using a DC current.

(3) Anodic protection. In this method, the metal to be protected is placed as anode. The corrosion product will precipitate on the surface of the anode and form a protective film with uniform distribution. In this process, the environment should be homogeneous in all places on the surface of the metal, and the current distribution on the surface should be uniform.

(4) Use of Inhibitors. Corrosion inhibitors are those organic or inorganic chemical species which when added to the environment in small amount, they reduce the corrosion rate. Inhibitors could react with the surface of a material decreasing the material's corrosion rate, or interact with the operating environment to reduce its corrosiveness. Corrosion inhibitors interact with the metal, slowing the corrosion process by: (1) shifting the corrosion potential of the metal's surface towards either the cathodic or anodic direction; (2) preventing permeation of ions into the metal and (3) increasing the electrical resistance of the surface. Addition of inhibitors is only effective for general corrosion but not for localized corrosion.

Inhibitors interact with the surface of a metal in two ways: (1) to form a passive film on the surface, and (2) to work as a barrier on the surface of the metal. Inhibitors are usually grouped into five different categories: passivating, cathodic, organic, precipitation and vapor phase. <sup>[43]</sup>

(1) Passivating inhibitors. Passivating inhibitors are the most common type of inhibitors due to their effectiveness in reducing the rate of corrosion. They protect the material by helping in forming a thin, inert film on the surface of a metal, thereby shifting the corrosion potential toward the noble region, which effectively passivates the metal.

(2) Cathodic inhibitors. Cathodic inhibitors protect the metal by inhibiting the rates of the cathodic reaction of the electrochemical cell. This is achieved by building a barrier layer to obstruct the corrosive agents from accessing the metal surface or by preventing the corrosive ions in the cathodic process from forming their normal products. Cathodic inhibitors usually shift the corrosion potential in a negative direction.

(3) Organic inhibitors. Organic inhibitors protect the metal by adsorbing to the surface to form a thin, water-displacing film. The adsorptive bond between the metal and film determines the protection level of the inhibitor.

(4) Precipitation inhibitors. Precipitation inhibitors are chemicals that can induce the formation of precipitates on a metal. The precipitates tend to cover the entire surface of the metal and act as somewhat of a barrier to the corrosive environment.

(5) Vapor phase inhibitors. This kind inhibitor is usually carried by a vapor phase product, such as water vapor to the metal surface. When it reaches the metal surface, the vapor phase condense, resulting in a release of the inhibitor ions.

A variety of methods such as anodizing, <sup>[44-46]</sup> chromate conversion coatings and rare earth chloride inhibition <sup>[47-49]</sup> have been suggested for the protection of aluminum metal matrix composites from corrosion. Despite the advantages offered by chromate conversion coating, their application has been limited because of recognized health risks associated with them. Recently, the organic compounds containing heteroatoms N, O, and S in the molecules were reported to be effective inhibitors for Al alloys in an environment containing aggressive ions. <sup>[50-52]</sup> It is believed that organic compounds inhibit the corrosion of Al alloys in some aggressive media by adsorbing on the material surface and forming a physical barrier between the material surface and the aggressive media. The adsorption process is influenced by the nature and surface charge of the alloy surface, the chemical structure of the organic inhibitors, the type of electrolyte and the type of interaction between the organic molecules and the metallic surface. <sup>[53]</sup>

For more than sixty years, benzotriazole, conveniently abbreviated as BTAH (Figure 2.20), has been known to be an effective inhibitor for copper and its alloys. <sup>[54-56]</sup> It has been recently reported to be an effective corrosion inhibitor for iron <sup>[57, 58]</sup> and aluminum alloys. <sup>[59]</sup> In the present research, benzotriazole was extensively used as corrosion inhibitor of Al-B<sub>4</sub>C composites in 3.5 g/L NaCl solution and its corrosion efficiency was systematic studied.

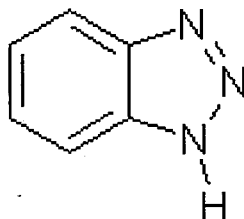


Figure 2.20 Chemical structure of BTAH.

## 2.6 Basic Aspects of Electrochemical Processes

### 2.6.1 Electrical Double Layer

The interface between the electrode and the electrolyte is the “core” of electrochemical process. It is the place where charge transfer takes place, where electrical and chemical potential gradients constitute the driving force for electrochemical reactions. Many models have been put forward to describe its structure, and the classical one is the electrical double layer. Figure 2.21 schematically describes the structure of electrical double layer between metal and electrolyte. The layer close to the electrode containing solvent molecules and sometimes “specially adsorbed” ions is called compact Helmholtz (or Stern) layer. The electrical centers of these “specially adsorbed” ions are called the *inner Helmholtz plane* (IHP), which is at a distance of  $z_1$ . The total charge density from these “specially adsorbed” ions is  $\phi_1$ . Solvated cations can approach the metal only to a distance of  $z_2$  and thus they are specified as “nonspecially adsorbed” ions. The centers of these “nonspecially adsorbed” ions are called the *outer Helmholtz plane* (OHP). The layer where the “nonspecially adsorbed” ions distributed is called diffusive layer, and it extends

from OHP to the bulk of the solution. <sup>[60]</sup> The charge density in this layer is  $\varphi^2$ . The total charge density on the solution side of the double layer  $\varphi^S$  is given by

$$\varphi^S = \varphi^1 + \varphi^2 = -\varphi^M$$

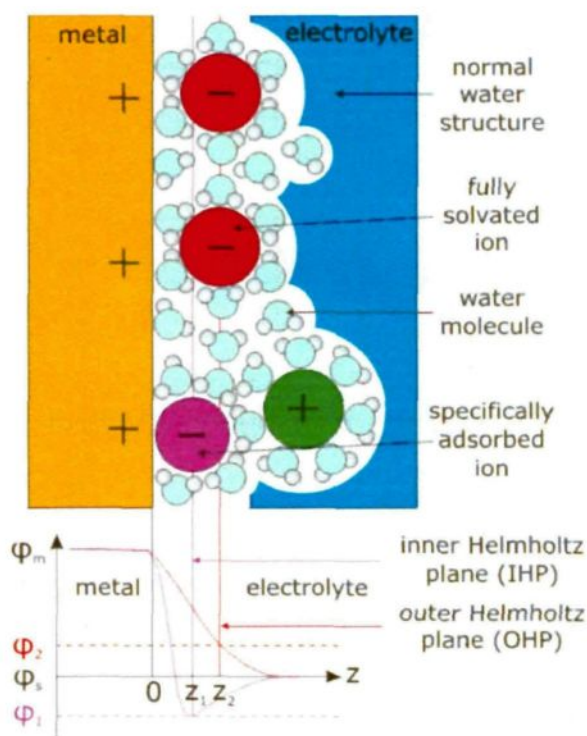


Figure 2.21 Proposed model of the double-layer region under conditions where anions specially adsorbed.

A characteristic feature of metal/aqueous electrolyte interfaces is their remarkably high capacity, which ranges between 20 and 50  $\mu\text{F}\cdot\text{cm}^{-2}$ . By applying a potential drop across the electrochemical interface of up to 1 V (which for noble metal electrodes is indeed possible) high surface charges of up to about 10 - 50  $\mu\text{C}\cdot\text{cm}^{-2}$  can be achieved (corresponding to a charge of about 0.1 - 0.2 electrons per surface atom), and extremely high electric fields of about  $3\times 10^7 \text{ Vcm}^{-1}$  can be obtained.

### 2.6.2 Three-Electrode Cell

The so-called “three-electrode” are the working electrode, the counter electrode, and the reference electrode, as illustrated in Figure 2.22. The working electrode is the sample being investigated. The reference electrode provides a stable “reference” potential against to which the potential of the working electrode may be accurately measured, so the reference electrode must be non-polarizable. A high-input-impedance device is used to measure the potential difference between working electrode and the reference electrode, so that a negligible current passes through the reference electrode. As consequence, its potential will remain constant and equals to the open-circuit potential. To decrease the uncompensated resistance existing between working electrode and reference electrode, *Luggin-Harber* capillary is employed, the tip of which is located as close as possible to the working electrode surface. In the three-electrode cell, the current passes between working electrode and counter electrode. The counter electrode should not produce substances by electrolysis that will reach the working electrode and causing interfering reactions there. <sup>[60]</sup>

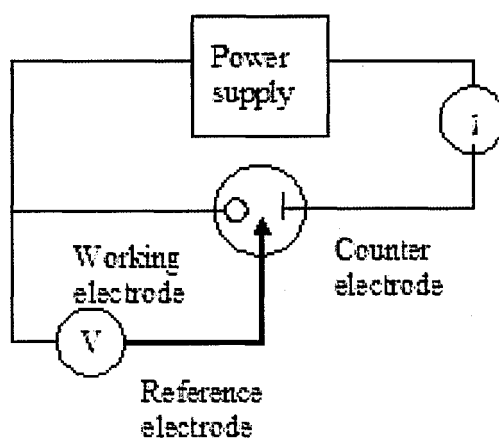


Figure 2.22 Three-electrode cell and notation for the difference electrodes. <sup>[60]</sup>

## **2.7 Corrosion testing and evaluation techniques**

There are numerous methods that may be used to test and evaluate the corrosion. The following section aimed at introducing some of available technologies and their applicability to the various forms of corrosion.

### **(1) Weight loss measurements**

This is the simplest corrosion monitoring technique, which involves exposing a specimen of material to a process environment for a given duration, then removing the specimen for analysis. This usually means the measurement of weight loss; the corrosion rate can be calculated from the weight loss and the period the coupon was exposed.

### **(2) Electrical Resistance Measurement**

This technique measures the change in resistance of a corroding metal element exposed in a process stream. The corrosion of the element causes a decrease in its cross-sectional area and a resultant increase in electrical resistance from which the corrosion rate can be calculated.

### **(3) Linear Polarization Resistance (LPR) Measurement**

In simple terms the LPR technique involves the application of a small voltage to an electrode in solution. The current needed to maintain a specific potential shift is directly related to the corrosion on the surface of the electrode from which the corrosion rate can be derived instantaneously.

### **(4) Electrochemical impedance spectroscopy (EIS)**

Electrochemical impedance spectroscopy (EIS), like LPR, uses the polarization of electrodes to measure corrosion rate. The difference is that EIS uses alternative currents and measures the resulting phase shift relative to the applied current. This technique will be introduced in section 2.7.2 in detail.

(5) Electrochemical noise.

This technique simultaneously measures changes in the electric potential and current between freely corroding electrodes. This technique may be used to identify pit initiation and growth. However, the interpretation of signals is complex. Although this technique is proven and can detect different corrosion processes, it remains difficult to determine the accuracy of corrosion rates derived from these measurements.

(6) Zero Resistance Ammetry (ZRA)

This is an electrochemical technique in which two electrodes of dissimilar metals are exposed to the process. The current generated due to the natural potential difference of the electrodes relates to the rate of corrosion that is occurring. This technique will be introduced in section 2.7.3 in detail.

(5) Hydrogen Probe

Many corrosion processes involve atomic hydrogen as a product of the corrosion reaction. Thus, by measuring the atomic hydrogen present, a corrosion rate may be determined. This method has been highly beneficial in oil refining and petrochemical industries due to the presence of hydrogen sulfide in such plants.

## 2.7.1 Potentiodynamic Polarization

Within the framework of a corrosion study, the aim of potentiodynamic polarization technique is to bring the potential of a material out of its quasi-equilibrium state and, thereafter, to investigate its corrosion behavior by measuring currents and observing other specific electrochemical signatures. Indeed, while potentiodynamic curves are mainly used to calculate corrosion current densities in the vicinity of the corrosion potential, they can also be applied to investigate different distinctive features such as the existence of a passive film, the susceptibility to pitting corrosion of a material, the stability of a surface over a wide range of potentials, etc. In laboratory, polarization experiments have the ability to rapidly indicate the corrosion behavior of a material in a specific environment whose composition simulates real service conditions.

### 2.7.1.1 Anodic polarization scan <sup>[61]</sup>

A schematic anodic polarization curve is illustrated in Figure 2.23. As can be seen in the figure, the scan starts from point 1 and progresses in the positive direction until point 2. The corrosion potential is located at point A, where the sum of the anodic and cathodic reaction rates on the electrode surface is zero. As a result, the measured current will be close to zero. As the potential increases, active region (region B) is observed. In this region, metal oxidation is the dominant reaction taking place. The potential at Point C is known as the passivation potential, above which the current density is seen to decrease with increasing potential (region D) until a low, passive current density is achieved (Passive region - Region E). Once the potential reached a sufficiently positive value (Point F,

sometimes termed the *breakaway potential*) the applied current rapidly increases (region G). This increase may be due to a number of phenomena, depending on the alloy/environment combination. For aluminum alloys in salt water, this sudden increase in current may be attributable to pitting. For some alloys with a very protective oxide, such as cobalt, the sudden increase in current is due to oxygen evolution reaction (OER).

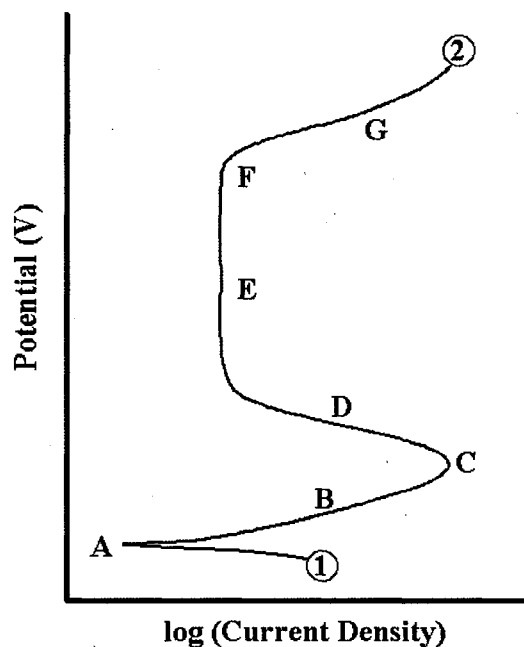


Figure 2.23 Theoretical anodic polarization scan. <sup>[61]</sup>

In potentiodynamic polarization process, the scan rate is a very important parameter. Higher scan rates do not allow sufficient time for the system to stabilize at each potential. As a result, parameters such as the passivation potential and the pitting potential are often shifted to more positive values. The ASTM standard scan rate is 0.1667 mV/s.

It should be stressed that this is a schematic diagram illustrating some of the possible regions present on an anodic polarization scan. Depending on the nature of a particular system, some or all of these features may be present. Bakkar and Neubert <sup>[26]</sup> investigated

the corrosion behavior of carbon fibers reinforced Mg MMCs in alkaline aqueous solutions containing 100 ppm NaCl. The anodic polarization curve in Figure 2.24 was divided into three regions. The first region (I) indicates the clear passivation after the Tafel part, whereas the second region (II) is characterized by a noticeably gradual increase in the current density with a forward potential scan. Then, it is followed by a sharp increase in the current density and region (III), which may characterize the occurrence of pitting corrosion.

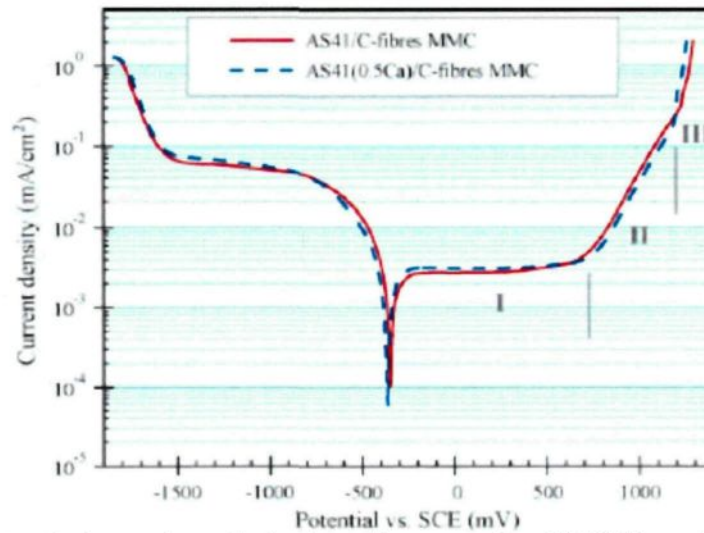


Figure 2.24 Potentiodynamic polarisation diagrams for C/AS41 and C/AS41(0.5% Ca) Mg MMCs in 100 ppm NaCl solution, pH 12.<sup>[26]</sup>

### 2.7.1.2 Tafel plot

For reactions which are essentially activation controlled (*i.e.* charge transfer controlled reactions, or mass transfer controlled reactions occurring at a rate much less than the limiting rate), the current density can be expressed as a function of the overpotential  $\eta$ ,

$$\eta = E_{\text{applied}} - E_{\text{equilibrium}}$$

$$\eta = \beta \log \frac{i}{i_0}$$

This expression is known as the Tafel equation, where  $\beta$  is the Tafel slope,  $i$  the applied current density, and  $i_0$  the exchange current. Thus, the Tafel slope  $\beta$  for the anodic and cathodic reactions occurring at open circuit may be obtained from the linear regions of the polarization curve, as illustrated in Figure 2.25. Once these slopes have been established, it is possible to extrapolate back from both the anodic and cathodic regions to the point where the anodic and cathodic currents are equivalent. The current density at that point is the corrosion current density  $i_{corr}$  and the potential at which it falls is the corrosion potential  $E_{corr}$ .

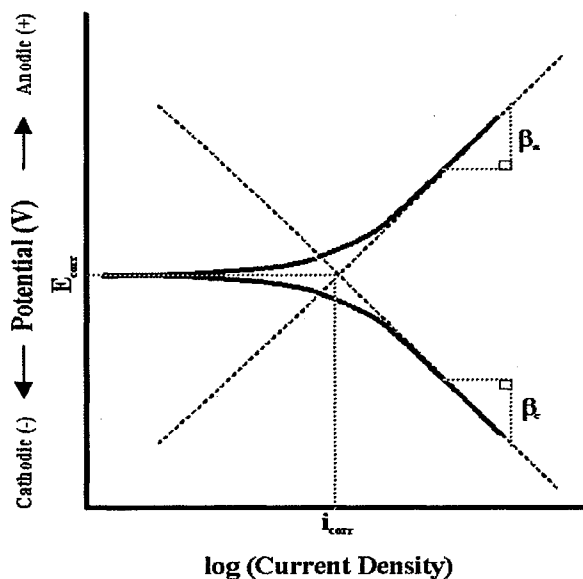


Figure 2.25 Tafel slope calculation.<sup>[61]</sup>

## 2.7.2 Electrochemical Impedance Spectroscopy (EIS)

EIS has been successfully applied to the study of corrosion systems for thirty years and been proven to be a powerful and accurate method for measuring corrosion rates. In contrast to polarization techniques, impedance measurements only require the application

of a small AC perturbation to the investigated samples, which has little or no effect on the integrity of materials. Therefore, it can virtually be considered as a non-destructive investigation method.

### 2.7.2.1 Impedance theory <sup>[62]</sup>

The concept of electrical resistance is well known and is defined by Ohm's law. Resistance is the ability of a circuit to resist the flow of current, mathematically expressed as

$$R = E / I$$

where R is resistance in ohms, E is voltage in volts, and I is current in amperes. While AC potential is applied as excitation signal, as shown in Figure 2.26, it could be expressed as a function of time,

$$E_t = E_0 \sin(\omega t)$$

$E_t$  is the potential at time t,  $E_0$  is the amplitude of the signal, and  $\omega$  is the radial frequency. The relationship between radial frequency  $\omega$  (expressed in radians/second) and frequency f (expressed in hertz) is:

$$\omega = 2\pi f$$

In a linear system, the response signal,  $I_t$ , is shifted in phase ( $\phi$ ) and has a different amplitude,  $I_0$ .

$$I_t = I_0 \sin(\omega t + \phi)$$

An expression analogous to Ohm's Law allows us to calculate the impedance of the system as:

$$Z = \frac{E_t}{I_t} = \frac{E_0 \sin(\omega t)}{I_0 \sin(\omega t + \phi)} = Z_0(\cos \phi + j \sin \phi)$$

Electrochemical Impedance is normally measured using a small excitation signal (5~50 mV) to obtain linearity or pseudo-linearity of the cell. In a linear (or pseudolinear) system, the current response to a sinusoidal potential will be a sinusoid at the same frequency but shifted in phase.

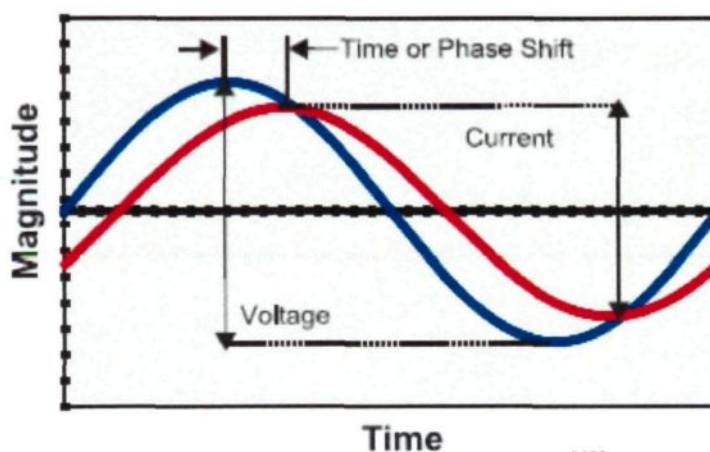


Figure 2.26 Sinusoidal current response in a linear system.<sup>[62]</sup>

The expression for impedance  $Z(\omega)$  is composed of a real and an imaginary part. If the real part is plotted on the X-axis and the imaginary part is plotted on the Y-axis of a chart, we get the "Nyquist Plot", see Figure 2.27. In this plot the Y-axis is negative and that each point on the Nyquist Plot is the impedance at one frequency. The low frequency data are on the right side of the plot and higher frequencies are on the left, the impedance can be expressed as a function of frequency  $f = \omega/2\pi$  as follows:

$$Z(j\omega) = R_s + \frac{R_p}{1 + j\omega C_d R_p}$$

The angle between this vector and the X-axis, commonly called the “phase angle”, is  $\phi$  ( $=\arg Z$ ). If the impedance and phase angle is plotted with log frequency, the plot is called the “Bode Plot”.

### 2.7.2.2 Impedance results interpretation <sup>[63]</sup>

The EIS instrument records the real (resistance) and imaginary (capacitance) components of the impedance response of the system. Depending upon the shape of the EIS spectrum, a circuit model and initial circuit parameters are assumed and input by the operator. The program then fits the best frequency response of the given EIS spectrum, to obtain fitting parameters. The quality of the fitting is judged by how well the fitting curve overlaps the original spectrum. By fitting the EIS data, it is possible to obtain a set of parameters which can be correlated well with the corrosion of the substrate.

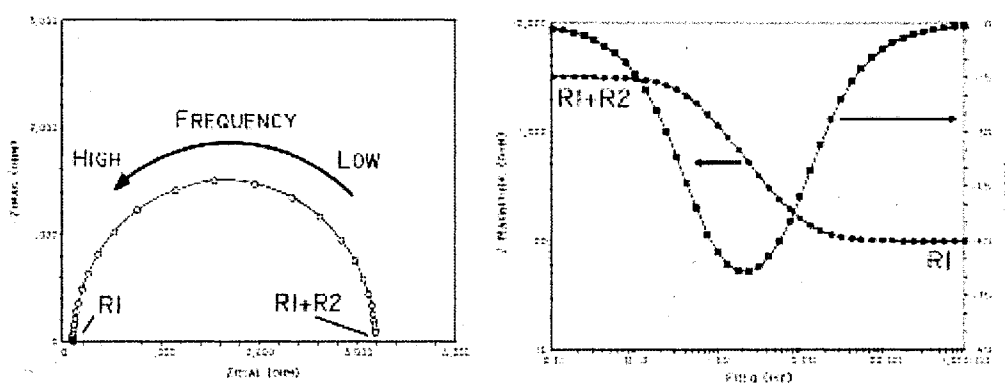


Figure 2.27 (a) Nyquist and (b) Bode plot for the Randle cell. <sup>[62]</sup>

The Nyquist plot in Figure 2.27 could be interpreted by equivalent circuit shown in Figure 2.28. For a corroding metal in an electrolyte solution,  $R_1$  is associated with the solution resistance  $R_s$ ,  $R_2$  is the polarization resistance  $R_p$  and the capacitor  $C$  is associated with the double layer capacitance  $C_{dl}$  of the metal/electrolyte interface. The capacitance

$C_{dl}$  can be obtained from the frequency  $f_{max}$  of the maximum of the imaginary impedance  $Z''$  and  $R_p$ :

$$C_{dl} = 1/2\pi f_{max} R_p$$

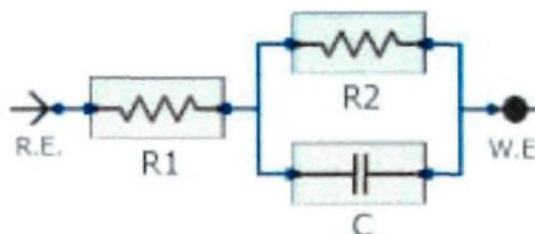


Figure 2.28 Simple equivalent circuit with one time constant.

However, in most cases reported so far, impedance data obtained at the corrosion potential  $E_{corr}$  have the shape of depressed semicircles with the centre of the circle below the real axis as shown in Figure 2.29. <sup>[64]</sup> Kending and Mansfeld <sup>[65]</sup> accounted for such deviation from the idea behavior by introducing an exponent  $a$  which leads to:

$$Z(j\omega) = R_s + \frac{R_p}{(1 + j\omega C_{dl} R_p)^a}$$

More recently, the concept of constant phase element (CPE) is proposed and Zoltowski <sup>[66]</sup> gave the impedance of CPE as

$$Z_{CPE} = \frac{1}{Q_a(j\omega)^a}$$

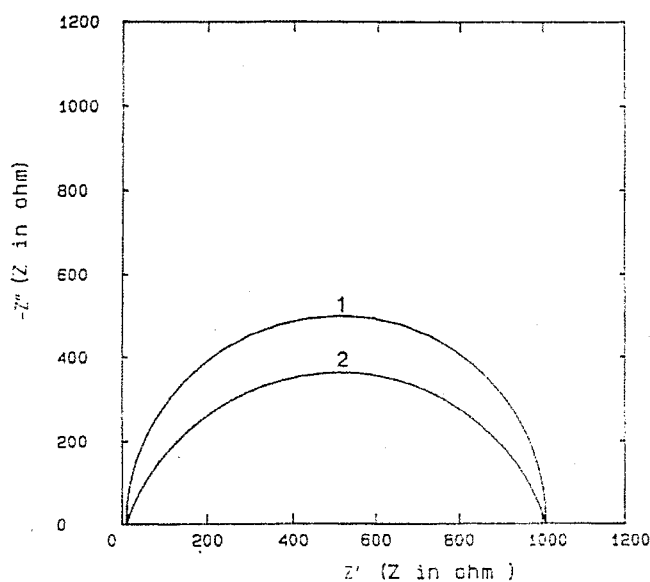


Figure 2.29 Nyquist plot showing the ideal semicircle (curve 1,  $\alpha=1.0$ ) and depressed semicircle (curve 2,  $\alpha=0.8$ ).<sup>[67]</sup>

Where  $Q_a$  is the double layer capacitance quantity and it is proportional to the active area.  $\alpha$  is the CPE power with  $-1 \leq \alpha \leq 1$ . For  $\alpha = 1$ , CPE represents a pure capacitance; for  $\alpha = 0$ , it is considered as a pure resistance; while  $\alpha = -1$ , it could be regarded as a pure inductance. In this case, the CPE becomes an extremely flexible fitting parameter, but its physical significance and relationship with the distribution of time constants is not clear.<sup>[68]</sup>

Bessone *et al.*<sup>[69]</sup> carried out AC-impedance measurements with the frequency range from  $5 \times 10^{-3}$  Hz to  $10^4$  Hz in the polycrystalline pure aluminum, 0.16M  $\text{NH}_4^+$  tartrate system at  $\text{pH}$  5-7, with the potential range of  $-900 \text{ mV} \leq E_H \leq 400 \text{ mV}$ . They found that the system is characterized by a high-frequency capacitive and a low-frequency inductive behavior. The capacitive loop is correlated to the dielectric properties of the barrier oxide film, and the inductive loop is determined mainly by the Faradic process of the system. They also

found that the capacitive semicircle decreases with increasing anodic potential in the potential range of  $800 \text{ mV} \leq E_H \leq 0 \text{ mV}$ , as shown in Figure 2.30. The effect of  $P^H$  value on the impedance of the system at a constant potential of  $E_H = 300 \text{ mV}$  was also investigated. They observed that the value of impedance decreases drastically with increasing  $P^H$ , whereas the shapes of the complex plane and Bode diagrams remain unchanged. The impedance diagrams were interpreted by the equivalent circuit given in Figure 2.31. The circuit consists of a capacitor  $C$  in parallel to the series resistor  $R_1$  and  $R_2$  and an inductance  $L$  in parallel to  $R_2$ .  $R_e$  corresponds to the electrolyte resistance.

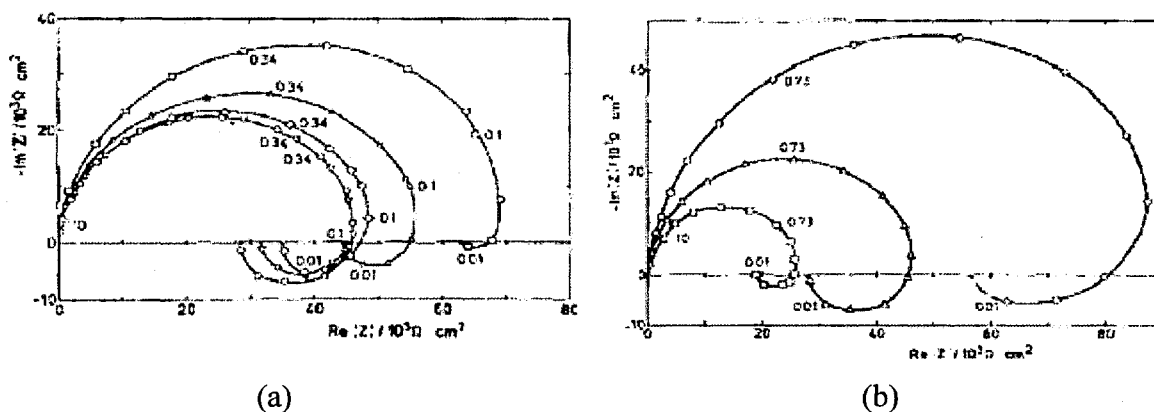


Figure 2.30 Nyquist plot of Al/0.16M  $\text{NH}_4^+$  tartrate at (a)  $P^H = 6$  and  $T = 298\text{K}$  with electrode potentials:  $-670 \text{ mV}$  ( $\square$ );  $-470 \text{ mV}$  ( $\Delta$ );  $-270 \text{ mV}$  ( $\diamond$ );  $-70 \text{ mV}$  ( $\bullet$ );  $+330 \text{ mV}$  ( $\circ$ ); (b)  $T = 298\text{K}$ ,  $E = 330 \text{ mV}$ ,  $P^H = 5$  ( $\circ$ );  $6$  ( $\Delta$ );  $7$  ( $\square$ ).<sup>[69]</sup>

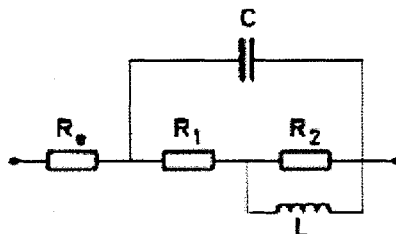


Figure 2.31 Equivalent circuit used to interpret the Nyquist plot in Figure 2.30.<sup>[69]</sup>

Frers *et al.* [70] performed impedance measurement on aluminum in 0.5 M NaCl in the frequency range from  $5 \times 10^{-4}$  Hz to  $10^4$  Hz and before the onset of pitting corrosion. They observed that the behavior of the system was characterized by a high frequency capacitive loop related to the thickness of the oxide film, and inductive loop at medium frequency, which was interpreted on the basis of the dielectric relaxation model proposed by Dignam [71], and a second capacitive loop obtained at low frequencies which was ascribed to the dissolution of the oxide film through the formation of a soluble chloride containing aluminum salt. The experimental results were interpreted in terms of electric equivalent circuit in Figure 2.32.  $R_1$ ,  $R_2$ ,  $R_3$ ,  $C$  and  $L$  are related to the faradic impedance, while  $C^*$  represents the capacity of the metal/film/electrolyte interface, it may be related to a series connection between the double layer capacity ( $C_{dl}$ ) and the oxide layer capacity ( $C_{ox}$ ), which was expressed as  $1/C^* = 1/C_{dl} + 1/C_{ox}$ .

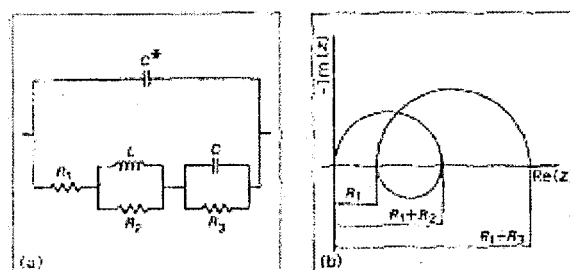


Figure 2.32 (a) Equivalent circuit for the total electrode impedance; (b) Nyquist plot for the circuit in (a) when  $1/CR_3 < R_2/L$ . [71]

Satochi *et al.* [72] also found the inductive loop when they carried out EIS experiments for 6000 series aluminum alloys in the 0.5 mol/L sulfuric acid solution. The experiments were conducted in both cathodic and anodic regions and they considered that

the occurrence of these inductive loops indicated the specimen was in the passive state even in the cathodic region.

Zucchi *et al.* <sup>[73]</sup> investigated the corrosion behavior of the AZ80A-20% SiCp and ZK60A-20% SiCp in 0.1 N and 1 N Na<sub>2</sub>SO<sub>4</sub> at 25 °C. It was observed that polarization resistance  $R_p$  decreased with increasing anion concentration. Nyquist plot showed a depressed capacitive semicircle followed by the beginning of a pseudo-inductive loop at frequency lower than 0.1 Hz. The high frequency loop was attributed to charge transfer and film effect, while the inductive loop was related to the relaxation process of absorbed species to the electrode surface. However, they found that the medium frequency capacitive loop in Mg alloys, which was attributed to the relaxation of mass transport in solid phase, was absent.

### 2.7.3 Zero Resistance Ammetry

Zero resistance ammetry has been used conventionally to determine the galvanic current between two dissimilar electrodes, but may also be used to determine the current between two nominally identical electrodes. ZRA is a current-to-voltage converter, which provides a voltage that is proportional to the current flowing between the input terminals when imposing a “zero” voltage drop to the external circuit. In the ZRA technique, a macro cell current is measured between two corroded sensor elements in an electrolytic environment. It is used for measuring the galvanic coupling current between two dissimilar or similar electrodes. The resultant galvanic current is a corrosion rate value which can be obtained through Faraday’s Law.

## References

- [1] D.B. Miracle, S.L. Donaldson, *ASM Handbook, Volume 21: Composites*, ASM International, 2001.
- [2] T.W. Clyne, P.J. Withers, *An Introduction to Metal Matrix Composites*, Cambridge University Press, Cambridge, 1993.
- [3] F. Thevenot, M. Bouchadourt, *L'industrie Ceramique*, 732 (1979) 655-667.
- [4] C. Brown, C.G. Interrante, L.R. Abramson, "Neutron Absorbers: Qualification and Acceptance Tests", in: *Proceeding of the 13<sup>th</sup> International Symposium on Packaging and Transportation of Radioactive Materials (PATRAM)*, (Eds.), 2001, pp. 201-205.
- [5] A.R. Kennedy, "The Microstructure and Mechanical Properties of Al-Si-B<sub>4</sub>C Metal Matrix Composites", *Journal of Materials Science*, 37 (2002) 317-323.
- [6] X.-G. Chen, "Application of Al-B<sub>4</sub>C Metal Matrix Composites in the Nuclear Industry for Neutron Absorber Materials", in: *Proceedings of the Symposium on Solidification Processing of Metal Matrix Composites*, W.H. Hunt and N. Gupta (Eds.), TMS, 2006, pp. 343-350.
- [7] A. Machiels, R. Lambert, *Handbook of Neutron Absorber Materials for Spent Nuclear Fuel Transportation and Storage Applications*, Palo Alto, 2006.
- [8] W.B. Eisen, B.L. Ferguson, R.M. German, R. Iacocca, P.W. Lee, D. Madan, K. Moyer, H. Sanderow, Y. Trudel, *ASM Handbook, Volume 07: Powder Metal Technologies and Applications* ASM International, 1998.
- [9] D.J. Lloyd, *Processing of Particle-Reinforced Metal Matrix Composites*, Marcel Dekker, Inc., New York, 1997.
- [10] Z. Zhang, A. Charette, Ghomashchi, X.-G. R. Chen, "Effect of Titanium on Solidification Microstructure of Al-16%B<sub>4</sub>C Composites", in: *44<sup>th</sup> Annual Conference of Metallurgist of CIM*, J.P. Martin (Eds.), The Metallurgical Society of CIM, 2005, pp. 447-456.
- [11] Z. Ahmad, B.J. Abdul Aleem, "Degradation of Aluminum Metal Matrix Composites in Salt Water and its Control", *Materials & Design*, 23 (2002) 173-180.
- [12] A.J. Trowsdale, B. Noble, S.J. Harris, I.S.R. Gibbins, G.E. Thompson, G.C. Wood, "The Influence of Silicon Carbide Reinforcement on the Pitting Behaviour of Aluminium", *Corrosion Science*, 38 (1996) 177-191.
- [13] Z. Zhang, X.G. Chen, A. Charette, "Microstructure Characterization of Al-7%Si-10%B<sub>4</sub>C Die Casting Composites", in: *Solidification Processing of Metal Matrix Composites: Rohatgi Honorary Symposium*, N. Gupta and W.H. Hunt (Eds.), John Wiley & Sons, 2006, pp. 173-178.

- [14] X.G. Chen, "Interface Reaction of Boron Carbide in Aluminum Matrix Composites and its Control", in: *EDP Congress 2005*, M.E. Schlesinger (Eds.), TMS, 2005, pp. 101-106.
- [15] US Stores Spent Nuclear Fuel Rods at 4 Times Pool Capacity, <http://coto2.wordpress.com/2011/03/26/us-stores-spent-nuclear-fuel-rods-at-4-times-pool-capacity>.
- [16] Nuclear Waste Storage, [http://library.thinkquest.org/17940/texts/nuclear\\_waste\\_storage/nuclear\\_waste\\_storage.html](http://library.thinkquest.org/17940/texts/nuclear_waste_storage/nuclear_waste_storage.html).
- [17] S.D. Cramer, J. B.S. Covino, *ASM Handbook, Vol.13A: Corrosion: Fundamentals, Testing and Protection*, ASM International, 2003.
- [18] F. Mansfeld, "Galvanic Corrosion of Al Alloys", *Werkstoffe und Korrosion*, 25 (1974) 578-586.
- [19] L.H. Hihara, R.M. Latanision, "Corrosion of Metal Matrix Composites", *International Materials Review*, 39 (1994) 245-263.
- [20] M.S.N. Bhat, M.K. Surappa, H.V.S. Nayak, "Corrosion Behaviour of Silicon Carbide Particle Reinforced 6061/Al Alloy Composites", *Journal of Materials Science*, 26 (1991) 4991-4996.
- [21] H. Sun, E.Y. Koo, H.G. Wheat, "Corrosion Behavior of SiCp/6061 Al Metal Matrix Composites", *Corrosion*, 47 (1991) 741-753.
- [22] I.B. Singh, D.P. Mandal, M. Singh, S. Das, "Influence of SiC Particles Addition on the Corrosion Behavior of 2014 Al-Cu Alloy in 3.5% NaCl Solution", *Corrosion Science*, 51 (2009) 234-241.
- [23] Z. Feng, C. Lin, J. Lin, J. Luo, "Pitting Behavior of SiCp/2024 Al Metal Matrix Composites", *Journal of Materials Science*, 33 (1998) 5637-5642.
- [24] L.H. Hihara, "Corrosion of Aluminum-Matrix Composites", *Corrosion Reviews*, 15 (1997) 361-386.
- [25] H. Ding, L. Hihara, "Electrochemical Behavior of Boron Carbide and Galvanic Corrosion of Boron Carbide Reinforced 6092 Aluminum Composites", *ECS Transactions*, 1 (2006) 103-114.
- [26] A. Bakkar, V. Neubert, "Corrosion Behaviour of Carbon Fibres/Magnesium Metal Matrix Composite and Electrochemical Response of its Constituents", *Electrochimica Acta*, 54 (2009) 1597-1606.
- [27] A. Turnbull, "Review of Corrosion Studies on Aluminium Metal Matrix Composites", *British Corrosion Journal*, 27 (1992) 27-35.

- [28] B. Dikici, M. Gavgali, C. Tekmen, "Corrosion Behaviour of an Artificially Aged (T6) Al-Si-Mg-based Metal Matrix composite", *Journal of Composite Materials*, 40 (2006) 1259-1269.
- [29] Y.L. Cheng, Z.H. Chen, H.L. Wu, H.M. Wang, "The Corrosion Behaviour of the Aluminum Alloy 7075/SiCp Metal Matrix Composite Prepared by Spray Deposition", *Materials and Corrosion*, 58 (2007) 280-284.
- [30] A. Pardo, S. Merino, M.C. Merino, I. Barroso, M. Mohedano, R. Arrabal, F. Viejo, "Corrosion Behaviour of Silicon-Carbide-Particle Reinforced AZ92 Magnesium Alloy", *Corrosion Science*, 51 (2009) 841-849.
- [31] P.P. Trzaskoma, "Pit Morphology of Aluminum Alloy and Silicon Carbide/Aluminum Alloy Metal Matrix Composites", *Corrosion*, 46 (1990) 402-409.
- [32] J.F. McIntyre, R.K. Conrad, S.L. Golledge, "Technical Note: The Effect of Heat Treatment on the Pitting Behavior of SiCw/AA2124", *Corrosion*, 46 (1990) 902-905.
- [33] T.M. Yue, Y.X. Wu, H.C. Man, "On the Role of Al<sub>2</sub>Cu Precipitation in Pitting Corrosion of Aluminum 2009/SiCw Metal Matrix Composite", *Journal of Materials Science Letters*, 19 (2003) 1003-1006.
- [34] H. Ding, L. Hihara, "Localized Corrosion Currents and pH Profile Over B<sub>4</sub>C, SiC, and Al<sub>2</sub>O<sub>3</sub> Reinforced 6092 Aluminum Composites: I. In 0.5 M Na<sub>2</sub>SO<sub>4</sub> Solution", *Journal of the Electrochemical Society*, 152 (2005) B161-B167.
- [35] S.L. Winkler, M.P. Ryan, H.M. Flower, "Pitting Corrosion in Cast 7XXX Aluminium Alloys and Fibre Reinforced MMCs", *Corrosion Science*, 46 (2004) 893-902.
- [36] R. Emmerich, W. Ensinger, B. Enders, "Corrosion Behaviour of Borated Aluminium Used as a Neutron Absorber", *Journal of European Archaeology*, 16 (2005) 151-156.
- [37] Z.F. Yin, M.L. Yan, Z.Q. Bai, W.Z. Zhao, W.J. Zhou, "Galvanic Corrosion Associated With SM 80SS Steel and Ni-Based Alloy G3 Couples in NaCl Solution", *Electrochimica Acta*, 53 (2008) 6285-6292.
- [38] R. Francis, "Galvanic Corrosion of High Alloy Stainless Steels in Sea Water", *British Corrosion Journal*, 29 (1994) 53-57.
- [39] F. Mansfeld, D.H. Hengstenberg, J.V. Kenkel, "Galvanic Corrosion of Al Alloys - 1. Effect of Dissimilar Metal", *Corrosion*, 30 (1974) 343-353.
- [40] F. Mansfeld, J.V. Kenkel, "Laboratory Studies of Galvanic Corrosion- 1. Two-Metal Couples", *Corrosion*, 31 (1975) 298-302.
- [41] F. Mansfeld, J.V. Kenkel, "Galvanic Corrosion of Al Alloys - II. Effect of Solution Composition", *Corrosion Science*, 15 (1975) 183-198.

- [42] F. Mansfeld, J.V. Kenkel, "Galvanic Corrosion of Al Alloys-III. The Effect of Area Ratio", *Corrosion Science*, 15 (1975) 239-250.
- [43] B.D. Craig, R.A. Lane, D.H. Rose, *Corrosion Prevention and Control: A Program Management Guide for Selecting Materials, spiral 2 (2nd edition)*, Advanced Materials and Processes Technology Information Analysis Center (AMPTIAC), New York, 2005.
- [44] S. Lin, H. Greene, H. Shih, F. Mansfeld, "Corrosion Protection of Al/SiC Metal Matrix Composites by Anodizing", *Corrosion*, 48 (1992) 61-67.
- [45] H.J. Greene, F. Mansfeld, "Corrosion Protection of Aluminum Metal-Matrix Composites", *Corrosion (Houston)*, 53 (1997) 920-927.
- [46] F. Mansfeld, S.L. Jeanjaquet, "The Evaluation of Corrosion Protection Measures for Metal Matrix Composites", *Corrosion Science*, 26 (1986) 727-734.
- [47] A.K. Mishra, R. Balasubramaniam, S. Tiwari, "Corrosion Inhibition of 6061-SiC by Rare Earth Chlorides", *Anti-Corrosion Methods and Materials*, 54 (2007) 37-46.
- [48] Z. Ahmad, B.J.A. Aleem, "The Effect of Inhibitors on the Susceptibility of Al 6013/SiC Interface to Localized Corrosion", *Journal of Materials Engineering and Performance*, 18 (2009) 129-136.
- [49] K.D. Ralston, S. Chrisanti, T.L. Young, R.G. Buchheit, "Corrosion Inhibition of Aluminum Alloy 2024-T3 by Aqueous Vanadium Species", *Journal of the Electrochemical Society*, 155 (2008) C350-C359.
- [50] G. Bereket, A. Pinarbaşı, "Electrochemical Thermodynamic and Kinetic Studies of the Behaviour of Aluminium in Hydrochloric Acid Containing Various Benzotriazole Derivatives", *Corrosion Engineering Science and Technology*, 39 (2004) 308-312.
- [51] V. Branzoi, F. Golgovici, F. Branzoi, "Aluminium Corrosion in Hydrochloric Acid Solutions and the Effect of Some Organic Inhibitors", *Materials Chemistry and Physics*, 78 (2003) 122-131.
- [52] Z. Grubač, R. Babić, M. Metikoš-Huković, "Application of Substituted N-arylpyrroles in the Corrosion Protection of Aluminium in Hydrochloric Acid", *Journal of Applied Electrochemistry*, 32 (2002) 431-438.
- [53] M. Abdallah, "Antibacterial Drugs As Corrosion Inhibitors For Corrosion of Aluminium in Hydrochloric Solution", *Corrosion Science*, 46 (2004) 1981-1996.
- [54] K.F. Khaled, M.M. Al-Qahtani, "The Inhibitive Effect of Some Tetrazole Derivatives Towards Al Corrosion in Acid Solution: Chemical, Electrochemical and Theoretical Studies", *Materials Chemistry and Physics*, 113 (2009) 150-158.
- [55] T. Kosec, I. Milošev, B. Pihlar, "Benzotriazole As An Inhibitor of Brass Corrosion in Chloride Solution", *Applied Surface Science*, 253 (2007) 8863-8873.

- [56] F.M. Bayoumi, A.M. Abdullah, B. Attia, "Kinetics of Corrosion Inhibition of Benzotriazole to Copper in 3.5% NaCl", *Materials and Corrosion*, 59 (2008) 691-696.
- [57] K. Babić-Samardžija, N. Hackerman, "Triazole, Benzotriazole and Substituted Benzotriazoles as Corrosion Inhibitors of Iron in Aerated Acidic Media", *Journal of Solid State Electrochemistry*, 9 (2005) 483-497.
- [58] J.L. Yao, B. Ren, Z.F. Huang, P.G. Cao, R.A. Gu, Z.Q. Tian, "Extending Surface Raman Spectroscopy to Transition Metals for Practical Applications IV. A Study on Corrosion Inhibition of Benzotriazole on Bare Fe Electrodes", *Electrochimica Acta*, 48 (2003) 1263-1271.
- [59] V. Palanivel, Y. Huang, W.J. Van Ooij, "Effects of Addition of Corrosion Inhibitors to Silane Films on the Performance of AA2024-T3 in a 0.5 M NaCl Solution", *Progress in Organic Coatings*, 53 (2005) 153-168.
- [60] A.J. Bard, L.R. Faulkner, *Electrochemical Methods: Fundamentals and Applications, 2nd Edition*, John Wiley & Sons, 2001.
- [61] D.G. Enos, L.L. Scribner, The Potentiodynamic Polarization Scan, Technical Report 33, Solartron Instruments, 1997.
- [62] Basics of Electrochemical Spectroscopy, Gamry Instrument, 2007.
- [63] D. Loveday, P. Peterson, B. Rodgers, Evaluation of Organic Coatings with Electrochemical Impedance Spectroscopy *Part 1: Fundamentals of Electrochemical Impedance Spectroscopy*, Gamry Instrument, 2004.
- [64] F. Mansfeld, "Recording and Analysis of AC Impedance Data for Corrosion Studies", *Corrosion*, 37 (1981) 301-307.
- [65] F. Mansfeld, M. Kendig, W. Lorenz, "Corrosion Inhibition in Neutral, Aerated Media", *Journal of the Electrochemical Society*, 132 (1985) 290-296.
- [66] P. Zoltowski, "On the Electrical Capacitance of Interfaces Exhibiting Constant Phase Element Behaviour", *Journal of Electroanalytical Chemistry*, 443 (1998) 149-154.
- [67] F. Mansfeld, Analysis and Interpretation of EIS Data for Metals and Alloys, Solartron Analytical, 1999.
- [68] J.R. Macdonald, W.R. Kenan, *Impedance Spectroscopy: Emphasizing Solid Materials and Systems*, John Wiley & Sons, 1987.
- [69] J. Bessone, C. Mayer, K. Jüttner, W.J. Lorenz, "AC-Impedance Measurements on Aluminium Barrier Type Oxide Films", *Electrochimica Acta*, 28 (1983) 171-175.
- [70] S.E. Frers, M.M. Stefenel, C. Mayer, T. Chierchie, "AC-Impedance Measurements on Aluminium in Chloride Containing Solutions and Below the Pitting Potential", *Journal of Applied Electrochemistry*, 20 (1990) 996-999.

- [71] D.F. Taylor, M.J. Dignam, "Transient Response of the System Ta/Ta<sub>2</sub>O<sub>5</sub>/Electrolyte II: Investigation of Faradaic-Current-Driven Polarization Processes", *Journal of the Electrochemical Society*, 120 (1973) 1306-1310.
- [72] S. Sunada, S. Sada, N. Nunomura, K. Majima, "Electrochemical Impedance Characteristics of 6000 Series Aluminum Alloys Produced by Conventional and Powder Extruded Methods", *Aluminum Alloys: Their Physical and Mechanical Properties*, 2 (2008) 2048-2053.
- [73] F. Zucchi, G. Trabanelli, V. Grassi, A. Frignani, "Corrosion Behavior in Sodium Sulfate and Sodium Chloride Solutions of SiCp Reinforced Magnesium Alloy Metal Matrix Composites", *Corrosion*, 60 (2004) 362-368.

## **CHAPTER 3**

### **EXPERIMENTAL PROCEDURES**

## CHAPTER 3

### EXPERIMENTAL PROCEDURES

#### 3.1 Sample Preparation and Solutions

The metal matrix composite Al-B<sub>4</sub>C fabricated by Rio Tinto Alcan (Saguenay, Quebec, Canada) was used in the present study. The designate chemical composition of AA1100 base alloy is listed in Table 3.1. It should be mentioned that the actual chemical composition of AA1100 used by RioTinto Alcan is not displayed since it varies with different batches. But most of trace elements were in the very low level range, which might not affect the corrosion behavior of the composite. For example, Nickel, Copper and Zinc contents were always below 0.012, 0.001 and 0.002 wt. %, respectively. The composites were produced using the liquid metal mixing technique. During the mixing process, ~ 0.5-1.5 wt. % titanium was added to the molten aluminum to reduce the interfacial reactions and ensure a uniform distribution of B<sub>4</sub>C particles in the matrix. <sup>[1]</sup> To study the effect of B<sub>4</sub>C particles volume fraction on the corrosion behavior of composites, two composites with 16 vol.% and 30 vol.% B<sub>4</sub>C particles (noted as AA1100-16 vol.% B<sub>4</sub>C and AA1100-30 vol.% B<sub>4</sub>C) as well as AA1100 base alloy in the form of rolled sheets, were used.

Table 3.1 Designate chemical composition of the base alloy AA1100.

| Elements               | Al          | Cu         | Mn           | Si+Fe       | Zn          | other       |
|------------------------|-------------|------------|--------------|-------------|-------------|-------------|
| Composition<br>(wt. %) | $\geq 99.0$ | 0.050-0.20 | $\leq 0.050$ | $\leq 0.95$ | $\leq 0.10$ | $\leq 0.15$ |

All samples were cut into small pieces of  $20 \times 20$  mm with a thickness of 4.3 mm. Two kinds of surface preparation were used: (1) Sanded with 3M Scotch-Brite™ MMM69412 surface conditioning disc (5 inches in diameter, xfine surface finish); (2) Mounted in epoxy resin, then grounded and polished to a  $0.05 \mu\text{m}$  fine finish. After sanding or polishing, samples were cleaned with soapy water or acetone, rinsed with deionized water, and dried with clean compressed air. Finally, samples were desiccated before carrying out the corrosion measurements.

The whole project was divided into four parts. Are listed below the materials, solutions and surface treatment method used in each part:

***Part 1: study the corrosion susceptibility of Al-B<sub>4</sub>C metal matrix composite in H<sub>3</sub>BO<sub>3</sub>, K<sub>2</sub>SO<sub>4</sub> and NaCl solutions***

- ✓ Materials:(1) AA1100
  - (2) AA1100-16 vol.% B<sub>4</sub>C
  - (3) AA1100-30 vol.% B<sub>4</sub>C
- ✓ Solutions:(1) 2500 ppm boron-containing H<sub>3</sub>BO<sub>3</sub>
  - (2) 0.5 M K<sub>2</sub>SO<sub>4</sub>
  - (3) 35g/L NaCl

- ✓ Surface treatment: Scotch-Brite sanded

***Part 2: Corrosion mechanism of Al-B<sub>4</sub>C MMCs in 0.5 M K<sub>2</sub>SO<sub>4</sub> solution***

- ✓ Materials: AA1100-16 vol.% B<sub>4</sub>C
- ✓ Solutions: 0.5 M K<sub>2</sub>SO<sub>4</sub>
- ✓ Surface treatment: polished to a 0.05 μm fine finish

***Part 3: Corrosion inhibition of Al-B<sub>4</sub>C MMCs in 3.5g/L NaCl solution by benzotriazole***

- ✓ Materials:(1) AA1100  
(2) AA1100-16 vol.% B<sub>4</sub>C  
(3) AA1100-30 vol.% B<sub>4</sub>C
- ✓ Solutions: 3.5 g/L NaCl
- ✓ Surface treatment: Scotch-Brite sanded

***Part 4: Galvanic coupling effect of Al-B<sub>4</sub>C MMCs associated with SS304 and AA6061***

- ✓ Materials: (1) AA1100  
(2) AA1100-16 vol.% B<sub>4</sub>C  
(3) AA1100-30 vol.% B<sub>4</sub>C
- ✓ Solutions: (1) 2500 ppm boron-containing H<sub>3</sub>BO<sub>3</sub>  
(2) 35g/L NaCl
- ✓ Surface treatment: Scotch-Brite sanded.

### 3.2 Electrochemical Experiments

Electrochemical experiments were performed at ambient temperature (around 21°C), in open to air condition if not otherwise mentioned. A 300 cm<sup>3</sup> - EG&G PAR flat cell (London Scientific, London, ON, Canada) linked to a Reference 600 instrument potentiostat/zero resistance ammeter (ZRA) (Gamry Instruments, Warminster, PA, USA) was used. In the three-electrode system, Ag/AgCl electrode was used as reference electrode (RE), a platinum mesh as the counter electrode (CE), and the sample as the working electrode (WE). The exposed surface of working electrode was 1 cm<sup>2</sup>, if not otherwise mentioned. Prior to electrochemical impedance spectroscopy (EIS) and potentiodynamic polarization (PDP) measurements, samples were immersed in the solution for 1 to 3 hours to reach a steady open circuit potential ( $E_{ocp}$ ). Magnetic stirring was employed at cell bottom to increase mass transfer at the electrode surface. Electrochemical impedance curves were obtained by applying a sinusoidal potential of 10 mV in amplitude around  $E_{ocp}$  at a steady-state, in the frequency range from 100 kHz to 10 mHz. Potentiodynamic polarization tests were performed at a scan rate of 1 mV s<sup>-1</sup> with the scans being taken from -250 mV below  $E_{ocp}$ . In the galvanic corrosion test, the investigated materials was used as working electrode #1, while AA6061 or SS304 materials were considered as working electrode #2. The variations in galvanic current and galvanic potential were continuously recorded for 24 hours. All the tests were conducted in duplicate to guarantee the reliability of results.

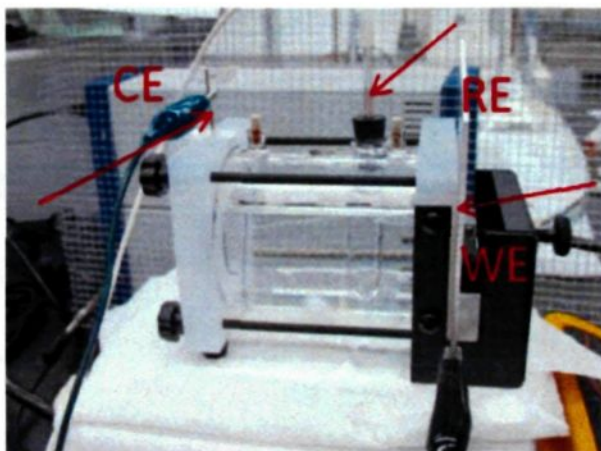


Figure 3.1 EG&G PAR flat cell used in the present study and the three-electrode system.

### 3.3 Microstructural Analysis

An optical microscope (CLEMEX JS-2000) and a scanning electron microscope equipped with an energy dispersive spectrometer (EDS) (Hitachi SU-70) were used to characterize the microstructure before and after the corrosion tests. To investigate the topographic profile of the composite surface before and after corrosion, a STIL confocal profilometer (CHR150-L) equipped with an optical pen MG140 was employed.



Figure 3.2 Image of scanning electron microscope used in the present study.

### 3.4 Infrared Reflection-Absorption Spectroscopy

Infrared reflection-absorption spectroscopy (IRRAS) was used as a complementary tool to analyze the corrosion products. The IRRAS accessory operated using a Nicolet 6700 spectrometer (ThermoFisher Scientific) equipped with a Mid-IR MCT-B wide band N<sub>2</sub>-cooled detector and a XT-KBr beam splitter. The Smart SAGA (Specular Apertured Grazing Angle) accessory was used to analyze samples at an average incidence angle of 80° relative to the normal surface. The spectra were recorded from 4000 to 600 cm<sup>-1</sup> with a resolution of 4 cm<sup>-1</sup> and 64 scans.

### 3.5 X-Ray Photoelectron Spectroscopy

The X-ray photoelectron spectra (XPS) were recorded with a model AXIS\_ULTRA Kratos photoelectron spectrometer, using a monochromatic Al K- $\alpha$  radiation (1486.6 eV), in a UHV system, and kept at about 10<sup>-8</sup> mbar during the analysis. The anode voltage was 15 kV and the emission current 20 mA. For each sample, high resolution scans for C1s, Al2p, O1s, B1s and Ti2p were recorded with a 0.5 eV resolution, followed by a high sensitivity survey scan recorded at a 1.8 eV resolution.

### References

- [1] Z. Zhang, A. Charette, Ghomashchi, X.-G. R. Chen, "Effect of Titanium on Solidification Microstructure of Al-16%B<sub>4</sub>C Composites", in: *44th Annual Conference of Metallurgist of CIM*, J.P. Martin (Eds.), The Metallurgical Society of CIM, 2005, pp. 447-456.

## **CHAPTER 4**

### **CORROSION BEHAVIOUR OF Al-B<sub>4</sub>C METAL MATRIX COMPOSITES IN H<sub>3</sub>BO<sub>3</sub>, K<sub>2</sub>SO<sub>4</sub> AND NaCl SOLUTIONS**

## CHAPTER 4

### CORROSION BEHAVIOUR OF Al-B<sub>4</sub>C METAL MATRIX COMPOSITES IN H<sub>3</sub>BO<sub>3</sub>, K<sub>2</sub>SO<sub>4</sub> AND NaCl SOLUTIONS

#### Abstract

The corrosion behavior of Al-B<sub>4</sub>C metal matrix composites immersed in 2500 ppm boron-containing H<sub>3</sub>BO<sub>3</sub>, 0.5 M K<sub>2</sub>SO<sub>4</sub>, and 3.5% NaCl solutions was investigated. Effects of B<sub>4</sub>C particle volume fraction on the corrosion behavior of composites were studied using potentiodynamic polarization and electrochemical impedance spectroscopy techniques. Scanning electron microscopy was employed to study the surface morphology of the material before and after corrosion. Results show that all materials investigated are more corrosion resistant in 2500 ppm boron-containing H<sub>3</sub>BO<sub>3</sub> than in other solutions. No appreciable corrosion was observed in boric acid and sulfate solutions in contrast to an obvious pitting in NaCl solution for both base alloy and composites. The preferential pitting sites are the interfaces of Al/Fe intermetallics for the base alloy, and the Al/B<sub>4</sub>C interfaces for the composites. Increasing the volume fraction of B<sub>4</sub>C particles in the composite decreases its corrosion resistance of Al-B<sub>4</sub>C composites.

## 4.1 Introduction

Al-B<sub>4</sub>C metal matrix composite (MMCs) is being considered as new advanced materials due to its light weight, superior thermal conductivity, high stiffness and hardness.<sup>[1]</sup> Recently, due to the special ability of the <sup>10</sup>B isotope to capture neutrons, Al-B<sub>4</sub>C composite has been extensively used as an excellent neutron absorber material to fabricate the inside baskets of storage and transport containers of the spent nuclear fuel.<sup>[2-4]</sup>

Although the incorporation of B<sub>4</sub>C particles into the Al matrix can enhance the physical and mechanical properties of the base material, it may also change its corrosion behavior.<sup>[5]</sup> Bhat *et al.*<sup>[6]</sup> investigated the corrosion behaviour of 6061 Al-SiCp composite and its base alloy in seawater using potentiodynamic polarization technique. It was found that the composite corroded faster than its base alloy. Furthermore, the corrosion of the composites was mainly confined to the interfaces between Al and ceramic particles, as opposite to the uniform corrosion observed for the base alloy. Sun *et al.*<sup>[7]</sup> also studied the corrosion behaviour of 6061 Al-SiCp MMCs in NaCl solution. It was observed that the pitting degree rose with an increasing SiC content. They presumed that more SiC particles incorporated could result in more film disruption and consequently more pit initiation sites. Differently, results of Singh *et al.*<sup>[8]</sup> revealed that addition of 10 wt. % SiC to the base alloy 2014 increases its corrosion resistance. However, addition of 25 wt. % SiC to the 2014 alloy decreases the corrosion resistance.

As neutron absorber material used in the spent fuel storage racks or transportation casks, Al-B<sub>4</sub>C MMCs are placed between spent nuclear fuel assemblies. In the wet storage

application, Al-B<sub>4</sub>C MMCs are continuously in contact with the reactor pool water (*i.e.* one of them is the boric acid with B concentration of ~2500 ppm), which is generally considered to be mildly corrosive.<sup>[9]</sup> Thus, from the safety consideration, it is of paramount importance to understand their corrosion behaviour in boric acid solution. However, up to date, quite limited studies have been devoted to the corrosion behaviour of the Al-B<sub>4</sub>C MMCs,<sup>[9-11]</sup> especially in boric acid, in contrast to considerable research in the corrosion behaviour of Al-SiC,<sup>[5-8, 10, 12-22]</sup> and Al-Al<sub>2</sub>O<sub>3</sub> composites<sup>[23-26]</sup> in various environments. Among literatures on corrosion, 3.5% NaCl and 0.5 M K<sub>2</sub>SO<sub>4</sub> are the most commonly used solutions in studying the corrosion behaviour of the composites. The present paper investigates, using electrochemical measurements and scanning electron microscopy, the corrosion susceptibilities of Al-B<sub>4</sub>C metal matrix composites in 2500 ppm boron-containing H<sub>3</sub>BO<sub>3</sub> in comparison with those in 0.5 M K<sub>2</sub>SO<sub>4</sub> and 3.5% NaCl solutions.

## 4.2 Materials and Methods

The matrix of composite is AA1100 alloy, whose composition is listed in Table 4.1. Composites with two volume fractions of B<sub>4</sub>C particles ( $V_F = 16\%$  and  $V_F = 30\%$ ) were investigated. The mean size of B<sub>4</sub>C particles was 17 and 23  $\mu\text{m}$ , respectively. AA1100 alloy without B<sub>4</sub>C particles ( $V_F = 0\%$ ) was used for comparison purpose. All materials used in the present study were fabricated by Rio Tinto Alcan (Saguenay, Quebec, Canada). Samples were cut into small pieces of 20  $\times$  20 mm with a thickness of 4.3 mm, sanded with 3M Scotch-Brite™ MMM69412 surface conditioning disc (5 inches in diameter, xfine

surface finish), degreased with acetone and then rinsed with deionized water. Finally, all specimens were dried with clean compressed air.

Table 4.1 Chemical composition of the base alloy AA1100.

| Elements            | Al          | Cu         | Mn           | Si+Fe       | Zn          | other       |
|---------------------|-------------|------------|--------------|-------------|-------------|-------------|
| Composition (wt. %) | $\geq 99.0$ | 0.050-0.20 | $\leq 0.050$ | $\leq 0.95$ | $\leq 0.10$ | $\leq 0.15$ |

Electrochemical experiments were performed at ambient temperature (about 21°C), in solutions open to air. The three solutions used were 2500 ppm boron-containing  $\text{H}_3\text{BO}_3$ , 0.5 M  $\text{K}_2\text{SO}_4$  and 3.5% NaCl. Electrochemical investigations were performed using a 300  $\text{cm}^3$  - EG&G PAR flat cell (London Scientific, London, ON, Canada) making use of a Reference 600 instrument potentiostat (Gamry Instruments, Warminster, PA, USA). A standard three-electrode system was used with an Ag/AgCl electrode as reference electrode (RE), a platinum mesh as the counter electrode (CE), and the sample as the working electrode (WE). The exposed surface of working electrode was 1  $\text{cm}^2$ . Prior to electrochemical measurements, the samples were immersed in the solution for 1 to 3 hours to obtain steady open circuit potential ( $E_{\text{ocp}}$ ). Magnetic stirring was employed at cell bottom to increase mass transfer at the electrode surface. Electrochemical impedance curves were obtained by applying a sinusoidal potential of 10 mV in amplitude around  $E_{\text{ocp}}$  at a steady-state, in the frequency range from 100 kHz to 10 mHz. Potentiodynamic polarization tests were performed at a scan rate of 1  $\text{mV s}^{-1}$ . All the tests were conducted in duplicate to guarantee the reliability of results.

The characterization of surface morphology was performed using a scanning electron microscope Hitachi Model SU-70 (Hitachi High-Technologies, Rexdale, ON, Canada) equipped with an energy dispersive spectrometer.

### **4.3 Results and Discussion**

#### **4.3.1 Potentiodynamic Polarization**

Within the framework of a corrosion study, the aim of potentiodynamic polarization technique is to bring the potential of a material out of its quasi-equilibrium state and, thereafter, to investigate its corrosion behavior by measuring currents and observing other specific electrochemical signatures. Indeed, while potentiodynamic curves are mainly used to calculate corrosion current densities in the vicinity of the corrosion potential, they can also be applied to investigate different distinctive features such as the existence of a passive film, the susceptibility to pitting corrosion of a material, the stability of a surface over a wide range of potentials, etc. In laboratory, polarization experiments have the ability to rapidly indicate the corrosion behavior of a material in a specific environment whose composition simulates real service conditions.

Potentiodynamic polarization curves recorded for the Al-B<sub>4</sub>C composites and the base alloy AA1100 in boric acid, potassium sulphate and sodium chloride solutions are shown in Figures 4.1, 4.2, and 4.3, respectively. The polarization scan started from - 250 mV vs. E<sub>ocp</sub> for all the tests and terminated at + 1000 mV vs. Ag/AgCl for boric acid and sulphate solutions but terminated at 1 mA.cm<sup>-2</sup> for the NaCl solution. Corrosion current density ( $j_{\text{corr}}$ ) and corrosion potential (E<sub>corr</sub>) derived from these polarization curves are all

summarized in Table 4.2. Corrosion current densities reported in this paper were calculated from the extrapolation of the cathodic polarization branch, as shown in Figure 4.4.

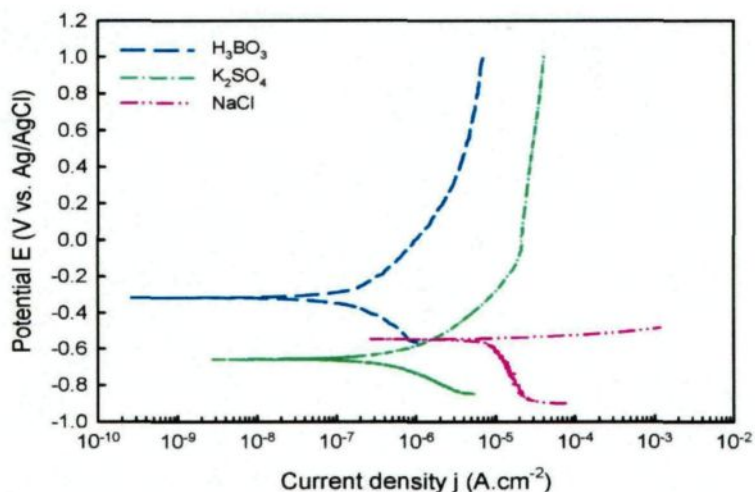


Figure 4.1 Potentiodynamic polarization curves recorded on AA1100-16 vol. % B<sub>4</sub>C in 2500 ppm boron-containing H<sub>3</sub>BO<sub>3</sub>, 0.5 M K<sub>2</sub>SO<sub>4</sub> and 3.5% NaCl.

Figure 4.1 presents the polarization curve of AA1100-16 vol. % B<sub>4</sub>C in three solutions. It is observed that with the same B<sub>4</sub>C particles volume fraction, current density  $j_{\text{corr}}$  in H<sub>3</sub>BO<sub>3</sub> (*i.e.* 0.18  $\mu\text{A}\cdot\text{cm}^{-2}$ ) is always smaller than those in sulfate (0.39  $\mu\text{A}\cdot\text{cm}^{-2}$ ) and chloride solutions (8.39  $\mu\text{A}\cdot\text{cm}^{-2}$ ). The same observation was obtained for AA1100-30 vol. % B<sub>4</sub>C and base alloy, as shown in Figures 4.2 and 4.3, which suggests that both composites and base alloy are more corrosion resistant in 2500 ppm boron-containing H<sub>3</sub>BO<sub>3</sub> (which is used in the wet storage of spent nuclear fuel) than in other two solutions.

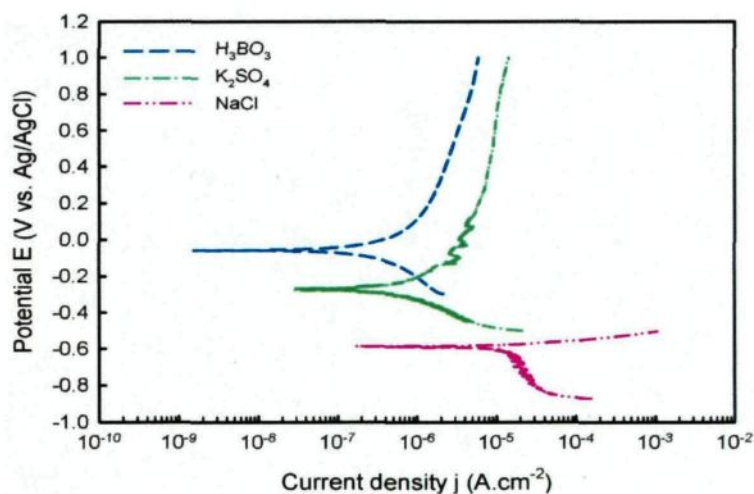


Figure 4.2 Potentiodynamic polarization curves recorded on AA1100-30 vol. % B<sub>4</sub>C in 2500 ppm boron-containing H<sub>3</sub>BO<sub>3</sub>, 0.5 M K<sub>2</sub>SO<sub>4</sub> and 3.5% NaCl.

It is noted from Figures 4.1 and 4.2 that in NaCl solution, the current density recorded for composites increases steeply to 1 mA.cm<sup>-2</sup> even under low overpotential, and this indicates the occurrence of pitting at  $E > E_{\text{corr}}$ . For the AA1100 base alloy, current oscillations due to competition between passivation and pitting at potentials slightly positive to  $E_{\text{corr}}$  were observed. However, as potential further increased, current density suddenly increases, suggesting the definite occurrence of pitting. The sudden increase in current density is not observed in K<sub>2</sub>SO<sub>4</sub> and H<sub>3</sub>BO<sub>3</sub> solutions. Therefore, it may be concluded that all three materials investigated are susceptible to pitting attack by chloride ion at either rest potential or under low polarization states.

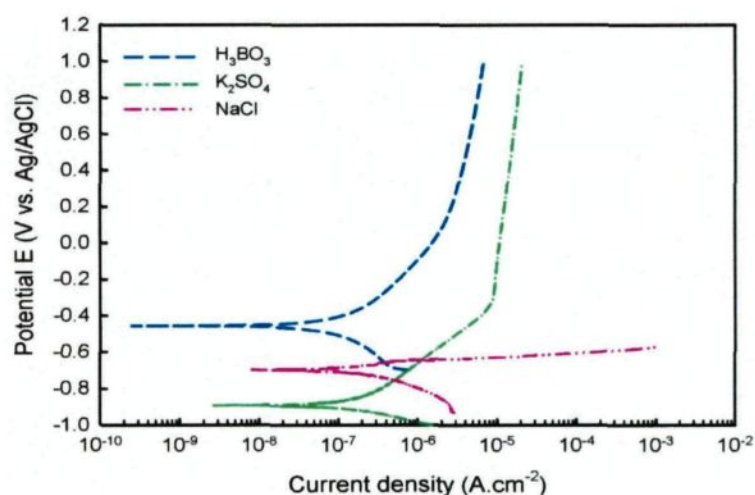


Figure 4.3 Potentiodynamic polarization curves recorded on base alloy AA1100 in 2500 ppm boron-containing  $\text{H}_3\text{BO}_3$ , 0.5 M  $\text{K}_2\text{SO}_4$  and 3.5% NaCl.

Table 4.2 Electrochemical parameters derived from polarization curves.

| Materials                             | 2500 ppm B $\text{H}_3\text{BO}_3$ |   | 0.5 M $\text{K}_2\text{SO}_4$ |   | 3.5% NaCl                 |   |
|---------------------------------------|------------------------------------|---|-------------------------------|---|---------------------------|---|
|                                       | $E_{\text{corr}}$<br>(mV)          | $j_{\text{corr}}$<br>( $\mu\text{A}\cdot\text{cm}^{-2}$ ) | $E_{\text{corr}}$<br>(mV)     | $j_{\text{corr}}$<br>( $\mu\text{A}\cdot\text{cm}^{-2}$ ) | $E_{\text{corr}}$<br>(mV) | $j_{\text{corr}}$<br>( $\mu\text{A}\cdot\text{cm}^{-2}$ ) |
| AA1100                                | -457                               | 0.10  | -892                          | 0.11  | -700                      | 0.345   |
| AA1100-16 vol. % $\text{B}_4\text{C}$ | -318                               | 0.18  | -660                          | 0.39  | -548                      | 8.39  |
| AA1100-30 vol. % $\text{B}_4\text{C}$ | -57                                | 0.35  | -269                          | 0.52  | -587                      | 11.2  |

It is also observed from Figure 4.2 that the anodic polarization curve of AA1100-30 vol. %  $\text{B}_4\text{C}$  in sulphate solution presents a potential region where current oscillations are recorded. This may be associated with a metastable process due to competition between passivation and dissolution of the matrix. Over this region, at potentials greater than +200 mV vs. Ag/AgCl reference electrode, the current density stabilizes, which suggests that the passivation process overtakes dissolution phenomenon. In the boric acid solution, passive behaviour is clearly observed for all specimens investigated.

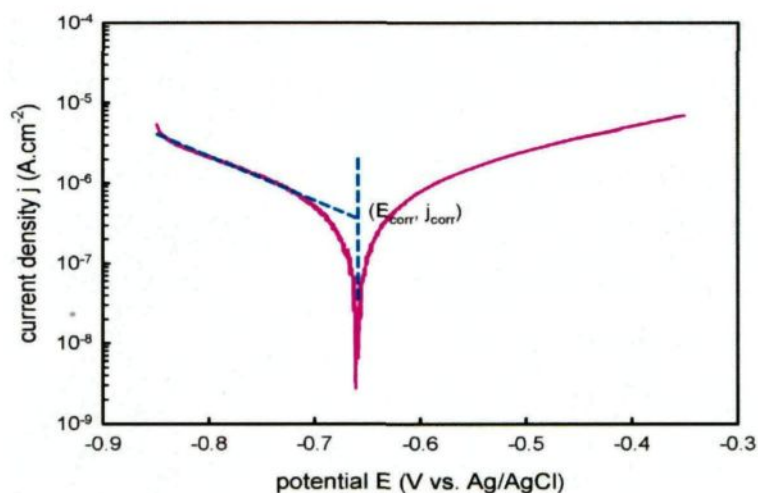


Figure 4.4 Tafel plot of AA1100-16 vol. % B<sub>4</sub>C in 0.5 M K<sub>2</sub>SO<sub>4</sub> showing that  $j_{\text{corr}}$  value is obtained by the intersection of the extrapolated cathodic branch at the corrosion potential.

From Table 4.2, it could be seen that in the same solution, with B<sub>4</sub>C volume fraction increasing from 0 to 30 vol. %,  $j_{\text{corr}}$  moves to higher values. In H<sub>3</sub>BO<sub>3</sub> solution,  $j_{\text{corr}}$  augments from 0.10 to 0.35  $\mu\text{A}\cdot\text{cm}^{-2}$ . While it increases by almost 5 times in K<sub>2</sub>SO<sub>4</sub> solution, and by more than 30 times in NaCl solution. This result indicates that increasing B<sub>4</sub>C volume fraction leads to decrease in the corrosion resistance of composites.

Figures 4.5a and 4.5b compare the surface morphology of AA1100-16 vol. % B<sub>4</sub>C before and after polarization in NaCl solution. As clearly evidenced in Figures 4.5b, pitting occurs and preferentially initiates at Al/B<sub>4</sub>C interfaces. Interestingly, for the base alloy, pitting was also observed and it was found to develop at the Al/Fe intermetallic interfaces, as shown in Figure 4.6. For sulphate and boric acid solutions, the highest current density recorded during the potentiodynamic scan is less than 50  $\mu\text{A}\cdot\text{cm}^{-2}$ , which suggests that pitting does not occur during polarization (even polarized up to + 1000 mV vs. Ag/AgCl). This result is in line with microscopic observations that no pit is present on the surface.

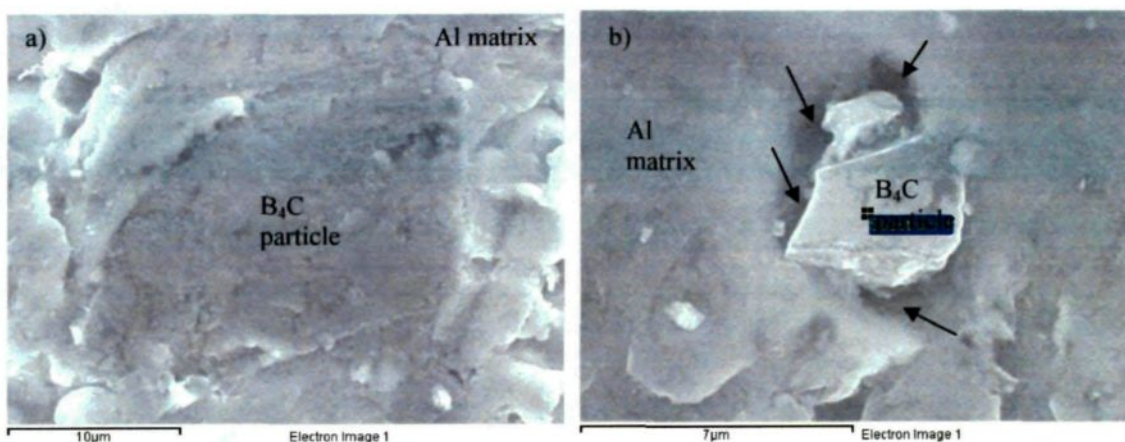


Figure 4.5 SEM image presenting the surface morphology of AA1100-16 vol. % B<sub>4</sub>C (a) before and (b) after polarization in 3.5% NaCl. Initiation of pitting (marked as black arrows) is observed at the Al/B<sub>4</sub>C interfaces after being polarized to 1 mA.cm<sup>-2</sup>.

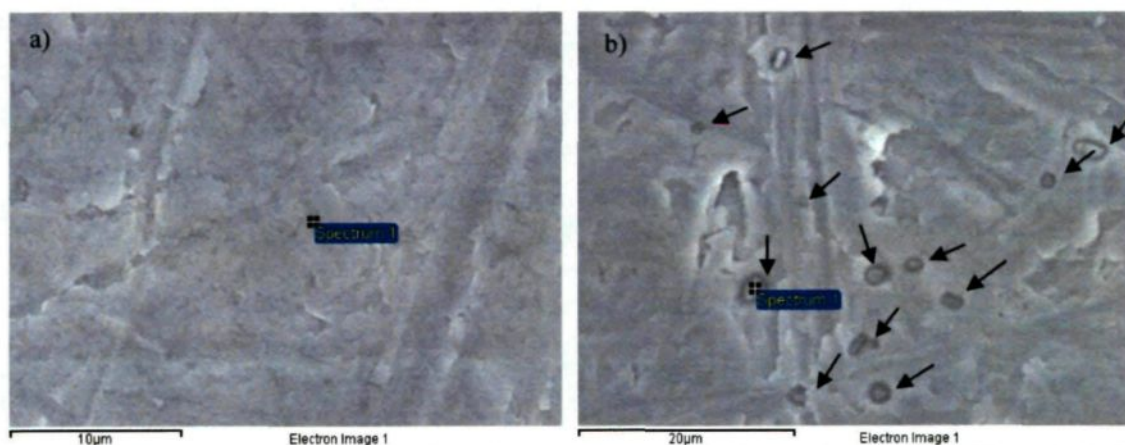


Figure 4.6 SEM image presenting the surface morphology of AA1100 alloy (a) before and (b) after polarization in 3.5% NaCl. Initiation of pitting (marked as black arrows) at Al/intermetallic phase is observed after polarization. EDS result shows that the intermetallic is Fe-containing phases.

### 4.3.2 Electrochemical Impedance Spectroscopy

Impedance spectroscopy is another effective electrochemical method to study the effect of B<sub>4</sub>C particles on the corrosion behavior of the base alloy. In contrast to polarization techniques, impedance measurements only require the application of a small AC perturbation to the investigated MMCs, which has little or no effect on the integrity of

materials. Therefore, it can virtually be considered as a non-destructive investigation method.

Figures 4.7, 4.8, and 4.9 show the typical Bode plots of three materials in 2500 ppm boron-containing  $\text{H}_3\text{BO}_3$ , 0.5 M  $\text{K}_2\text{SO}_4$  and 3.5% NaCl solutions, respectively. As semi-quantitative criterion to determine whether a material is corrosion resistant or not, the average impedance module measured at low frequencies was used. Indeed, as the frequency acquisition is lowered, a resistive behavior is generally encountered, thereby approaching the value of polarization resistance associated to faradaic charge transfers assigned to corrosion processes. As could be seen in figures above mentioned, in all three solutions, the impedance at low frequency decreases with increasing  $\text{B}_4\text{C}$  particles content, again suggesting that incorporation of  $\text{B}_4\text{C}$  particles to the base alloy decreases its corrosion resistance. The average impedance values in the range of 0.01 ~ 0.04 Hz ( $Z_{0.01-0.04 \text{ Hz}}$ ) are summarized in Figure 4.10. From this figure, it is observed that for the same material, impedance in  $\text{H}_3\text{BO}_3$  solution always shows the highest values while the impedances recorded in NaCl solution are lowest. As an example, for AA1100-30 vol. %  $\text{B}_4\text{C}$  MMC, an average  $Z_{0.01-0.04 \text{ Hz}}$  of 156 k $\Omega$  is measured in  $\text{H}_3\text{BO}_3$  solution, while the same parameter has a value of 1.32 k $\Omega$  in NaCl solution.

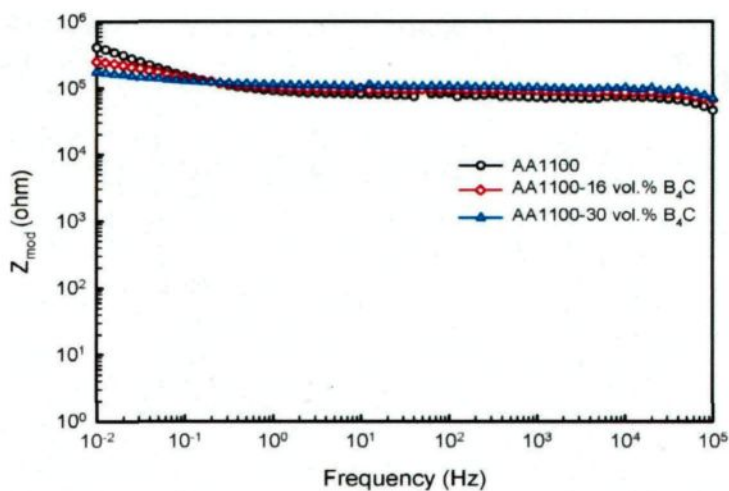


Figure 4.7 Typical Bode plots of AA1100, -16 vol. %  $B_4C$  and -30 vol. %  $B_4C$  composites obtained after a 3-hour immersion in 2500 ppm B-containing  $H_3BO_3$  solution.

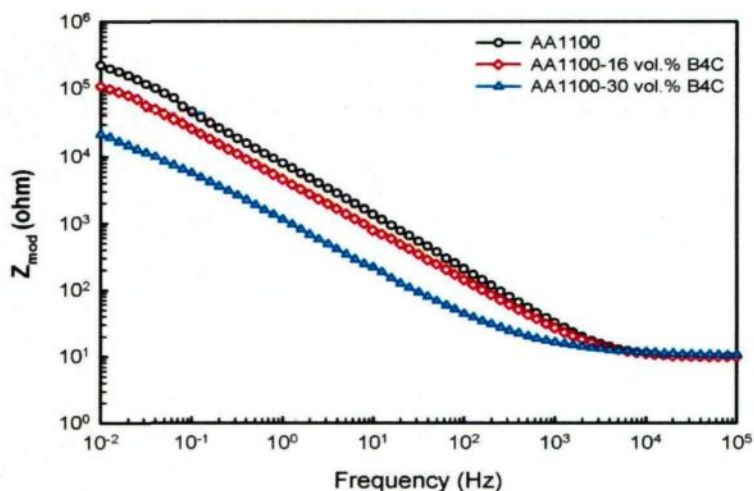


Figure 4.8 Typical Bode plots of AA1100, -16 vol. %  $B_4C$  and -30 vol. %  $B_4C$  composites obtained after a 1-hour immersion in 0.5 M  $K_2SO_4$  solution.

Electrochemical impedance spectroscopy was also used to determine the pitting corrosion susceptibility of materials immersed in investigated solutions. As seen from Figure 4.9 (3.5% NaCl solution), when the acquisition frequency is lowered from 0.1 to 0.01 Hz, the impedance of the two composites is found to decrease (inductive phenomenon). Also, in this frequency interval, some instability is observed in the electrical signal recorded at the working electrode surface. Such features are indicators of the occurrence of

pitting for the two composites. This result is in accordance with polarization curves which show that Al-B<sub>4</sub>C MMCs exhibit the highest susceptibility to pitting corrosion in NaCl solution. For the base alloy, there is no inductive phenomenon recorded, indicating that its resistance to pitting is higher than that of MMCs. Again, the result is in agreement with polarization results presented above.

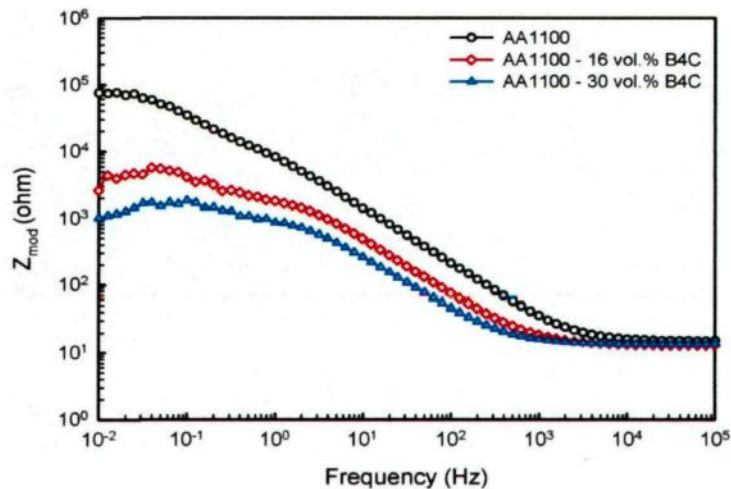


Figure 4.9 Typical Bode plots of AA1100, AA1100-16 vol. % B<sub>4</sub>C and AA1100-30 vol. % B<sub>4</sub>C obtained after a 1-hour immersion in 3.5% NaCl solution.

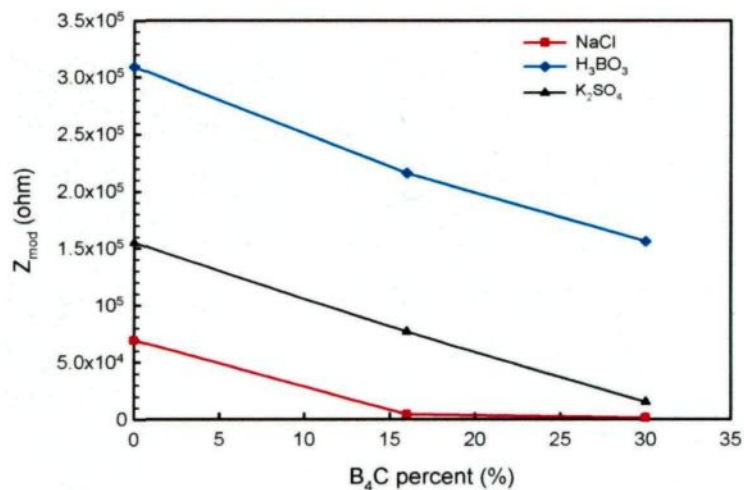


Figure 4.10 Average impedances measured in three solutions in the frequency range 0.01 ~ 0.04 Hz as a function of B<sub>4</sub>C percent in the MMCs.

Damage function ( $D$ ) is a useful indicator that evidences the influence of a parameter on the corrosion susceptibility of a material. It is typically characterized as the changes of impedance in the low frequency region as a function of immersion time.<sup>[27]</sup> In the present study, it has been adapted to visually report modifications of impedance obtained in the low frequency region (0.01 - 0.04 Hz), along with  $B_4C$  percent variation in the composite. Thus, in the present study, the indicator  $D$  is defined as:

$$D = \log (Z_{AA1100}/Z_{\%B_4C})_{0.01-0.04Hz}$$

where  $Z_{AA1100}$  is the average impedance of the alloy AA1100 in 2500 ppm boron-containing  $H_3BO_3$  in the frequency range of 0.01-0.04 Hz. As a reference, the damage function of AA1100 in  $H_3BO_3$  solution equals to zero.  $Z_{\%B_4C}$  represents the average impedance of composites with different  $B_4C$  volume percent (*i.e.* 16 vol. %  $B_4C$  and 30 vol. %  $B_4C$ ) in the 0.01 to 0.04 Hz frequency range.

Figure 4.11 summarizes the damage functions calculated as a function of  $B_4C$  volume fraction in 2500 ppm boron-containing  $H_3BO_3$ , 0.5 M  $K_2SO_4$  and 3.5% NaCl solutions. It is observed that for the same material, regardless of the base alloy or the composite, the minimum damage function was obtained when the material was immersed in 2500 ppm boron-containing  $H_3BO_3$  solution, while the greatest damage function was in 3.5 % NaCl. This result demonstrates again that all materials investigated are more corrosion resistant in 2500 ppm boron-containing  $H_3BO_3$  than that in 0.5 M  $K_2SO_4$  and 3.5% NaCl. Take the composites with 16 vol. %  $B_4C$  as an example, the damage function value in  $H_3BO_3$  solution is 0.16, while it is 0.60 in  $K_2SO_4$  and is as high as 1.8 in NaCl.

Additionally, it is also found that in all three solutions, the damage function increases considerably with increasing B<sub>4</sub>C volume fraction from 0 % to 30 %. Thus the highest damage function value, which is  $D = 2.40$ , is obtained from AA1100-30 vol. % B<sub>4</sub>C while immersed in 3.5% NaCl.

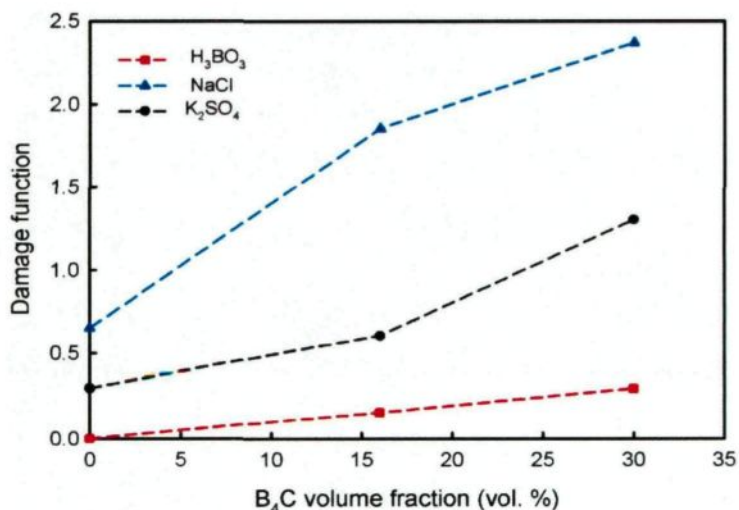


Figure 4.11 Damage function as function of B<sub>4</sub>C percent for materials investigated in 2500 ppm B-containing H<sub>3</sub>BO<sub>3</sub>, 0.5 M K<sub>2</sub>SO<sub>4</sub> and 3.5% NaCl solutions.

#### 4.4 Conclusions

The corrosion behaviour of Al-B<sub>4</sub>C metal matrix composites in 2500 ppm boron-containing H<sub>3</sub>BO<sub>3</sub> solution was investigated in comparison with the corrosion behaviour in 0.5 M K<sub>2</sub>SO<sub>4</sub> and 3.5% NaCl solutions. Both polarization and electrochemical impedance techniques reveal the facts that all materials investigated are more corrosion resistant in 2500 ppm boron-containing H<sub>3</sub>BO<sub>3</sub> than that in other two solutions, and increasing the volume fraction of B<sub>4</sub>C particles to the composite leads to a decrease in its corrosion resistance. No appreciable corrosion was observed in boric acid and sulfate solutions, while apparent pitting was observed in NaCl solutions for all materials studied. The preferential

pitting sites were the Al/Fe intermetallics interfaces for the base alloy and the Al/B<sub>4</sub>C interfaces for the composites. Besides, it is observed that increasing the volume fraction of B<sub>4</sub>C particles in the composite decreases its corrosion resistance of Al-B<sub>4</sub>C composites.

## References

- [1] X.-G. Chen, "Application of Al-B<sub>4</sub>C Metal Matrix Composites in the Nuclear Industry for Neutron Absorber Materials", in: *Proceedings of the Symposium on Solidification Processing of Metal Matrix Composites*, W.H. Hunt and N. Grupta (Eds.), TMS, 2006, pp. 343-350.
- [2] X.-G. Chen, R. Hark, "Development of Al-30%B<sub>4</sub>C Metal Matrix Composites for Neutron Absorber Material", in: *Proceedings of Aluminium Alloys: Fabrication, Characterization and Applications* W. Yin and S.K. Das (Eds.), TMS, 2008, pp. 3-9.
- [3] G. Bonnet, V. Rohr, X.-G. Chen, J.L. Bernier, R. Chiocca, H. Issard, "Use of Alcan's Al-B<sub>4</sub>C Metal Matrix Composites as Neutron Absorber Material in TN International's Transportation and Storage Casks", *Packaging, Transport, Storage and Security of Radioactive Material*, 20 (2009) 98-102.
- [4] A.R. Kennedy, "The Microstructure and Mechanical Properties of Al-Si-B<sub>4</sub>C Metal Matrix Composites", *Journal of Materials Science*, 37 (2002) 317-323.
- [5] L.H. Hihara, R.M. Latanision, "Corrosion of Metal Matrix Composites", *International Materials Review*, 39 (1994) 245-263.
- [6] M.S.N. Bhat, M.K. Surappa, H.V.S. Nayak, "Corrosion Behaviour of Silicon Carbide Particle Reinforced 6061/Al Alloy Composites", *Journal of Materials Science*, 26 (1991) 4991-4996.
- [7] H. Sun, E.Y. Koo, H.G. Wheat, "Corrosion Behavior of SiCp/6061 Al Metal Matrix Composites", *Corrosion*, 47 (1991) 741-753.
- [8] I.B. Singh, D.P. Mandal, M. Singh, S. Das, "Influence of SiC Particles Addition on the Corrosion Behavior of 2014 Al-Cu Alloy in 3.5% NaCl Solution", *Corrosion Science*, 51 (2009) 234-241.
- [9] H. Ding, L. Hihara, "Localized Corrosion Currents and pH Profile Over B<sub>4</sub>C, SiC, and Al<sub>2</sub>O<sub>3</sub> Reinforced 6092 Aluminum Composites: I. In 0.5 M Na<sub>2</sub>SO<sub>4</sub> Solution", *Journal of the Electrochemical Society*, 152 (2005) B161-B167.
- [10] H. Ding, L. Hihara, "Electrochemical Behavior of Boron Carbide and Galvanic Corrosion of Boron Carbide Reinforced 6092 Aluminum Composites", *ECS Transactions*, 1 (2006) 103-114.

- [11] R. Emmerich, W. Ensinger, B. Enders, "Corrosion Behaviour of Borated Aluminium Used as a Neutron Absorber", *Journal of European Archaeology*, 16 (2005) 151-156.
- [12] B. Dikici, M. Gavgali, C. Tekmen, "Corrosion Behaviour of an Artificially Aged (T6) Al-Si-Mg-based Metal Matrix composite", *Journal of Composite Materials*, 40 (2006) 1259-1269.
- [13] I. Gurrappa, V.V.B. Prasad, "Corrosion Characteristics of Aluminum Based Metal Matrix Composites", *Materials Science and Technology*, 22 (2006) 115-122.
- [14] C.L. He, F.Q. Li, C.S. Liu, Z.M. Shi, M.J. Zhao, J. Bi, Q.K. Cai, "Study of Corrosion Resistance of Anodized Film on the SiCp/2024 Al Metal Matrix Composite with Electrochemical Impedance Spectroscopy", *Acta Metallurgica Sinica*, 37 (2001) 869-872.
- [15] Y.L. Cheng, Z.H. Chen, H.L. Wu, H.M. Wang, "The Corrosion Behaviour of the Aluminum Alloy 7075/SiCp Metal Matrix Composite Prepared by Spray Deposition", *Materials and Corrosion*, 58 (2007) 280-284.
- [16] Z. Ahmad, B.J. Abdul Aleem, "Degradation of Aluminum Metal Matrix Composites in Salt Water and its Control", *Materials & Design*, 23 (2002) 173-180.
- [17] A. Pardo, M.C. Merino, F. Viejo, S.J. Feliu, M. Carboneras, R. Arrabal, "Corrosion Behavior of Cast Aluminum Matrix Composites (A3xx.x/SiCp) in Chloride Media", *Journal of the Electrochemical Society*, 152 (2005) B198-B204.
- [18] G.M. Pinto, J. Nayak, A.N. Shetty, "Corrosion Behaviour of 6061 Al-15 vol. Pct. SiC Composite and its Base Alloy in a Mixture of 1:1 Hydrochloric and Sulphuric Acid Medium", *International Journal of Electrochemical Science*, 4 (2009) 1452-1468.
- [19] A. Pardo, M.C. Merino, S. Merino, M.D. Lopez, F. Viejo, M. Carboneras, "Influence of SiCp Content and Matrix Composition on Corrosion Resistance in Cast Aluminum Matrix Composites in Salt Fog", *Corrosion Engineering, Science and Technology*, 39 (2004) 82-88.
- [20] F. Zucchi, G. Trabanelli, V. Grassi, A. Frignani, "Corrosion Behavior in Sodium Sulfate and Sodium Chloride Solutions of SiCp Reinforced Magnesium Alloy Metal Matrix Composites", *Corrosion*, 60 (2004) 362-368.
- [21] J. Hu, R.S. Luo, C.K. Yao, L.C. Zhao, "Effect of Annealing Treatment on the Stress Corrosion Cracking Behavior of SiC Whisker Reinforced Aluminum Composite", *Materials Chemistry and Physics*, 70 (2001) 160-163.
- [22] M. Montoya-Dávila, M.I. Pech-Canul, M.A. Pech-Canul, "Corrosion Performance of Al/SiCp Composites with Multimodal Distribution under Humid Ambient and Aerated Chloride Solutions", in: *Supplemental Proceedings: General Paper Selections*, (Eds.), 2009, pp. 91-99.

- [23] J. Hu , L.X. Xu, C.K. Yao, "Location Corrosion of Alumina Borate Whisker Reinforced AA2024 T6 Composite in Aqueous 3.5% NaCl Solution", *Materials Chemistry and Physics*, 76 (2002) 290-294.
- [24] J. Datta, B. Samanta, A. Jana, S. Sinha, C. Bhattacharya, S. Bandyopadhyay, "Role of  $\text{Cl}^-$  and  $\text{NO}_3^-$  Ions on the Corrosion Behavior of 20%  $\text{SiC}_p$  Reinforced 6061-Al Metal Matrix Composite: A Correlation between Electrochemical Studies and Atomic Force Microscopy", *Corrosion Science and Protection Technology*, 50 (2008) 2658-2668.
- [25] J. Zhu, L.H. Hihara, "Corrosion of Continuous Alumina-Fibre Reinforced Al-2 wt.% Cu-T6 Metal-Matrix Composite in 3.15 wt.% NaCl Solution", *Corrosion Science and Protection Technology*, 52 (2010) 406-415.
- [26] L. Bertolini, M.F. Brunella, S. Candiani, "Corrosion Behavior of a Particulate Metal-Matrix Composite", *Corrosion*, 55 (1999) 422-431.
- [27] F. Mansfeld, M.W. Kending, "Evaluation of Anodized Aluminum Surfaces with Electrochemical Impedance Spectroscopy", *Journal of the Electrochemical Society*, 135 (1988) 828-833.

## **CHAPTER 5**

# **INVESTIGATION ON CORROSION BEHAVIOR OF THE Al-B<sub>4</sub>C METAL MATRIX COMPOSITES IN A MILDLY OXIDIZING AQUEOUS ENVIRONMENT**

## CHAPTER 5

### INVESTIGATION ON CORROSION BEHAVIOR OF THE Al-B<sub>4</sub>C METAL MATRIX COMPOSITES IN A MILDLY OXIDIZING AQUEOUS ENVIRONMENT

#### Abstract

The corrosion behavior of Al-B<sub>4</sub>C metal matrix composites in a 0.5 M K<sub>2</sub>SO<sub>4</sub> solution was investigated using electrochemical impedance spectroscopy and potentiodynamic polarization methods. Optical and scanning electron microscopes as well as profilometry were employed to study the surface morphology of the material before and after corrosion. Moreover, infrared reflection-absorption spectroscopy (IRRAS) and x-ray photoelectron spectroscopy (XPS) were used to identify the corrosion products. It was observed that SO<sub>4</sub><sup>2-</sup> species did not induce pitting of the AA1100-16 vol. % B<sub>4</sub>C. In contrast, it was found that the Al-B<sub>4</sub>C composite was highly susceptible to pitting attacks by chloride ions, especially at the Al/B<sub>4</sub>C interfaces. The B<sub>4</sub>C particles showed a cathodic character with respect to the peripheral matrix, and both the IRRAS and XPS results showed that bayerite Al(OH)<sub>3</sub> was the main corrosion product.

## 5.1 Introduction

Al-B<sub>4</sub>C metal matrix composites (MMCs) are being considered as new advanced materials due to their light weight, superior thermal conductivity, high stiffness and hardness. <sup>[1]</sup> Due to the neutron capturing ability, Al-B<sub>4</sub>C composites have recently been extensively used as neutron absorber components in the nuclear industry. <sup>[2-5]</sup> However, although the incorporation of the particles into the Al matrix can enhance the physical and mechanical properties of the base material, it may also change its corrosion behavior. <sup>[6]</sup> Bhat *et al.* <sup>[7]</sup> investigated the corrosion behavior of the 6061 Al-SiCp composite and its base alloy in seawater using the potentiodynamic polarization technique. It was found that the composite corroded faster than its base alloy and that composite corrosion was mainly confined to the interface as opposed to the uniform corrosion observed for the base alloy. Sun *et al.* <sup>[8]</sup> also studied the corrosion behavior of 6061 Al-SiCp MMCs in a NaCl solution. With the observation that the pitting degree rose with an increasing SiC content, it is presumed that the pitting corrosion depends on the local SiC distribution and the surface film integrity. According to the authors, larger volume percentages of SiC could result in more opportunities for film disruption formation and consequently more pit initiation sites. Singh *et al.* <sup>[9]</sup> similarly studied the influence of SiC additions on the corrosion behavior of 2014 alloy in a 3.5% NaCl solution at 30 °C. It was revealed that the addition of 10 wt. % SiC into the base alloy increases its corrosion resistance considerably, while the addition of 25 wt. % SiC into the base alloy decreases the overall corrosion resistance of the material. From a more general perspective, Roepstorff *et al.* <sup>[10]</sup> reported that the corrosion resistance of metal matrix composites can essentially be affected by three processes: (1) galvanic

coupling of the metal and reinforcement, (2) crevice attack at the metal/reinforcement interface, and (3) preferred localized attack on possible reaction products between metal and ceramic. According to Hihara *et al.*,<sup>[11]</sup> among these corrosion mechanisms, the galvanic corrosion between aluminum and reinforcement particles is of primary concern when studying MMC corrosion behavior.

In contrast to the considerable amount of research work dedicated to a better understanding of the corrosion behavior of Al-SiC composites, there are only a few studies devoted to the corrosion behavior of Al-B<sub>4</sub>C composites. Ding and Hihara<sup>[12]</sup> investigated the effect of B<sub>4</sub>C particles on the corrosion behavior of 6092-T6 Al MMCs with 20 vol. % B<sub>4</sub>C in a 0.5 M Na<sub>2</sub>SO<sub>4</sub> solution at room temperature. It was found that corrosion initiation and propagation are related to the formation of microcrevices caused by reinforcement particles left in relief, to localized acidification and alkalization of the solution, and to aluminum containing amphoteric oxides. In a recent study, Emmerich *et al.*<sup>[13]</sup> performed electrochemical polarization measurements on pure aluminum and 4.0 - 4.5 at. % borated AA1100 in the as-received surface condition in two different electrolytes at 90 °C. The first solution contained 0.15 mg/L fluoride and 0.15 mg/L chloride, while the second contained the same quantity of fluoride but a higher chloride ion concentration (*i.e.*, 1.0 mg/L). The applied potential was increased from -300 mV to +400 mV during a potentiodynamic polarization experiment. For borated aluminum, current transients (*i.e.*, metastable depassivation events) were observed and attributed to locally thinner and/or less stable passivation layers on the surface. The cause for such inhomogeneous passive layers could

be mechanical surface defects or inclusions in the alloy. It was also presumed that both  $\text{AlB}_2$  and  $\text{AlB}_{12}$  particles present in the alloy could act as nucleation sites.

The AA1100 matrix is very attractive for neutron absorption applications as it can incorporate high concentrations of  $\text{B}_4\text{C}$  particles and still have good formability for the extrusion and rolling manufacturing processes. <sup>[1] [14]</sup> As a neutron absorber used in wet storage applications, AA1100- $\text{B}_4\text{C}$  MMCs are exposed to aqueous environments considered, *prima facie*, as being mildly corrosive. <sup>[15]</sup> During this immersion period, because material degradation by corrosion may occur, it becomes an evident and important safety precaution to better understand the corrosion behavior of AA1100- $\text{B}_4\text{C}$  MMCs. In literatures concerning the corrosion of MMCs, the mildly corrosive 0.5 M  $\text{K}_2\text{SO}_4$  solution is commonly used when studying the composites corrosion behavior. <sup>[16, 17]</sup> The present research aims at studying the corrosion behavior of AA1100 with 16 vol. %  $\text{B}_4\text{C}$  reinforcement in a 0.5 M  $\text{K}_2\text{SO}_4$  solution using electrochemical impedance spectroscopy (EIS), potentiodynamic polarization and surface science techniques. In order to determine the aggressiveness of sulfate ions toward the MMCs, the influence of chloride species acting as corrosion agents on this material is also briefly reported.

## **5.2 Experimental Procedure**

### **5.2.1 Material Preparation**

The metal matrix composite AA1100-16 vol. %  $\text{B}_4\text{C}$  fabricated by Rio Tinto Alcan (Saguenay, Quebec, Canada) was used in the present study. The chemical composition of the base alloy is listed in Table 5.1. The composites were produced using the liquid metal

mixing technique. During the mixing process, ~ 0.5-1.5 wt. % titanium was added to the molten aluminum to reduce the interfacial reactions and ensure a uniform distribution of B<sub>4</sub>C particles in the matrix.<sup>[18]</sup> For the corrosion experiment, rolled flat plates of approximately 4.3 mm thick were used. The plates were cut into small 15 × 15 mm pieces. All the samples were mounted in epoxy resin with only one air-exposed surface, then grounded and polished to a 0.05 μm fine finish. The polished samples were cleaned with soapy water, rinsed with deionized water, and dried with clean compressed air. Finally, the as-processed coupons were desiccated before carrying out the corrosion measurements.

Table 5.1 Typical chemical composition of AA 1100 – 15 wt. % B<sub>4</sub>C composite.

| Elements         | Amounts (wt. %) |
|------------------|-----------------|
| Ti               | 0.5-1.5         |
| B <sub>4</sub> C | 15              |
| AA1100           | Balance         |

### 5.2.2 Electrochemical Experiments

Electrochemical experiments were performed at ambient conditions (21°C) in solutions of 0.5 M K<sub>2</sub>SO<sub>4</sub> (pH = 9.5) and 3.5% NaCl (pH = 5.9) both opened to air. The potentiostat employed in the present study was a Reference 600 instrument (Gamry Instruments, Warminster, PA, USA). Electrochemical investigations were performed using a 300 cm<sup>3</sup> - EG&G PAR flat cell (London Scientific, London, ON, Canada), equipped with a standard three-electrode system with a saturated calomel electrode (SCE) as the reference electrode, a platinum mesh as the counter electrode (CE), and the sample as the working electrode (WE). The corrosion cell had a 1 cm<sup>2</sup> orifice as the working surface. The SCE

was connected to the cell by a Luggin capillary, the tip of which was very close to the surface of the working electrode in order to minimize the IR drop. All potentials given in this article are referred to the SCE electrode. Prior to electrochemical measurements, the samples were immersed in the solution for approximately three hours until a steady open circuit potential ( $E_{ocp}$ ) was reached. Magnetic stirring was employed at the cell bottom to increase mass transfer at the electrode surface.

Potentiodynamic polarization tests were performed at a scan rate of  $1 \text{ mV s}^{-1}$  with the scans being taken from  $-250 \text{ mV}$  below  $E_{ocp}$  to  $1000 \text{ mV vs. SCE}$ . The EIS curves were obtained by applying a sinusoidal potential of  $10 \text{ mV}$  in amplitude around  $E_{ocp}$  at a steady-state in the  $100 \text{ kHz}$  to  $10 \text{ mHz}$  frequency range. Frequencies lower than  $10 \text{ mHz}$  were not used as the data acquisition time of the frequency response analysis (FRA) was very long resulting in significant dispersion of impedance values. In all cases, the tests were duplicated to ensure reproducibility of the results. Using the Gamry Instruments Echem Analyst software, the impedance parameters were calculated by fitting the experimental results to an equivalent circuit model.

Since the working electrode showed deviation from the ideal capacitive behavior due to surface roughness, heterogeneities, anion adsorption, non-uniform potential, current profile, *etc.*,<sup>[19]</sup> the constant phase element (CPE) was employed to substitute pure capacitances in the equivalent circuits employed. Zoltowski<sup>[20]</sup> gave the CPE impedance as:

$$Z_{CPE} = \frac{1}{Q_a(j\omega)^\alpha}$$

where  $j = \sqrt{-1}$  and  $\omega$  was the angular frequency ( $\omega = 2\pi f$ ,  $f$  being the frequency).

The double layer capacitance quantity (proportional to the active area) was  $Q_a$ , and  $\alpha$  was the CPE power with  $-1 \leq \alpha \leq 1$ . When  $\alpha = 1$ , the CPE represented a pure capacitance; when  $\alpha = 0$ , the CPE was considered as a pure resistance; and when  $\alpha = -1$ , the CPE was regarded as a pure inductance. In this case, the CPE became an extremely flexible fitting parameter, but its physical significance and relationship with the distribution of time constants was not clear. [21]

### 5.2.3 Microstructural Analysis

An optical microscope (CLEMEX JS-2000) and a scanning electron microscope equipped with an energy dispersive spectrometer (EDS) (Hitachi SU-70) were used to characterize the microstructure before and after the corrosion tests. To investigate the topographic profile of the composite surface before and after corrosion, a STIL confocal profilometer (CHR150-L) equipped with an optical pen MG140 was employed.

### 5.2.4 Infrared Reflection-Absorption Spectroscopy

The presence of typical vibration bands, associated with known aluminum corrosion products, enabled the use of the infrared reflection-absorption spectroscopy (IRRAS) as a complementary tool to examine the corrosion products studied herein. The IRRAS operated using a Nicolet 6700 spectrometer (ThermoFisher Scientific) equipped with a Mid-IR MCT-B wide band  $N_2$ -cooled detector and a XT-KBr beam splitter. The Smart SAGA (Specular Apertured Grazing Angle) accessory was used to analyze samples at an average

incidence angle of  $80^\circ$  relative to the normal surface. The spectra were recorded from 4000 to  $600\text{ cm}^{-1}$  with a resolution of  $4\text{ cm}^{-1}$  and 64 scans. The IR radiation was p-polarized, and the resulting spectrum was subtracted from a background spectrum taken from a clean gold-coated reference sample. All the IRRAS spectra results were processed using the OMNIC software provided by the instrument manufacturer.

### 5.2.5 X-Ray Photoelectron Spectroscopy

The X-ray photoelectron spectra (XPS) were recorded with a model AXIS\_ULTRA Kratos photoelectron spectrometer, using a monochromatic Al K- $\alpha$  radiation (1486.6 eV), in a UHV system, and kept at about  $10^{-8}$  mbar during the analysis. The anode voltage was 15 kV and the emission current 20 mA. For each sample, high resolution scans for C1s, Al2p, O1s, B1s and Ti2p were recorded with a 0.5 eV resolution then followed by a high sensitivity survey scan recorded at a 1.8 eV resolution.

## 5.3 Results and Discussion

### 5.3.1 Potentiodynamic Polarization of Al-B<sub>4</sub>C MMC in K<sub>2</sub>SO<sub>4</sub> and NaCl Solutions

Figure 5.1 and Figure 5.2 show the typical potentiodynamic polarization curve of AA1100-16 vol. % B<sub>4</sub>C MMC in 0.5 M K<sub>2</sub>SO<sub>4</sub> and 3.5 % NaCl solutions, respectively. Corrosion current density  $j_{\text{corr}}$  and corrosion potential  $E_{\text{corr}}$ , both derived from the polarization curves, are summarized in Table 5.2. The corrosion current density  $j_{\text{corr}}$  was calculated from the extrapolation of the cathodic curves, as shown in the inset in Figure 5.1

and Figure 5.2. From Figure 5.1, it was observed that the anodic branch of the polarization curve exhibited the three following regions:

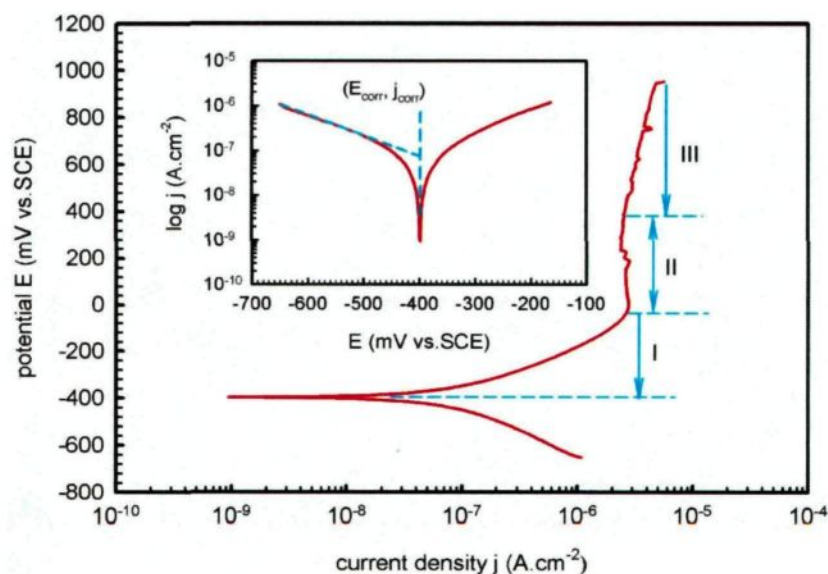


Figure 5.1 Typical potentiodynamic polarization curve of AA1100-16 vol. % B<sub>4</sub>C composite in a 0.5 M K<sub>2</sub>SO<sub>4</sub> solution after a 3-hour immersion period. (Inset: Tafel plot showing the corrosion current  $j$  was obtained at the intercept of the extrapolation of cathodic branch.  $j_{\text{corr}} = 74 \text{ nA}\cdot\text{cm}^{-2}$ ,  $E_{\text{corr}} = -400.7 \text{ mV}$ ).

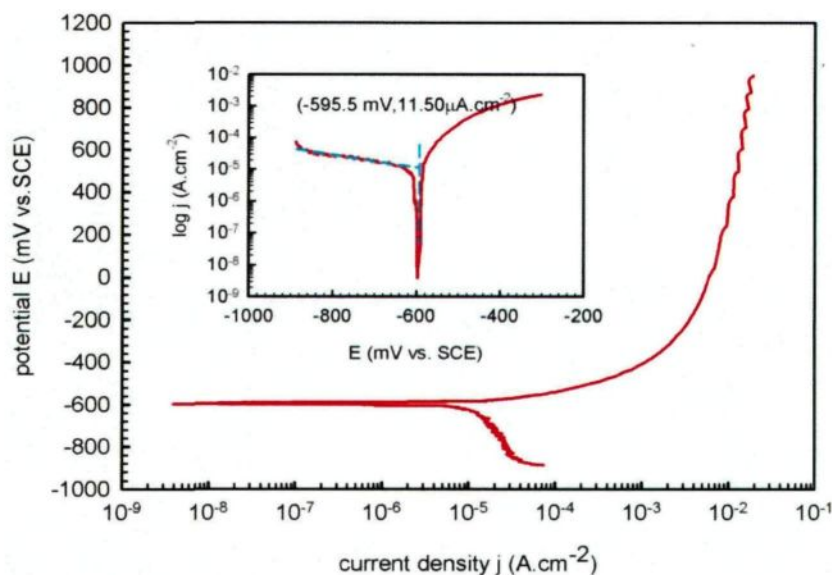


Figure 5.2 Typical potentiodynamic polarization curve of AA1100-16 vol. % B<sub>4</sub>C composite in a 3.5% NaCl solution after a 3-hour immersion period. (Inset: Tafel plot showing the corrosion current  $j_{\text{corr}}$  was obtained at the intercept of the extrapolation of cathodic branch.  $j_{\text{corr}} = 11.50 \text{ }\mu\text{A}\cdot\text{cm}^{-2}$ ,  $E_{\text{corr}} = -595.5 \text{ mV}$ ).

*Region 'I'*: An active region characterized by a gradual increase in the current density with a forward potential scan, ascribing to a progressive oxidation of Al matrix;

*Region 'II'*: A passive region characterized by an almost constant current density as the applied potential increased;

*Region 'III'*: A slight increase in the dissolution kinetics.

Table 5.2 Corrosion parameters calculated from polarization curves.

| Parameters   | Solution                             |           |
|--|--------------------------------------|-----------|
|  | 0.5 M K <sub>2</sub> SO <sub>4</sub> | 3.5% NaCl |
| $E_{\text{corr}}$ (mV vs. SCE)                         | - 400.7                              | - 595     |
| $j_{\text{corr}}$ ( $\mu\text{A}\cdot\text{cm}^{-2}$ ) | 0.074                                | 11.5      |
| $R_p$ ( $\text{k}\Omega\cdot\text{cm}^2$ )             | 562                                  | 1.98      |

While the composite was immersed in a 3.5% NaCl solution (Figure 5.2), a passive region was not observed and the polarization curve remarkably shifted direction to a more negative  $E_{\text{corr}}$  and a higher current density. Both trends are associated with a more active material behavior. As compared in Figure 5.1, the  $E_{\text{corr}}$  in the sulfate solution is -400.7 mV and the  $j_{\text{corr}}$  value is as low as 74 nA.cm<sup>-2</sup>. During polarization in the K<sub>2</sub>SO<sub>4</sub> solution, the highest current density recorded was less than 10  $\mu\text{A}\cdot\text{cm}^{-2}$ , demonstrating that pitting of the MMC did not occur in this environment. Figure 5.3 compares the surface morphology of the composite before and after polarization in a K<sub>2</sub>SO<sub>4</sub> solution. It was observed that pitting was not provoked after polarization in a sulfate solution, while the protective TiB<sub>2</sub> layer around B<sub>4</sub>C particles dissolved.

Many researchers <sup>[22-24]</sup> studied the anodic dissolution of  $\text{TiB}_2$  in different conditions and found that  $\text{TiB}_2$  could be oxidized to  $\text{TiO}^{2+}$ ,  $\text{Ti}^{3+}$  and  $\text{TiO}_2 \cdot \text{H}_2\text{O}$  depending on the pH and aeration conditions. Compared to the corrosion behavior in a sulfate solution,  $E_{\text{corr}}$  decreased to -595 mV and  $j_{\text{corr}}$  increased to  $11.5 \mu\text{A} \cdot \text{cm}^{-2}$  while the composite was immersed in a 3.5% NaCl solution. Moreover, when the potential slightly exceeded  $E_{\text{corr}}$ , the current density increased steeply and rapidly reached  $1 \text{ mA} \cdot \text{cm}^{-2}$ . All these results indicate that the NaCl solution was more aggressive than the sulfate solution in provoking corrosion and that pitting occurred during polarization.

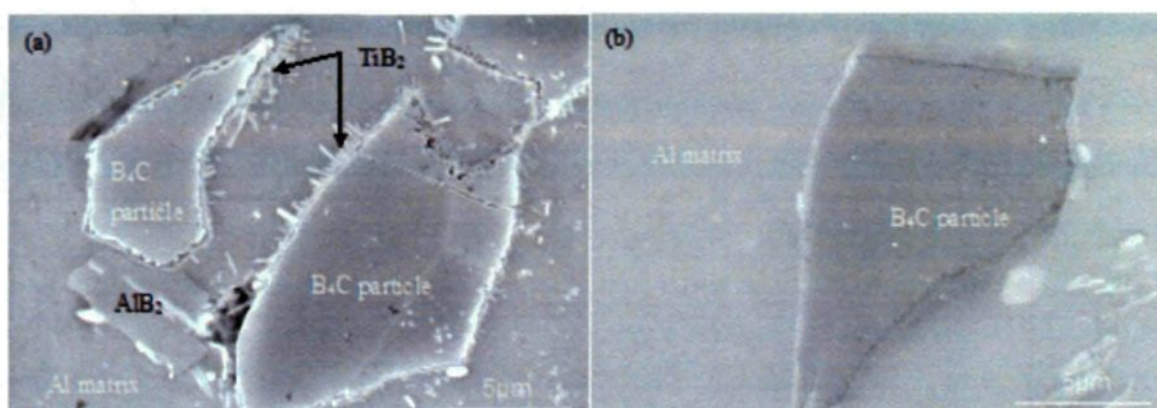


Figure 5.3 SEM image comparing the surface morphology of the composite (a) before and (b) after polarization in a 0.5 M  $\text{K}_2\text{SO}_4$  solution.

The SEM image presented in Figure 5.4 evidences pit initiations at the Al/ $\text{B}_4\text{C}$  interface. This can be explained by the fact that  $\text{B}_4\text{C}$  particles break the continuity of the neighboring aluminum oxide films. Such discontinuities would facilitate the passage of aggressive chloride ions to the matrix and, once in contact with the chloride ions, the matrix would suffer pitting. <sup>[25]</sup> Additionally, the protective  $\text{TiB}_2$  layers around the  $\text{B}_4\text{C}$  particles may deteriorate the discontinuity of the oxide film, and thus aggravate the pitting phenomenon. Finally, for both solutions, the polarization resistance ( $R_p$ ) values were

calculated from the slope of linear E - j curves found by varying  $\pm 10$  mV around the  $E_{corr}$ . As reported in Table 5.2, the polarization resistance in a 3.5 % NaCl solution is  $1.98 \text{ k}\Omega\cdot\text{cm}^2$ , which is low compared to that calculated in a 0.5 M  $\text{K}_2\text{SO}_4$  solution (*i.e.*,  $562 \text{ k}\Omega\cdot\text{cm}^2$ ).

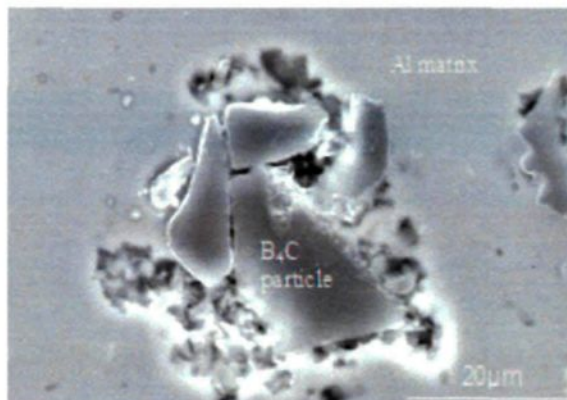


Figure 5.4 SEM image presenting the occurrence of pitting at the interface of Al/ $\text{B}_4\text{C}$  particles on an AA1100-16 vol. %  $\text{B}_4\text{C}$  MMC surface during polarization in a 3.5% NaCl solution.

Since the polarization results have demonstrated that  $\text{SO}_4^{2-}$  was really a mild oxidizing species for Al- $\text{B}_4\text{C}$  MMCs, electrochemical impedance spectroscopy was used to conduct a more thorough investigation of the Al- $\text{B}_4\text{C}$  MMCs corrosion behavior as a function of time in the sulfate environment.

### 5.3.2 Electrochemical Impedance Spectroscopy Investigation of Al- $\text{B}_4\text{C}$ MMC in 0.5 M $\text{K}_2\text{SO}_4$

Due to its sensitivity to material surface condition, the EIS technique was used to determine the corrosion behavior of AA1100-16 vol. %  $\text{B}_4\text{C}$  MMCs in a  $\text{K}_2\text{SO}_4$  solution as a function of time and surface state. The porosity caused by hydrogen precipitation and micro-shrinkage during the cooling and solidification of the molten composite was

observed on a few samples.<sup>[25]</sup> Figure 5.5a and Figure 5.5b respectively display optical images of typical uniform and defective surfaces. The profilometry analyses performed on these surfaces (Figure 5.5c and Figure 5.5d), revealed that the uniform surfaces were micro-flat while the pores in the defective surfaces were as deep as 55  $\mu\text{m}$ .

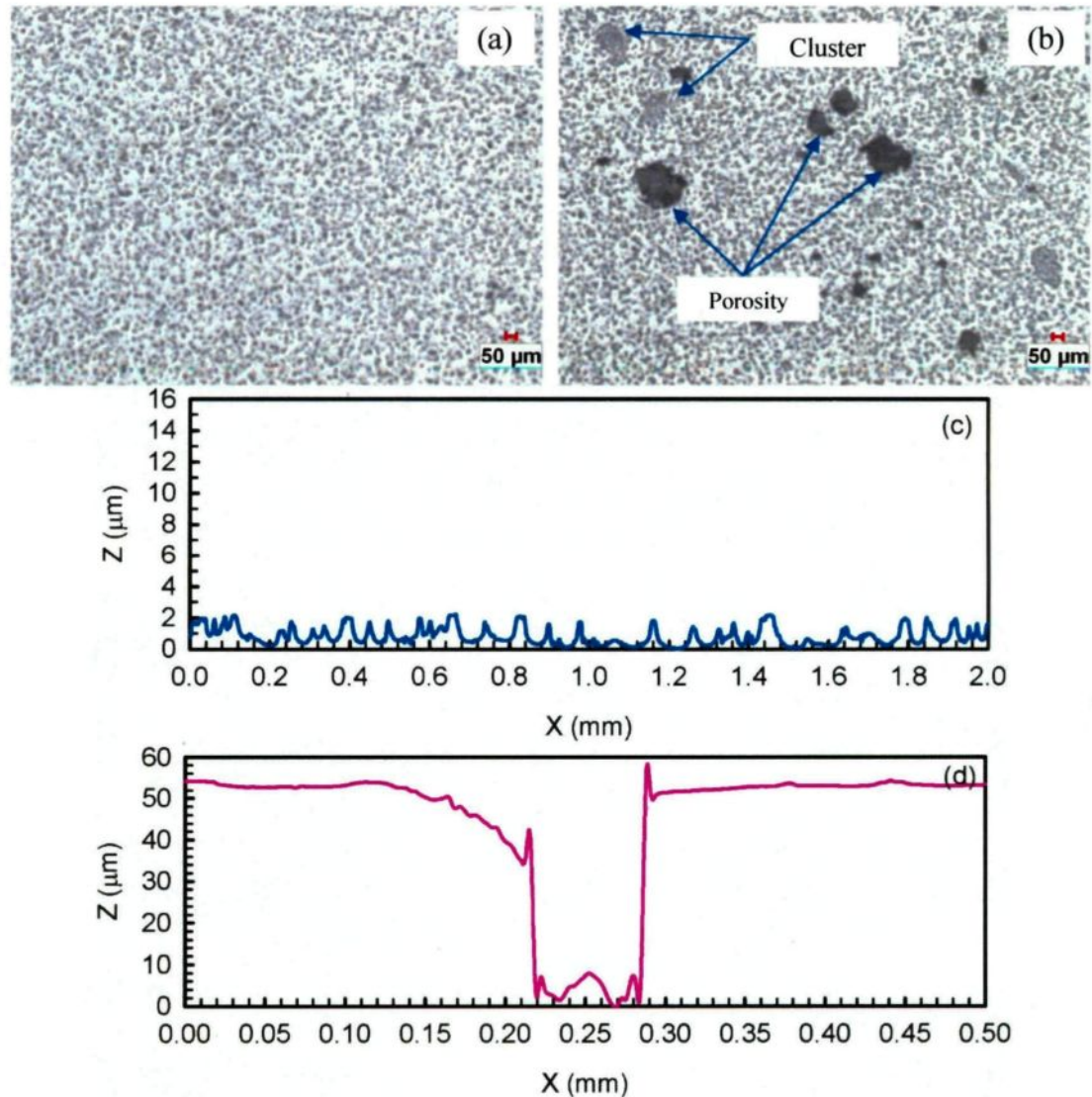


Figure 5.5 Optical micrographs showing (a) uniform B<sub>4</sub>C particle distribution and (b) defects on an AA1100-16 vol. % B<sub>4</sub>C MMC surface; topographic profile of (c) uniform surface and (d) defective surface.

Figure 5.6 shows typical Nyquist and Bode plots obtained from defect-free samples. The Nyquist plot shows a single semicircle and the Bode plot exhibits a one-time constant for the uniform surfaces. This behavior can be interpreted by the equivalent circuit shown in Figure 5.7. <sup>[26]</sup> It was observed that the polarization resistance parameter ( $R_p$ ) determined from the intercepts of the Nyquist plot with the  $Z_{\text{real}}$  axis was  $550 \text{ k}\Omega\cdot\text{cm}^2$ . This virtually equalled the resistance parameter obtained from the polarization curve *i.e.*,  $562 \text{ k}\Omega\cdot\text{cm}^2$ . Such a high  $R_p$  value was, on one hand, attributed to the high corrosion resistance of the material in the  $\text{K}_2\text{SO}_4$  solution. On the other hand, high impedance values were recorded since the  $\text{B}_4\text{C}$  particles took a certain fraction of the measured area and made the effective conductive area smaller than  $1 \text{ cm}^2$  (geometric area of the coupon exposed to the solution). All electrochemical parameters obtained from the equivalent circuit fit are listed in Table 5.3.

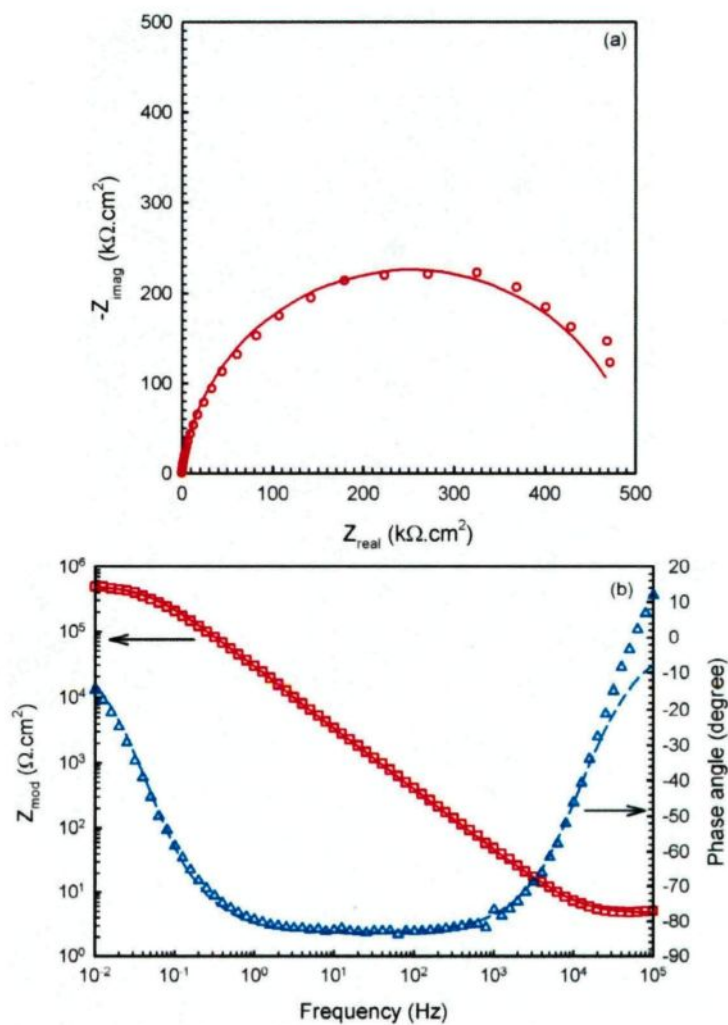


Figure 5.6 Typical (a) Nyquist and (b) Bode plots of AA1100-16 vol. % B<sub>4</sub>C MMC samples with uniform surfaces obtained after a 3-hour immersion period in a 0.5 M K<sub>2</sub>SO<sub>4</sub> solution (experimental data and fitted curves are respectively presented by points and lines).

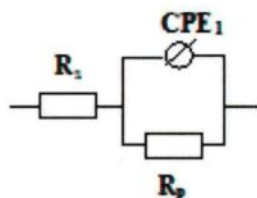


Figure 5.7 Equivalent circuit to interpret EIS spectra obtained from samples with uniform surface.

Table 5.3 Electrochemical parameters calculated from the equivalent circuit in Figure 5.7

| Corrosion parameters                                  | Values |
|---|--------|
| $R_s$ ( $\Omega \cdot \text{cm}^2$ )                  | 4.64   |
| $R_p$ ( $\text{k}\Omega \cdot \text{cm}^2$ )          | 550.0  |
| $\text{CPE}_1$ ( $\mu\text{F} \cdot \text{cm}^{-2}$ ) | 6.486  |
| $\alpha_1$  | 0.930  |

Figure 5.8 illustrates the typical Nyquist and Bode plots recorded for defective surfaces. The behavior of this system was characterized by high- and low-frequency capacitive loops. Consequently, the two time-constants were clearly exhibited in the Bode plot. The impedance magnitude of the defective surface at a low frequency (*i.e.*, 0.01 Hz) was 158  $\text{k}\Omega \cdot \text{cm}^2$ , hence much smaller than that of the defect-free surface (550  $\text{k}\Omega \cdot \text{cm}^2$ ). These results accord with the fact that defective surfaces were more susceptible to corrosion. Similar EIS spectra were obtained from electrodes coated with porous layers and interpreted in published literatures.<sup>[27, 28]</sup> Considering the real surface condition in the present study and in combination with models presented in published literatures, the EIS spectra in Figure 5.8 were interpreted with the equivalent circuit presented in Figure 5.9. All electrochemical parameters obtained from the equivalent circuit fit are listed in Table 5.4. The parallel combination of  $\text{CPE}_2$  and  $R_p$  corresponded to the double layer capacitance and polarization resistance at the solution/matrix interface found at the end of the pore. Taking into account that the concentration of different species involved in the reaction in the pore could differ from that of the bulk solution, the latter's resistance was marked as  $R_s$ , while the resistance associated to faradic processes occurring within the pore length was

noted as  $R_{po}$ . The capacitance of the composite within the pore length ( $CPE_1$ ) was in parallel with the capacitance within the pore ( $CPE_2$ ). The good fit presented in Figure 5.8 proved that the equivalent circuit in Figure 5.9 was relevant in explaining the faradic and capacitive phenomena taking place at the material-solution interface of the defective MMC material.

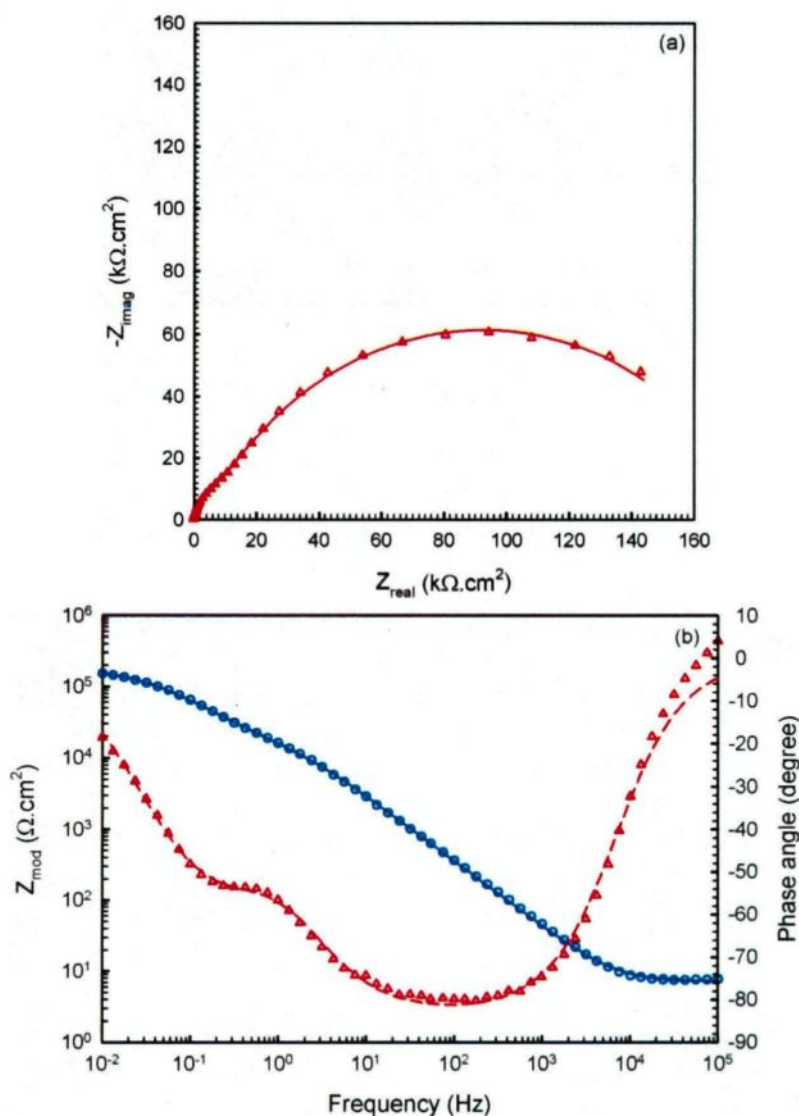


Figure 5.8 Typical (a) Nyquist and (b) Bode plots of AA1100-16 vol. % B<sub>4</sub>C MMC samples with defective surfaces obtained after a 3-hour immersion period in a 0.5 M K<sub>2</sub>SO<sub>4</sub> solution (experimental data and fitted curves are respectively presented by points and lines).

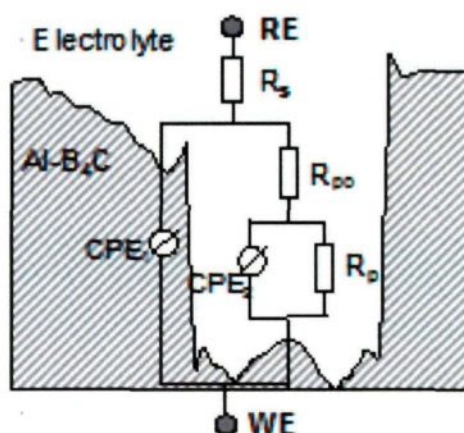


Figure 5.9 Equivalent circuit to interpret EIS spectra obtained from samples with defective surfaces (the pore section was taken from Figure 5.5; RE: reference electrode; WE: working electrode).

Table 5.4 Electrochemical parameters calculated from the equivalent circuit in Figure 5.9.

| Corrosion parameters                                  | Values |
|---|--------|
| $R_s$ ( $\Omega \cdot \text{cm}^2$ )                  | 7.07   |
| $\text{CPE}_1$ ( $\mu\text{F} \cdot \text{cm}^{-2}$ ) | 7.174  |
| $\alpha_1$  | 0.926  |
| $R_{po}$ ( $\text{k}\Omega \cdot \text{cm}^2$ )       | 20.96  |
| $R_p$ ( $\text{k}\Omega \cdot \text{cm}^2$ )          | 158.0  |
| $\text{CPE}_2$ ( $\mu\text{F} \cdot \text{cm}^{-2}$ ) | 16.610 |
| $\alpha_2$  | 0.753  |

With the purpose of presenting how the Al-B<sub>4</sub>C MMC material behaved in a K<sub>2</sub>SO<sub>4</sub> solution as a function of immersion time, the Nyquist plots obtained at E<sub>ocp</sub> after 3, 24, 48, 96 and 120 hours of immersion in a 0.5 M K<sub>2</sub>SO<sub>4</sub> solution are exhibited in Figure 5.10a. It was observed that the curve shape did not really change with time, indicating that the same corrosion mechanism was expected to control the dissolution of the MMC during the time span. Figure 5.10b shows that the polarization resistance almost linearly decreased from

550  $\text{k}\Omega\cdot\text{cm}^2$  to 160  $\text{k}\Omega\cdot\text{cm}^2$  within the first 96 hours of immersion meaning that the composite corrosion resistance decreased progressively with time. However, as the  $R_p$  value was found to increase during the last 24-hour immersion period, this indicated the initial formation of a passive protective layer over the dissolution process of the material.

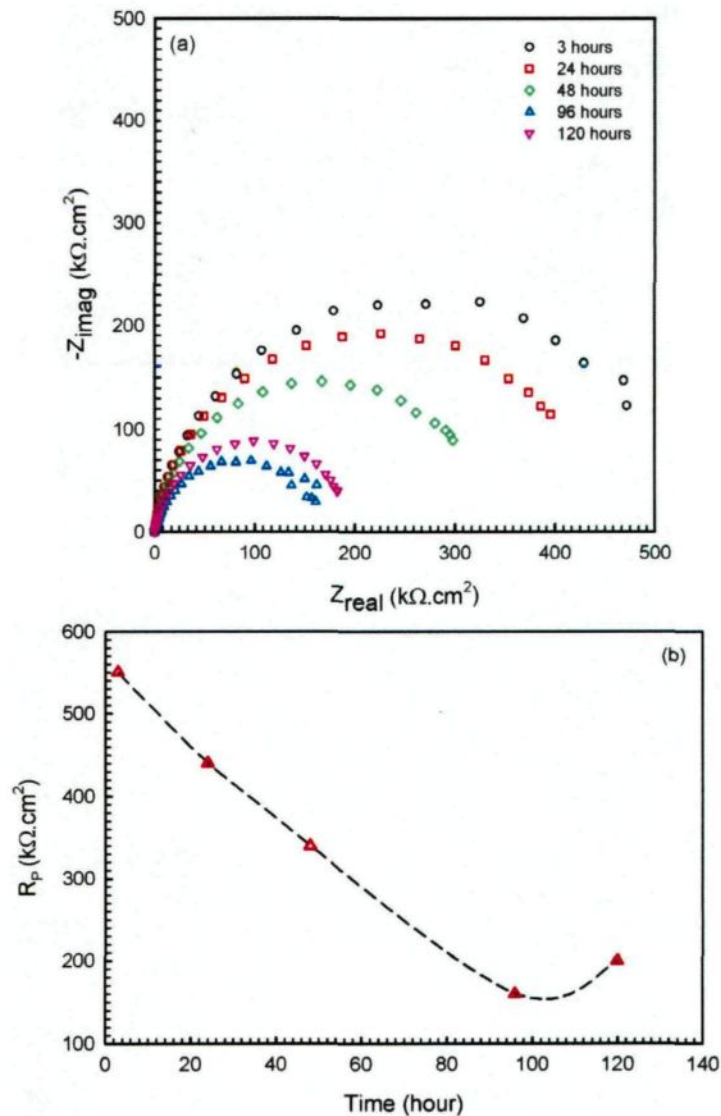


Figure 5.10 (a) Nyquist plots of the composite with uniform surface obtained after 3, 24, 48, 96 and 120 hours' immersion times in a 0.5 M  $\text{K}_2\text{SO}_4$  solution; (b) plot showing polarization resistance varying with time.

### 5.3.3 Morphology and Characterization of Corrosion Products

Figure 5.11a and Figure 5.11b show the surface morphology of AA1100-16 vol. % B<sub>4</sub>C MMCs before and after 120 hours' immersion in a 0.5 M K<sub>2</sub>SO<sub>4</sub> solution. As expected and since SO<sub>4</sub><sup>2-</sup> species were not found to be aggressive toward the MMCs, there was no appreciable degradation under this condition. To obtain noticeable corrosion, facilitate the on-premise analysis and not significantly change the mechanisms sustaining interfacial phenomena, the composite was immersed in a 0.5 M K<sub>2</sub>SO<sub>4</sub> solution without agitation. It was expected that the unstirred condition would favor passive film thickening by minimizing its dissolution or mechanical removal. Figure 5.11c exhibits the corroded surface morphology where film cracking was clearly observed around the B<sub>4</sub>C particles. This phenomenon was attributed to the film dehydration upon removal of the sample from the solution.

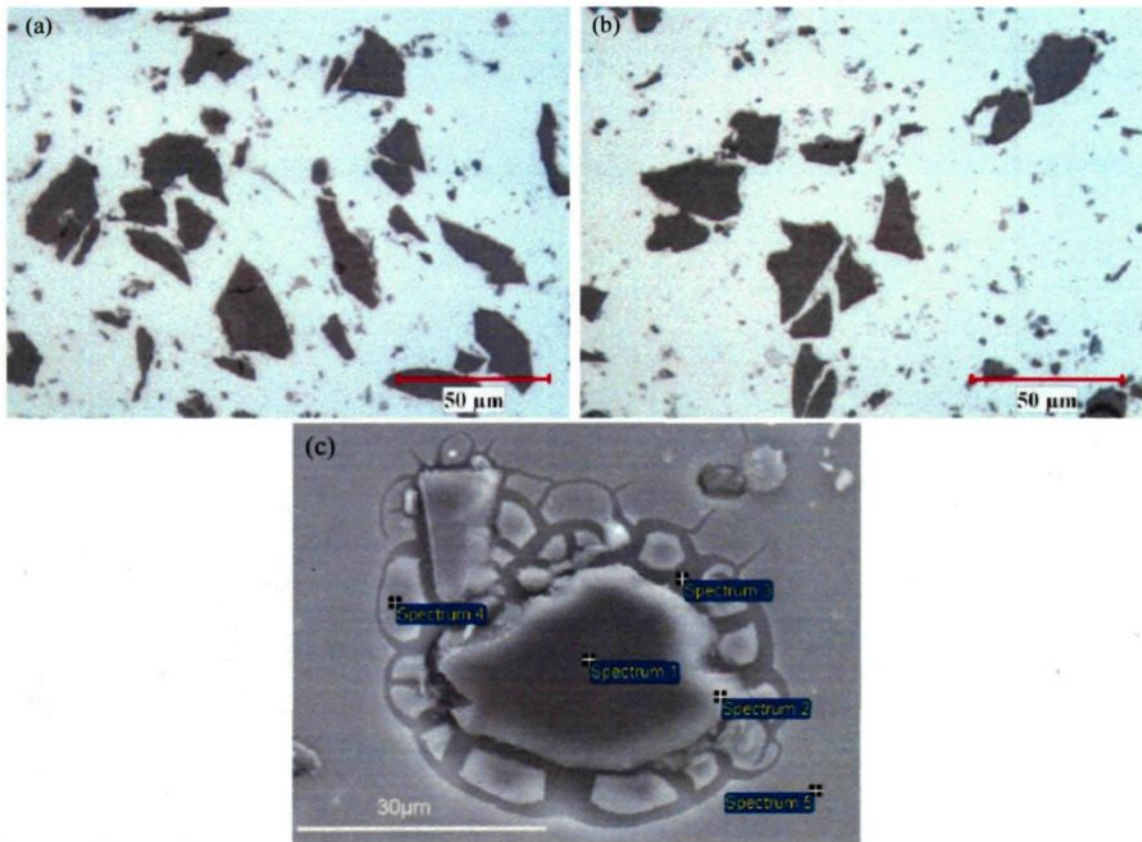


Figure 5.11 Optical and SEM micrographs showing the surface morphology of AA1100 – 16 vol. % B<sub>4</sub>C MMC (a) before corrosion and after a 120-hour immersion in a 0.5 M K<sub>2</sub>SO<sub>4</sub> solution (b) with agitation and (c) without agitation.

To resolve the nature of the cracked layer, EDS was employed. Figure 5.12 presents the corresponding EDS results of Figure 5.11c. “Spectrum 1” points the B<sub>4</sub>C particle. “Spectrum 2” reveals that B<sub>4</sub>C particle boundaries are rich in Ti, Al, O and other trace elements. “Spectrum 3” shows the Al matrix under the cracked layer. “Spectrum 4” and “Spectrum 5” indicate that the cracked and uncracked layers are rich in Al and O.

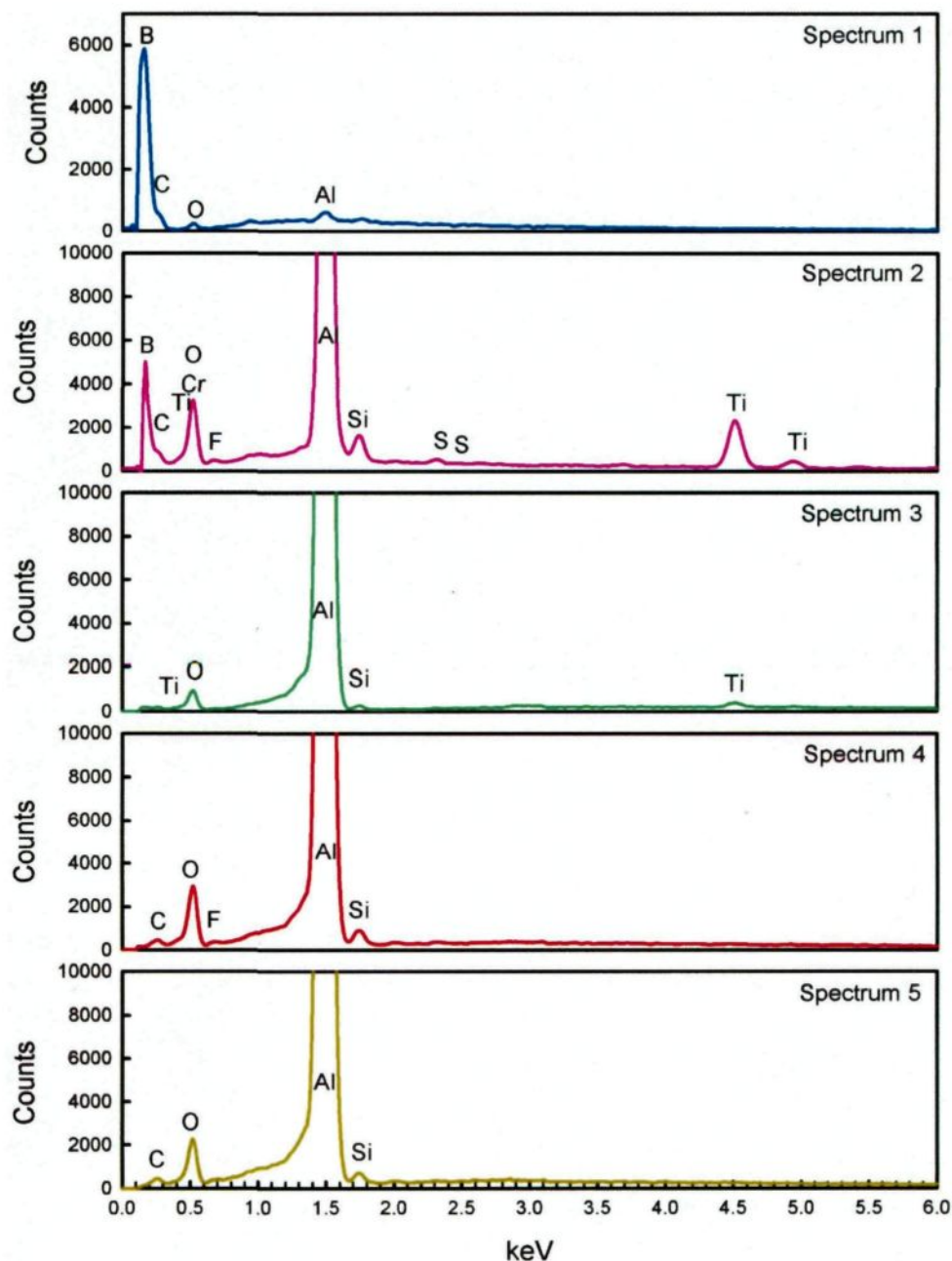


Figure 5.12 Corresponding EDS results of Figure 5.11: “Spectrum 1” points the  $B_4C$  particle; “Spectrum 2” reveals that the  $B_4C$  boundaries are rich in Ti, Al, O and trace elements; “Spectrum 3” exhibits the Al matrix under the cracked layer, “Spectrum 4” and “Spectrum 5” indicate the cracked and uncracked layer as Al oxide.

For further identification of the cracked layer, IRRAS measurements were performed.

Figure 5.13a presents the IR spectra of corroded and non-corroded samples. Figure 5.13b

shows the IR spectra difference of the two curves recorded in Figure 5.13a. A broad IR absorption band centered at about  $3500\text{ cm}^{-1}$  is, according to the literature,<sup>[29, 30]</sup> attributed to O-H stretching vibrations in bayerite  $\text{Al}(\text{OH})_3$ . The peak at about  $1600\text{ cm}^{-1}$  is associated with the H-OH bending vibration of absorbed water, and the peaks in the  $\sim 900 - 1200\text{ cm}^{-1}$  range represent the Al-OH vibrations.<sup>[31, 32]</sup> In order to confirm the nature of the corrosion product layer suspected from IRRAS experiments, XPS tests were carried out and the results are presented in Figure 5.14. Figure 5.14a and Figure 5.14b respectively depict the Al2p XP spectra of composite samples before and after corrosion. It could be observed that metallic Al was always present on the surface, whether corroded or not, and showed that the oxide film thickness was in the 1-10 nm range. It was noted that the intensity ratio of  $\text{Al}_{\text{oxide}}/\text{Al}_{\text{metal}}$  increased after corrosion, indicating that the oxide film thickness increased during immersion.<sup>[33]</sup> It was also observed that before corrosion, the Al2p oxide core level could be curve fitted with only one symmetric component at 74.67 eV which is attributed to  $\text{Al}_2\text{O}_3$ . After corrosion, the Al2p oxide core level was best synthesized with two components centered at 74.82 eV and 75.52 eV and was respectively associated with  $\text{Al}_2\text{O}_3$  and bayerite  $\text{Al}(\text{OH})_3$ .<sup>[34]</sup> This implied that  $\text{Al}_2\text{O}_3$  was the main Al oxide found on the surface of the composite before corrosion, and bayerite  $\text{Al}(\text{OH})_3$  was produced on the surface during corrosion in the sulfate environment. These results were consistent with the IRRAS measurements.

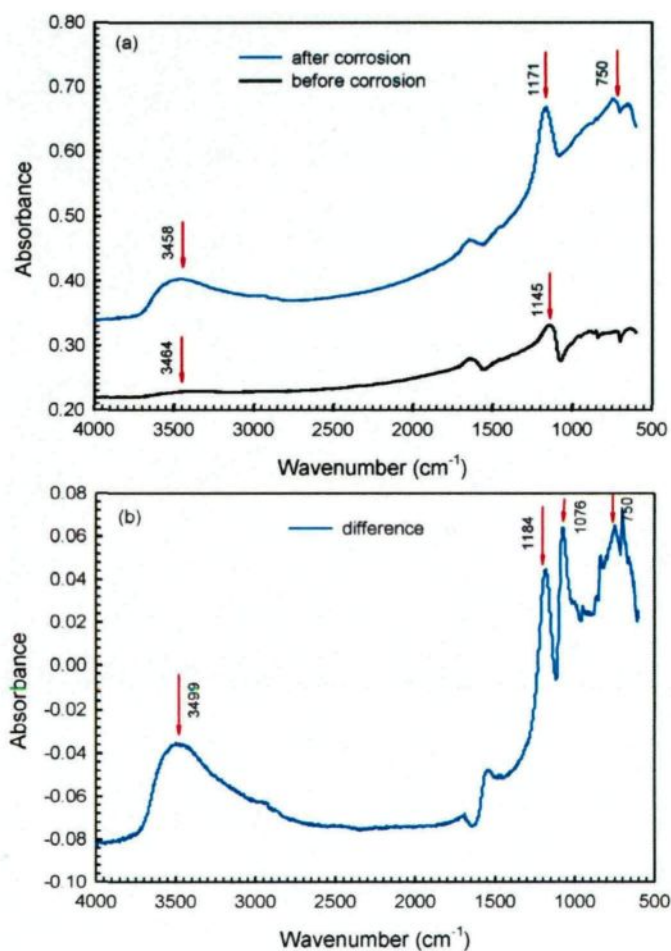


Figure 5.13 IRRAS spectra of AA1100-16 vol. %  $\text{B}_4\text{C}$  MMCs obtained from different conditions: (a) before and after 120-hour corrosion, (b) the difference of the two spectra seen in (a) with a corrected baseline.

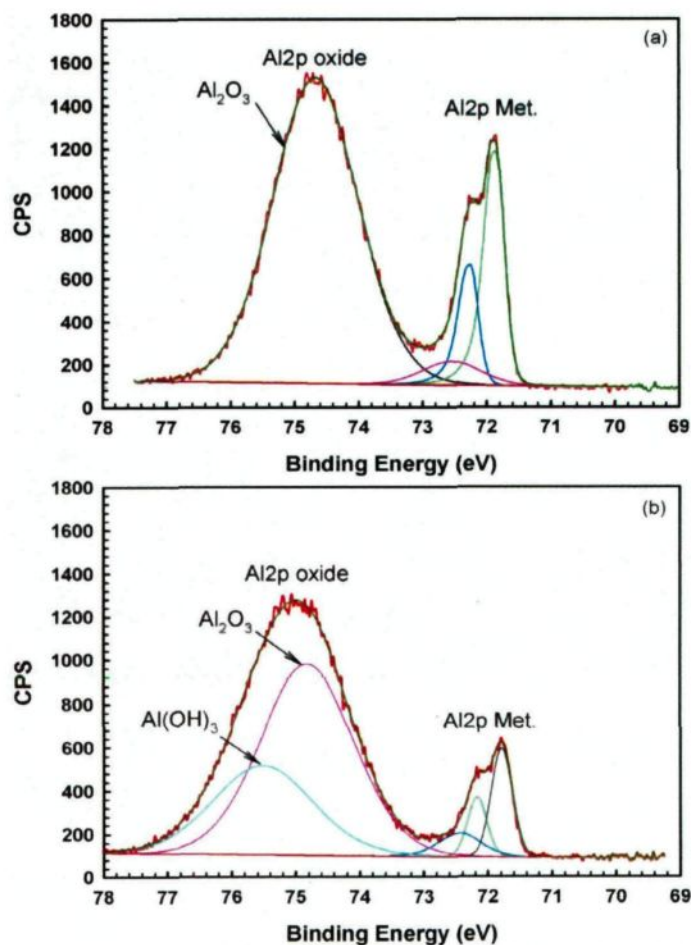


Figure 5.14 X-ray photoelectron Al<sub>2</sub>p spectra of AA1100 -16 vol. % B<sub>4</sub>C samples (a) before corrosion and (b) after 120 hours corrosion in a 0.5 M K<sub>2</sub>SO<sub>4</sub> solution.

An interesting and noticeable but occasional fact was the preferential deposition of small nodules over the B<sub>4</sub>C particles after the composite was immersed in a 0.5 M K<sub>2</sub>SO<sub>4</sub> solution (Figure 5.15a). Elemental mapping results in Figure 5.15b and Figure 5.15c indicate that these small nodules are rich in Cu and O. From the Al-Cu alloys in a 0.59 M NaCl solution, other researchers<sup>[35-37]</sup> observed similar copper nodules over the Al (Cu, Fe, Mn) intermetallic phase. According to these authors, the copper originated from the Al (Cu, Mg) intermetallic in the alloy, which formed a galvanic couple with the Al (Cu, Fe, Mn) phase. Under this galvanic effect, Al (Cu, Mg) intermetallics acted as an anode, the Al and

Mg elements were first dealloyed and the remaining copper then dissolved due to its porous structure. Owing to the cathodic character of intermetallics, the local pH around Al (Cu, Fe, Mn) was expected to be alkaline and the dissolved copper could thus re-precipitate as an oxide and preferentially be deposited on Al (Cu, Fe, Mn) intermetallics. The copper source in the present investigation was peculiar since very little copper (less than 2.20  $\mu\text{g/L}$ ) was present in the  $\text{K}_2\text{SO}_4$  solution and in the tap water (280  $\mu\text{g/L}$ ). Thus, the copper's sole possible source was the AA1100 matrix which was, however, exposed to have less than 0.20 wt. % Cu. Authors Ding *et al.* <sup>[17]</sup> investigated the galvanic corrosion of  $\text{B}_4\text{C}$  reinforced 6092-T6 alloys by soaking the composite in a 0.5 M  $\text{Na}_2\text{SO}_4$  solution containing 3-5 ppm  $\text{H}_2\text{PtCl}_6$  for 5 hours (platinization method). They observed that Pt micro-particles predominantly precipitated on  $\text{B}_4\text{C}$  particles. For this reason, they concluded that  $\text{B}_4\text{C}$  particles were cathodic sites and induced galvanic effects on the corrosion of the 6092- $\text{B}_4\text{C}$  composites. Similarly, the preferential deposition of copper oxide over  $\text{B}_4\text{C}$  particles - while not in the matrix- would indicate the cathodic behavior of the  $\text{B}_4\text{C}$  particles.

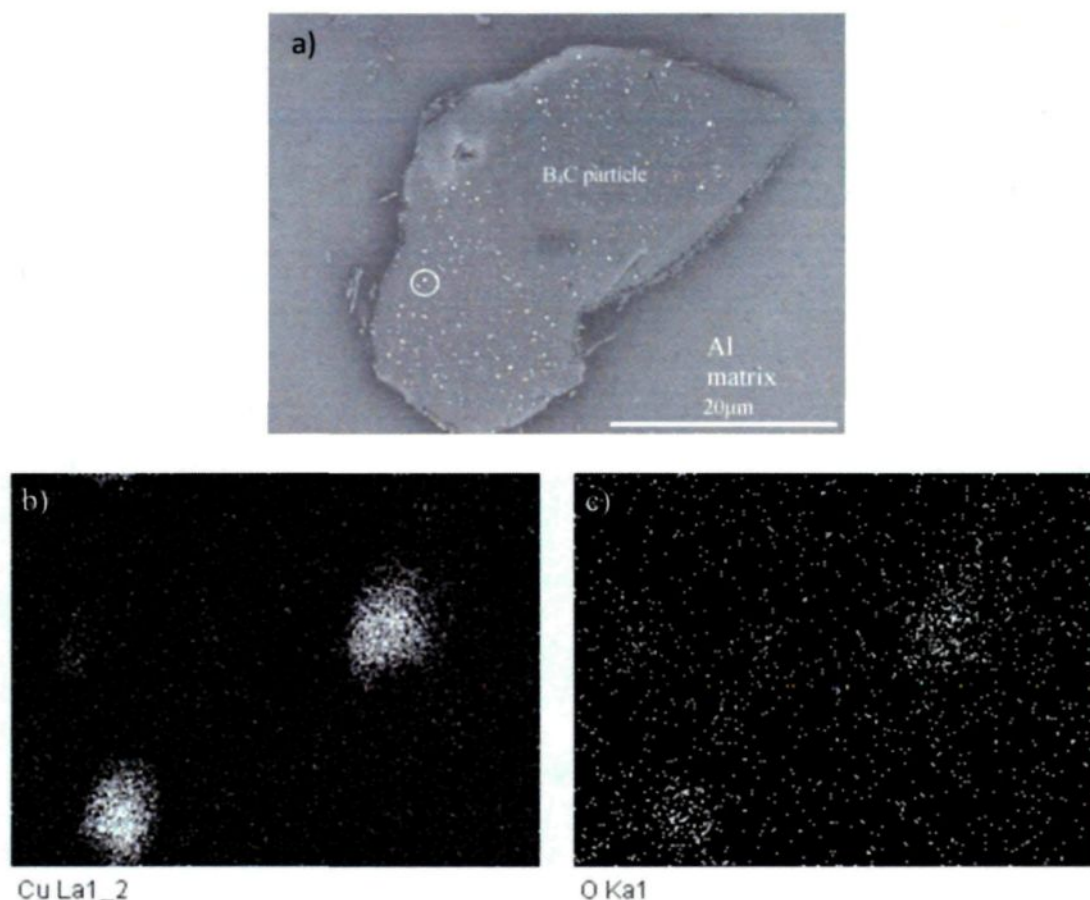
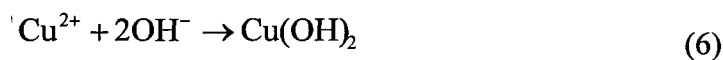
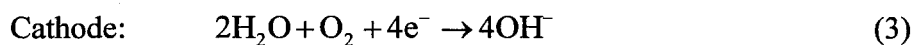
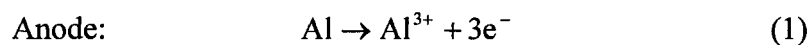


Figure 5.15 (a) SEM image showing the preferential deposition of small nodules over  $B_4C$  particles; (b) and (c) EDS elemental mappings showing that the small nodules contained within the circle in (a) are essentially composed of Cu and O.

The preferential deposition mechanism of copper over  $B_4C$  particles is schematically illustrated in Figure 5.16. At the material surface, the  $B_4C$  particles, peripheral Al matrix and intermetallic phase  $TiB_2$  were galvanically coupled. In this slightly alkaline environment ( $pH = 9.5$ ), the Al matrix and  $TiB_2$  layers acted as anodes and dissolved slowly as respectively shown by Equations 5.1 and 5.2, Under such pH conditions, the associated cathodic response was the reduction of the  $O_2$  and/or  $H_2O$  surrounding the  $B_4C$  particles, as indicated in Equations 5.3 and 5.4. Resulting from these reactions, the local pH became more alkaline. Hence, it was reasonable to suggest that bayerite  $Al(OH)_3$ ,

evidenced with the IRRAS and XPS results, was consequently produced in the neighborhood of the B<sub>4</sub>C particles according to the mechanism presented in Equation 5.5. This explained why O and Al appeared over the B<sub>4</sub>C particles in the EDS results (Spectrum 1). According to Bethencourt *et al.*,<sup>[38]</sup> while Cu is present in the matrix, the Al in the intermetallics will be first dealloyed and result in the remaining copper sponge-like structure. Owing to this structure, the copper dissolved and, due to the locally high pH close to the B<sub>4</sub>C particle, it precipitated as an oxide over the B<sub>4</sub>C particles (Equation 5.6).



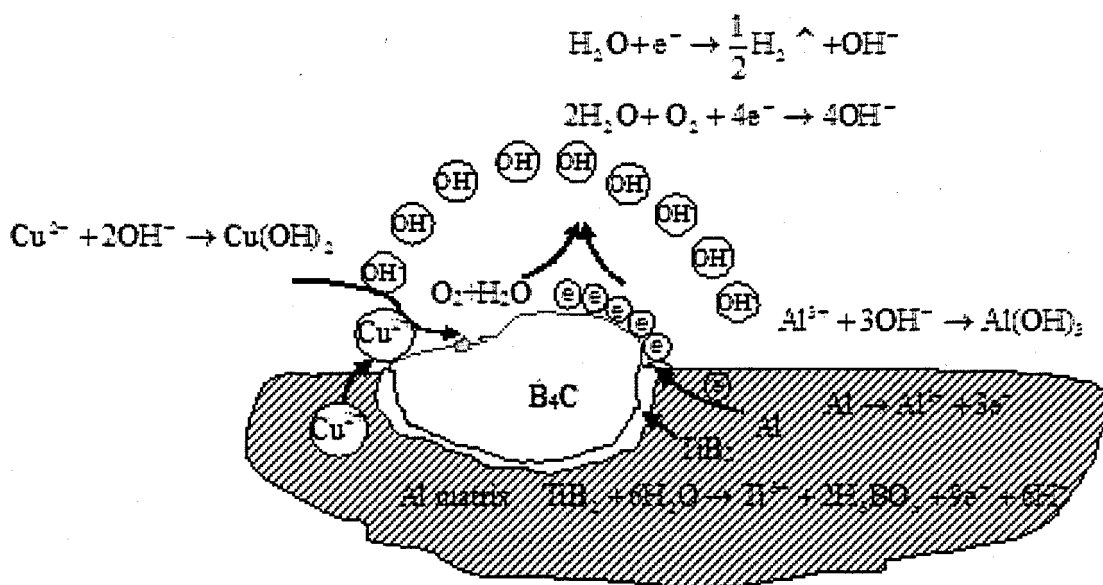


Figure 5.16 The schematic diagram showing the preferential deposition mechanism of copper oxide over B<sub>4</sub>C particles.

#### 5.4 Conclusions

The corrosion behavior of AA1100-16 vol. % B<sub>4</sub>C MMCs was systematically investigated using EIS, potentiodynamic polarization, optical microscopy, SEM, profilometry, IRRAS and XPS. The following conclusions could be drawn.

- (1) The AA1100-16 vol. % B<sub>4</sub>C material shows great corrosion resistance in a 0.5 M K<sub>2</sub>SO<sub>4</sub> solution.
- (2) Surface defects such as porosities can significantly reduce the corrosion resistance of the composite and change the corrosion impedance spectra from one to two capacitive loops.
- (3) The K<sub>2</sub>SO<sub>4</sub> solution does not induce pitting of the composite even under high polarization conditions. In contrast, pitting is provoked in a 3.5% NaCl solution and preferentially occurs at Al/B<sub>4</sub>C interfaces.

(4) The B<sub>4</sub>C particles show a cathodic character with respect to the peripheral matrix. The associated anodic response is the dissolution of the aluminum matrix and the TiB<sub>2</sub> layer. The consequent corrosion product is bayerite Al(OH)<sub>3</sub>.

## References

- [1] X.-G. Chen, "Application of Al-B<sub>4</sub>C Metal Matrix Composites in the Nuclear Industry for Neutron Absorber Materials", in: *Proceedings of the Symposium on Solidification Processing of Metal Matrix Composites*, W.H. Hunt and N. Gupta (Eds.), TMS, 2006, pp. 343-350.
- [2] X.-G. Chen, R. Hark, "Development of Al-30%B<sub>4</sub>C Metal Matrix Composites for Neutron Absorber Material", in: *Proceedings of Aluminium Alloys: Fabrication, Characterization and Applications* W. Yin and S.K. Das (Eds.), TMS, 2008, pp. 3-9.
- [3] G. Bonnet, V. Rohr, X.-G. Chen, J.L. Bernier, R. Chiocca, H. Issard, "Use of Alcan's Al-B<sub>4</sub>C Metal Matrix Composites as Neutron Absorber Material in TN International's Transportation and Storage Casks", *Packaging, Transport, Storage and Security of Radioactive Material*, 20 (2009) 98-102.
- [4] A.R. Kennedy, "The Microstructure and Mechanical Properties of Al-Si-B<sub>4</sub>C Metal Matrix Composites", *Journal of Materials Science*, 37 (2002) 317-323.
- [5] C. Brown, C.G. Interrante, L.R. Abramson, "Neutron Absorbers: Qualification and Acceptance Tests", in: *Proceeding of the 13<sup>th</sup> International Symposium on Packaging and Transportation of Radioactive Materials (PATRAM)*, (Eds.), 2001, pp. 201-205.
- [6] L.H. Hihara, R.M. Latanision, "Corrosion of Metal Matrix Composites", *International Materials Review*, 39 (1994) 245-263.
- [7] M.S.N. Bhat, M.K. Surappa, H.V.S. Nayak, "Corrosion Behaviour of Silicon Carbide Particle Reinforced 6061/Al Alloy Composites", *Journal of Materials Science*, 26 (1991) 4991-4996.
- [8] H. Sun, E.Y. Koo, H.G. Wheat, "Corrosion Behavior of SiCp/6061 Al Metal Matrix Composites", *Corrosion*, 47 (1991) 741-753.
- [9] I.B. Singh, D.P. Mandal, M. Singh, S. Das, "Influence of SiC Particles Addition on the Corrosion Behavior of 2014 Al-Cu Alloy in 3.5% NaCl Solution", *Corrosion Science*, 51 (2009) 234-241.
- [10] S. Roepstorff, E. Maahn, "Corrosion Resistance of Aluminum-Silicon Carbide Composite Materials", in: *Proceeding of 12th Scandinavian Corrosion Congress and Eurocorr'92*, P.J. Tunturi (Eds.), Corrosion Society of Finland, 1992, pp.

- [11] L.H. Hihara, "Corrosion of Aluminum-Matrix Composites", *Corrosion Reviews*, 15 (1997) 361-386.
- [12] H. Ding, L. Hihara, "Localized Corrosion Currents and pH Profile Over B<sub>4</sub>C, SiC, and Al<sub>2</sub>O<sub>3</sub> Reinforced 6092 Aluminum Composites: I. In 0.5 M Na<sub>2</sub>SO<sub>4</sub> Solution", *Journal of the Electrochemical Society*, 152 (2005) B161-B167.
- [13] R. Emmerich, W. Ensinger, B. Enders, "Corrosion Behaviour of Borated Aluminium Used as a Neutron Absorber", *Journal of European Archaeology*, 16 (2005) 151-156.
- [14] A. Machiels, R. Lambert, Handbook of Neutron Absorber Materials for Spent Nuclear Fuel Transportation and Storage Applications, Palo Alto, 2006.
- [15] Qualification of METAMIC® for Spent-Fuel Storage Application, EPRI, 2001.
- [16] F. Zucchi, G. Trabanelli, V. Grassi, A. Frignani, "Corrosion Behavior in Sodium Sulfate and Sodium Chloride Solutions of SiCp Reinforced Magnesium Alloy Metal Matrix Composites", *Corrosion*, 60 (2004) 362-368.
- [17] H. Ding, L. Hihara, "Electrochemical Behavior of Boron Carbide and Galvanic Corrosion of Boron Carbide Reinforced 6092 Aluminum Composites", *ECS Transactions*, 1 (2006) 103-114.
- [18] Z. Zhang, A. Charette, Ghomashchi, X.-G. R. Chen, "Effect of Titanium on Solidification Microstructure of Al-16%B<sub>4</sub>C Composites", in: *44th Annual Conference of Metallurgist of CIM*, J.P. Martin (Eds.), The Metallurgical Society of CIM, 2005, pp. 447-456.
- [19] J.-B. Jorcin, M.E. Orazem, N. Pébère, B. Tribollet, "CPE Analysis by Local Electrochemical Impedance Spectroscopy", *Electrochimica Acta*, 51 (2006) 1473-1479.
- [20] P. Zoltowski, "On the Electrical Capacitance of Interfaces Exhibiting Constant Phase Element Behaviour", *Journal of Electroanalytical Chemistry*, 443 (1998) 149-154.
- [21] J.R. Macdonald, W.R. Kenan, Impedance Spectroscopy: Emphasizing Solid Materials and Systems, John Wiley & Sons, 1987.
- [22] C. Monticelli, A. Frignani, A. Bellosi, G. Brunoro, G. Trabanelli, "The Corrosion Behaviour of Titanium Diboride in Neutral Chloride Solution", *Corrosion Science*, 43 (2001) 979-992.
- [23] B.S. Covino Jr, S.D. Cramer, J.P. Carter, D. Schlain, "Corrosion of Titanium Diboride", *Journal of the Less-Common Metals*, 41 (1975) 211-224.
- [24] A. Balbo, C. Monticelli, A. Bellosi, A. Pagnoni, "Corrosion of Alumina/Titanium Diboride Composites in Neutral and Acidic Chloride Solutions", *Materials and Corrosion*, 53 (2002) 471-478.
- [25] J.G. Kaufman, E.L. Rooy, *Aluminum Alloy Castings: Properties, Processes and Applications*, ASM International Ohio, 2004.

- [26] Basics of Electrochemical Impedance Spectroscopy, Gamry Instrument, 2007.
- [27] M.E. Orazem, B. Tribollet, *Electrochemical Impedance Spectroscopy*, John Wiley & Sons, Inc., 2008.
- [28] F. Mansfeld, An Introduction to Electrochemical Impedance Measurement, Solartron Ltd, 1999.
- [29] A. Violante, P.M. Huang, "Influence of Inorganic and Organic Ligands on the Formation of Aluminium Hydroxides and Oxyhydroxides", *Clays & Clay Minerals*, 33 (1985) 181-192.
- [30] S.L. Nail, J.L. White, S.L. Hem, "Comparison of IR Spectroscopic Analysis and X-Ray Diffraction of Aluminum Hydroxide Gel", *Journal of Pharmaceutical Sciences*, 64 (1975) 1166-1169.
- [31] A.C. Geiculescu, T.F. Strange, "A Microstructural Investigation of Low-Temperature Crystalline Alumina Films Grown on Aluminum", *Thin Solid Films*, 426 (2003) 160-171.
- [32] R. Frost, J.T. Kloprogge, S.C. Russell, J. Szetu, "Dehydroxylation of Aluminum (Oxo)hydroxides Using Infrared Emission Spectroscopy. Part II: Boehmite", *Applied Spectroscopy*, 53 (1999) 572-582.
- [33] B.R. Strohmeier, "An ESCA Method for Determining the Oxide Thickness on Aluminum Alloys", *Surface and Interface Analysis*, 15 (1990) 51-56.
- [34] J.T. Kloprogge, L.V. Duong, B.J. Wood, R.L. Frost, "XPS Study of the Major Minerals in Bauxite: Gibbsite, Bayerite and (Pseudo-)Boehmite", *Journal of Colloid and Interface Science*, 296 (2006) 572-576.
- [35] V. Guillaumin, G. Mankowski, "Localized Corrosion of 2024 T351 Aluminium Alloy in Chloride Media", *Corrosion Science*, 41 (1998) 421-438.
- [36] R.G. Buchheit, R.P. Grant, P.F. Hlava, B. Mckenzie, G.L. Zender, "Local Dissolution Phenomena Associated With S Phase (Al<sub>2</sub>CuMg) Particles in Aluminum Alloy 2024-T3", *Journal of the Electrochemical Society*, 144 (1997) 2621-2628.
- [37] D. Zhu, W.J. van Ooij, "Corrosion Protection of AA 2024-T3 by Bis-[3-(triethoxysilyl)propyl]tetrasulfide in Sodium Chloride Solution.: Part 2: Mechanism for Corrosion Protection", *Corrosion Science*, 45 (2003) 2177-2197.
- [38] M. Bethencourt, F.J. Botana, M.J. Cano, M. Marcos, J.M. Sánchez-Amaya, L. González-Rovira, "Behaviour of the Alloy AA2017 in Aqueous Solutions of NaCl. Part I: Corrosion Mechanisms", *Corrosion Science*, 51 (2009) 518-524.

## **CHAPTER 6**

### **CORROSION INHIBITION OF Al-B<sub>4</sub>C METAL MATRIX COMPOSITES IN A NaCl SOLUTION BY BENZOTRIAZOLE**

## CHAPTER 6

### CORROSION INHIBITION OF Al-B<sub>4</sub>C METAL MATRIX COMPOSITES IN A NaCl SOLUTION BY BENZOTRIAZOLE

#### Abstract

Benzotriazole (BTAH) was used for the first time to inhibit the corrosion of Al-B<sub>4</sub>C composites in a NaCl solution. Its corrosion inhibition effect was systematically investigated as a function of BTAH concentrations, volume fractions of B<sub>4</sub>C particles and immersion time by using potentiodynamic polarization, electrochemical impedance and infrared reflection adsorption spectroscopy techniques. It was found that BTAH is an efficient corrosion inhibitor for the Al-B<sub>4</sub>C MMCs in a 3.5 g/L NaCl solution, and its inhibition efficiency increased when increasing the BTAH concentration. For the same BTAH concentration and immersion time, higher B<sub>4</sub>C volume fraction leads to a higher corrosion inhibition efficiency. The inhibition efficiency of benzotriazole was also influenced by the immersion time: the inhibition efficiency increases with the immersion time in the first 18 hours. However, prolonging the immersion time leads to a decrease in the inhibition efficiency. As the BTAH was an inhibitor with a cathodic character and it inhibited corrosion by physically adsorbing on B<sub>4</sub>C particles at the composite surface, it obeyed the Freundlich adsorption isotherm.

## 6.1 Introduction

Al-B<sub>4</sub>C metal matrix composites (MMCs) have received considerable attention due to their light weight, superior thermal conductivity, high stiffness and their hardness. [1] Owing to the special capturing neutron ability of isotope B<sup>10</sup>, Al-B<sub>4</sub>C MMCs have been increasingly used as excellent neutron absorber materials to fabricate the inside basket of transport and storage casks for spent nuclear fuels in the nuclear industry. [2, 3]

Although the incorporation of B<sub>4</sub>C particles into an Al base alloy enhances its physical and mechanical properties, the corrosion resistance of such materials is a great concern for wider industrial applications. As reported in our previous studies, [4, 5] Al-B<sub>4</sub>C composites in 0.5 M K<sub>2</sub>SO<sub>4</sub>, 3.5% NaCl and 2500 ppm Boron-containing H<sub>3</sub>BO<sub>3</sub> solutions showed lower polarization resistance than the base AA1100 alloy. In addition, the polarization resistances of the composites in all three solutions decreased when increasing the B<sub>4</sub>C particle volume fraction. This can be explained by the fact that the reinforcement B<sub>4</sub>C particles provoke the discontinuity of the protective aluminum oxide film, and thereby increase the number of sites where corrosion can be initiated. Higher B<sub>4</sub>C particle levels result in more severe discontinuities and thus more corrosion sites. The B<sub>4</sub>C particles could form galvanic couples with the Al matrix which could also stimulate the corrosion process on the Al matrix. Of all three solutions investigated, the NaCl solution is the most corrosive since pitting corrosion is easily provoked at the interfaces of Al matrix/B<sub>4</sub>C particles. However, very little literature is reported on the corrosion protection of the Al-B<sub>4</sub>C composite in the corrosive media. Therefore, it becomes of great technical interest to study the corrosion control of Al-B<sub>4</sub>C composites in a NaCl solution by using suitable methods.

A variety of methods such as anodizing <sup>[6-8]</sup> and rare earth chloride inhibition <sup>[9-11]</sup> have been suggested for the protection of aluminum metal matrix composites from corrosion. The organic compounds containing heteroatoms N, O, and S in the molecules were reported to be effective inhibitors for Al alloys in an environment containing aggressive ions. <sup>[12-14]</sup> It is believed that organic compounds inhibit the corrosion of Al alloys in some aggressive media by adsorbing on the material surface and forming a physical barrier between the material surface and the aggressive media. The adsorption process is influenced by the nature and surface charge of the alloy surface, the chemical structure of the organic inhibitors, the type of electrolyte and the type of interaction between the organic molecules and the metallic surface. <sup>[15]</sup>

For more than sixty years, benzotriazole, conveniently abbreviated as BTAH (Figure 1), has been known to be an effective inhibitor for copper and its alloys. <sup>[16-18]</sup> It has been recently reported to be an effective corrosion inhibitor for iron <sup>[19,20]</sup> and aluminum alloys. <sup>[21]</sup> In the present paper, the benzotriazole was tentatively used as a corrosion inhibitor for Al-B<sub>4</sub>C composites in a NaCl solution.

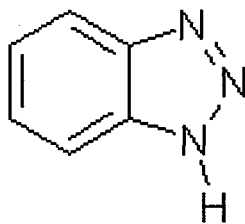


Figure 6.1 Chemical structure of BTAH.

The present work aims at investigating the inhibitive effect of BTAH on the corrosion of Al-B<sub>4</sub>C composites in a 3.5 g/L NaCl solution at different concentrations of

BTAH, at different volume fractions of B<sub>4</sub>C particles as well as at different immersion times. The study was carried out using potentiodynamic polarization (PDP) and electrochemical impedance spectroscopy (EIS) techniques. Infrared reflection absorption spectroscopy (IRRAS) was used as a supplementary method to identify the adsorbed BTAH on the composite surface.

## 6.2 Experimental Procedures

### 6.2.1 Preparation of Samples and Electrolytes

The composites investigated were AA1100-16 vol.% B<sub>4</sub>C and AA1100-30 vol.% B<sub>4</sub>C in the form of rolled sheets, supplied by Rio Tinto Alcan (Saguenay, Quebec, Canada). The designate chemical composition of the base alloy is listed in Table 6.1. Samples were cut into small 20 by 20 by 4.3 mm thick pieces , sanded with a 3M Scotch-Brite™ MMM69412 surface conditioning disc (5 inches in diameter, extra-fine surface finish), degreased with acetone and then rinsed with nanopure water. Finally, all specimens were dried with clean compressed air. Analytical reagent grade NaCl was used to obtain the 3.5g/L NaCl electrolyte. Nanopure water (15.2 MΩ.cm) was used in all experiments.

Table 6.1 Designated chemical composition of the base AA1100 alloy.

| Elements               | Al     | Cu           | Mn      | Si+Fe  | Zn     | others |
|------------------------|--------|--------------|---------|--------|--------|--------|
| Composition<br>(wt. %) | ≥ 99.0 | 0.050 - 0.20 | ≤ 0.050 | ≤ 0.95 | ≤ 0.10 | ≤ 0.15 |

## 6.2.2 Electrochemical Measurements

The potentiostat employed in the present study was a Reference 600 instrument (Gamry Instruments, Warminster, PA, USA). Electrochemical investigations were performed using a 300 cm<sup>3</sup> - EG&G PAR flat cell (London Scientific, London, ON, Canada) with an Ag/AgCl electrode as the reference electrode and a platinum mesh as the counter electrode (CE). The corrosion cell had an 1-cm<sup>2</sup> orifice as the working surface. Prior to the electrochemical measurements, and if not otherwise mentioned, the samples were immersed in the solution for one hour to ensure a steady opened circuit potential ( $E_{ocp}$ ). To test the effect of the immersion time in section 3.3, the electrochemical measurements were performed after immersing the samples in the solutions for desired times varying from 1 to 120 hours. Magnetic stirring was employed at the cell bottom to increase the mass transfer at the electrode surface.

Potentiodynamic polarization tests were performed at a scan rate of 1 mV s<sup>-1</sup> with the scans being taken from -250 mV below  $E_{ocp}$  to the potential at which a 1mA.cm<sup>-2</sup> current density was recorded. The polarization resistance ( $R_p$ ) values were calculated from the slope of linear E - j curves found by varying  $\pm 10$  mV around the  $E_{corr}$ . The EIS curves were obtained by applying a sinusoidal potential of 10 mV in amplitude around the  $E_{ocp}$  at a steady-state in the 100 kHz to 10 mHz frequency range. In all cases, the tests were duplicated at least once to ensure the reproducibility of the results. Using the Gamry Instruments Echem Analyst software, the impedance parameters were calculated by fitting the experimental data to an equivalent circuit model.

### 6.2.3 Infrared Reflection-Absorption Spectroscopy

Infrared reflection-absorption spectroscopy (IRRAS) was used to characterize the sample surfaces after immersion in a NaCl solution with different BTAH concentrations. The IRRAS operated using a Nicolet 6700 spectrometer (ThermoFisher Scientific) equipped with a Mid-IR MCT-B wide band N<sub>2</sub>-cooled detector and a XT-KBr beam splitter. The Smart SAGA (Specular Apertured Grazing Angle) accessory was used to analyze samples at an average incidence angle of 80° relative to the normal surface. The spectra were recorded from 4000 to 650 cm<sup>-1</sup> with a resolution of 4 cm<sup>-1</sup> and 64 scans. The IR radiation was p-polarized, and the resulting spectrum was subtracted from a background spectrum taken from a clean gold-coated reference sample. All the IRRAS spectra results were processed using the OMNIC software provided by the instrument manufacturer.

## 6.3 Results and Discussion

### 6.3.1 Effect of BTAH on the Inhibition Efficiency

The effect of benzotriazole on the corrosion inhibition of AA1100-16 vol.% B<sub>4</sub>C was investigated by varying the BTAH concentration in an aggressive 3.5 g/L NaCl solution. Table 6.1 presents the potentiodynamic polarization curves of AA1100-16 vol.% B<sub>4</sub>C in the NaCl solution containing 0 to 0.15 M BTAH. For each curve, the corrosion current density was determined by the extrapolation of cathodic Tafel slopes to the respective corrosion potentials. The polarization resistance ( $R_p$ ) values were obtained from the slope of the E - i curves by varying  $\pm 10$  mV around the  $E_{\text{corr}}$ . The surface coverage  $\theta$  of the inhibitor at different concentrations was calculated from the equation. <sup>[22]</sup>

$$\theta = \frac{j_{\text{corr}}(\text{uninh}) - j_{\text{corr}}(\text{inh})}{j_{\text{corr}}(\text{uninh})}$$

where  $j_{\text{corr}}(\text{uninh})$  is the corrosion current density in the 3.5 g/L NaCl solution without the inhibitor (*i.e.*  $1.77 \mu\text{Acm}^{-2}$ ) and  $j_{\text{corr}}(\text{inh})$  is the corrosion current density in the 3.5 g/L NaCl solution with different concentrations of the inhibitor. The inhibition efficiency (IE) was thereafter calculated using the following equation:

$$\text{IE} (\%) = \theta \times 100$$

The calculated electrochemical parameters ( $E_{\text{corr}}$ ,  $j_{\text{corr}}$ ,  $R_p$  and I.E.), associated with the polarization measurements at different BTAH concentrations, are presented in Table 6.2.

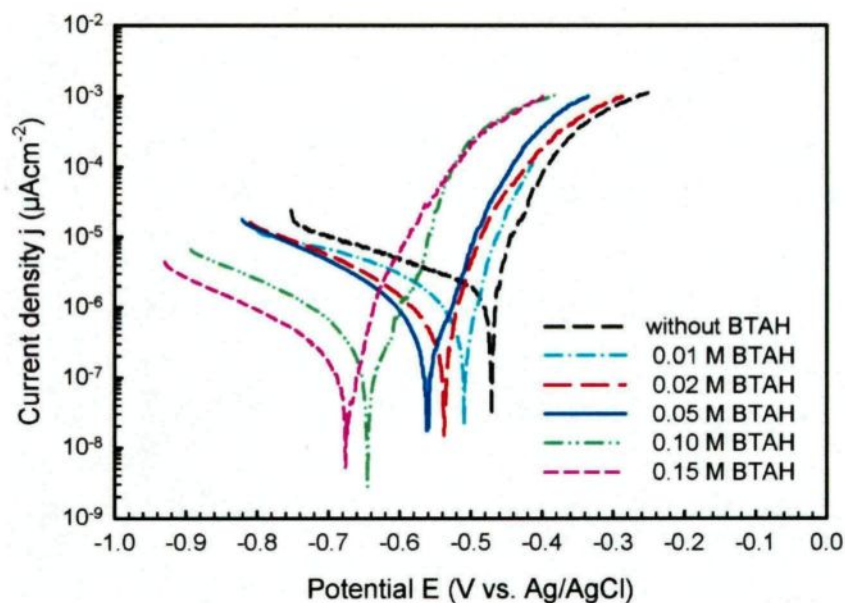


Figure 6.2 Potentiodynamic polarization curves of AA1100-16 vol.% B<sub>4</sub>C in a 3.5 g/L NaCl solution containing different BTAH concentrations.

Data presented in Table 6.2 clearly show that the addition of BTAH to a 3.5 g/L NaCl solution significantly decreases the corrosion current density and consequently inhibits the dissolution of the AA1100-16 vol.% B<sub>4</sub>C composite. Indeed, in the 3.5 g/L

NaCl solution, without any BTAH addition, a corrosion current density of  $1.77 \mu\text{A cm}^{-2}$  was found to characterize the Al-B<sub>4</sub>C composite. When 0.05 M of BTAH was added to the solution, the current density decreased to  $0.89 \mu\text{A cm}^{-2}$  and results in an inhibition efficiency of 49.7%, which is more than two times greater than that obtained in the solution containing 0.01 M of BTAH. Notably, with a further increase of the BTAH concentration to 0.15 M, the corrosion current density decreased considerably to  $0.25 \mu\text{A cm}^{-2}$ , resulting in a corrosion inhibition efficiency of up to 85.9%, denoting that BTAH is a highly suitable corrosion inhibitor for the Al-B<sub>4</sub>C composite in a 3.5 g/L NaCl solution. Although the inhibition efficiency increases along with the BTAH concentration, the relationship between these two parameters is, however, non-linear. As suggested in Figure 6.3, the inhibition mechanism may be governed by a complex equilibrium condition between the dissolved and the adsorbed BTAH species, which can be mathematically described by an adsorption isotherm that will be presented in Section 6.4.6.

It can be noticed from Figure 6.2 that addition of BTAH moves the  $E_{\text{corr}}$  to a more negative value and that this shift increases as the concentration of BTAH is increased in the solution. According to Li *et al.*,<sup>[23]</sup> if the displacement in corrosion potential is more than 85 mV in the negative direction with respect to the  $E_{\text{corr}}$  obtained in the solution without inhibitor, then the inhibitor could be considered as a cathodic type. In the present study, the maximum  $E_{\text{corr}}$  shift is more than 200 mV (*i.e.* from -471.2 to -676.0 mV) in the negative direction when the added BTAH concentration reached 0.15 M, indicating that BTAH acts as a cathodic reaction inhibitor.<sup>[24]</sup>

It is also observed in Figure 6.2 that the general aspect of cathodic and anodic portions of the potentiodynamic curves change only slightly with the addition of BTAH, suggesting that BTAH inhibits the corrosion of the Al-B<sub>4</sub>C composite in a NaCl solution without altering the corrosion mechanism. Therefore, the BTAH species would simply adsorb on the composite surface and partially block it from the corrosive media. [22] Because the B<sub>4</sub>C particles in the composite are cathodic sites and form galvanic coupling with the aluminum matrix, [5] it is suggested that BTAH, which acts as a cathodic inhibitor, preferentially adsorbs onto the B<sub>4</sub>C component. As a result, blocking these sites via an adsorption phenomenon decreases the corrosion current density by slowing down the cathodic reaction that sustains the aluminum dissolution reaction. In parallel and as expected, the polarization resistance of the composite was found to increase remarkably from 7.1 kΩcm<sup>2</sup> in the 3.5 g/L NaCl solution without BTAH, to 44.1 kΩcm<sup>2</sup> in the same NaCl solution with 0.05 M of BTAH addition, and to 164.3 kΩcm<sup>2</sup> when 0.15 M of BTAH was added.

Table 6.2 Electrochemical parameters obtained from PDP measurements of AA1100-16 vol.% B<sub>4</sub>C in 3.5 g/L NaCl with different concentrations of BTAH.

| Solution                 | $j_{\text{corr}}$<br>( $\mu\text{Acm}^{-2}$ ) | $E_{\text{corr}}$<br>(mV) | $R_p$<br>( $\text{k}\Omega\text{cm}^2$ ) | IE<br>(%) |
|--------------------------|---|---------------------------|--|-----------|
| 3.5 g/L NaCl             | 1.77  | -471.2                    | 7.1                                      | -         |
| 3.5 g/L NaCl+0.01 M BTAH | 1.40  | -509.6                    | 23.9                                     | 20.9      |
| 3.5 g/L NaCl+0.02 M BTAH | 1.17  | -537.8                    | 29.9                                     | 33.9      |
| 3.5 g/L NaCl+0.05 M BTAH | 0.89  | -562.0                    | 44.1                                     | 49.7      |
| 3.5 g/L NaCl+0.10 M BTAH | 0.51  | -644.9                    | 91.5                                     | 71.2      |
| 3.5 g/L NaCl+0.15 M BTAH | 0.25  | -676.0                    | 164.3                                    | 85.9      |

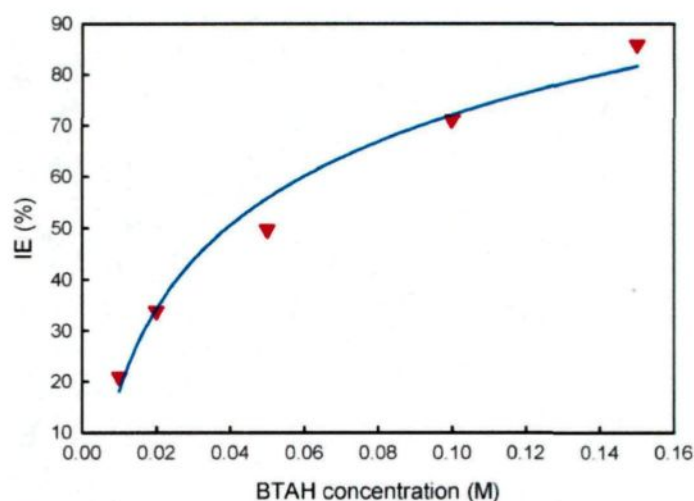


Figure 6.3 Variation of inhibition efficiency IE (%) as a function of BTAAH concentration in a 3.5 g/L NaCl solution.

### 6.3.2 Effect of B<sub>4</sub>C Particle Volume Fraction on The inhibition Efficiency

The effect of the B<sub>4</sub>C volume fraction on the BTAAH inhibition efficiency in a 3.5 g/L NaCl solution was studied by varying the B<sub>4</sub>C volume fraction from 0 (the base alloy) to 30 vol.%. For that purpose, a constant BTAAH concentration of 0.05 M was used. This BTAAH concentration was selected because it provides an intermediate inhibition efficiency of 49.7% when used with a composite of the intermediate B<sub>4</sub>C content (16 vol.%).

Figure 6.4a displays the potentiodynamic polarization curves of three materials obtained after a one-hour immersion in the 3.5 g/L NaCl solution without BTAAH. The derived electrochemical parameters are summarized in Table 6.3. In the NaCl solution without BTAAH, the base alloy, which is free of B<sub>4</sub>C particles, shows a slow transition to passivation between  $E_{\text{corr}}$  and -520 mV. This is the potential after which the current density steeply increases due to the breakdown of the passive film. The composites, however, are displaying the sudden current density increase at the very beginning of the anodic portion

of the polarization curve without showing any trend toward passivation. Moreover, the corrosion current density associated to composite materials was found to increase substantially from 0.76 to 16.46  $\mu\text{Acm}^{-2}$  with the  $\text{B}_4\text{C}$  volume fraction increasing from 0 to 30 %. The higher sensitivity toward the active dissolution and pitting corrosion of composites can be explained by the fact that the addition of  $\text{B}_4\text{C}$  particles to the base alloy increases the heterogeneity of the passive film and facilitates the access of  $\text{Cl}^-$  species to the aluminum matrix, especially at film disruptions in the vicinity of the  $\text{B}_4\text{C}$  particles. The galvanic coupling effect between the aluminum matrix and the  $\text{B}_4\text{C}$  particles is also considered to be responsible for the high corrosion current densities measured for the composites immersed in a NaCl solution. <sup>[5]</sup>

In Figure 6.4b, the passivation behavior of the AA1100 aluminum alloy becomes more obvious in the presence of BTAH. For the base alloy, BTAH was again found to move the corrosion potential in a cathodic direction by 80 mV, demonstrating that it acts as a cathodic inhibitor for the aluminum alloy by adsorbing at cathodic sites at the surface (e.g. intermetallic particles). Furthermore, when 0.05 M of BTAH was added to the chloride solution, as presented in Table 6.3, the corrosion current densities of the matrix and the composites were all lowered in comparison to those recorded in the absence of BTAH. The inhibition observed was particularly efficient for the composites, although the  $\text{B}_4\text{C}$  particles led to a severe discontinuity of the matrix and thus provide additional sites where corrosion could easily be initiated. Indeed, for the base alloy, only a slight  $j_{\text{corr}}$  decrease from 0.76 to 0.49  $\mu\text{Acm}^{-2}$  (I.E. = 29.0%) was obtained using 0.05 M of BTAH. On the other hand, for the composite with 30 vol.%  $\text{B}_4\text{C}$ , the  $j_{\text{corr}}$  remarkably decreased from 16.46 to 4.66  $\mu\text{Acm}^{-2}$ ,

indicating an inhibition efficiency of 71.7%. As previously presented, an intermediate inhibition efficiency of 49.7% was found to be associated with the 16 vol.% B<sub>4</sub>C material.

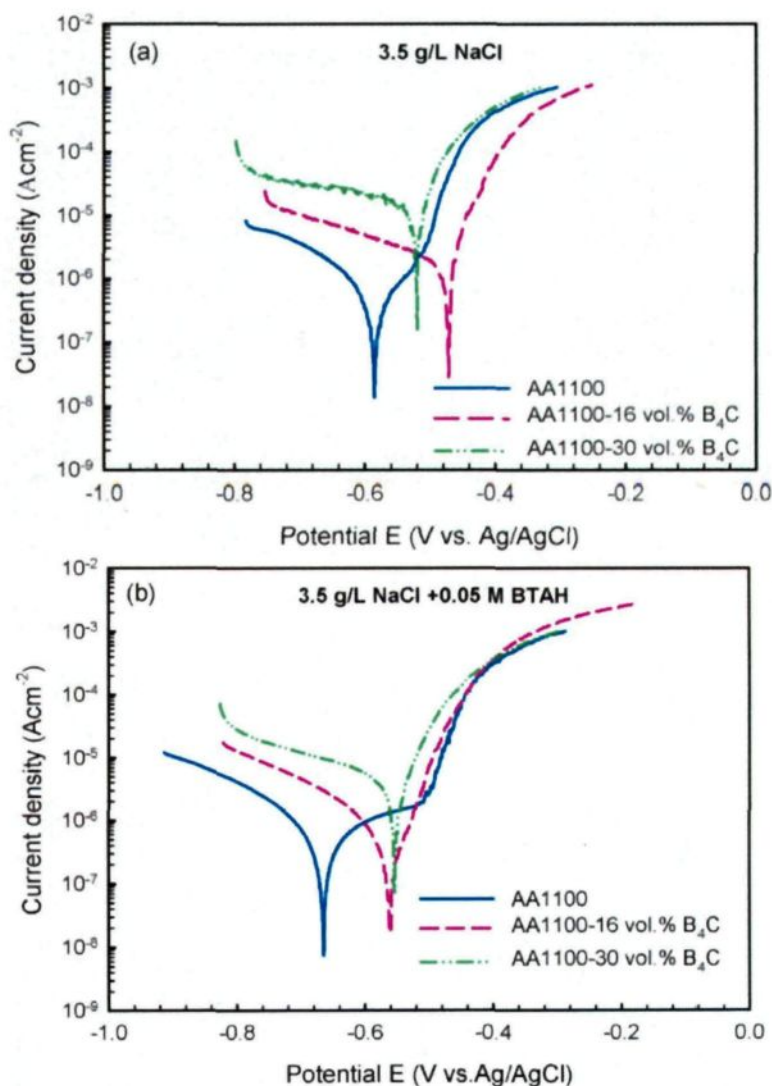


Figure 6.4 Potentiodynamic polarization curves of AA1100, AA1100-16 vol.% B<sub>4</sub>C and AA1100-30 vol.% B<sub>4</sub>C immersed in (a) 3.5 g/L NaCl and (b) 3.5 g/L NaCl +0.05M of BTAH solution for one hour.

Gathering these three inhibition efficiency values, it is found that the higher B<sub>4</sub>C volume fraction in the composite leads to the higher inhibition efficiency of BTAH. In addition and as illustrated in Figure 5, the relationship is linear. This result demonstrates

that although the number of corrosion-susceptible Al/B<sub>4</sub>C interfaces increases when the B<sub>4</sub>C volume fraction increases, these additional B<sub>4</sub>C particles play a positive role in the inhibition mechanism. Indeed, the higher the B<sub>4</sub>C volume fraction is, the higher the efficiency of BTAH is obtained, as it can be adsorbed on a higher number of B<sub>4</sub>C cathodic sites.

Table 6.3 Electrochemical parameters obtained from PDP measurements of AA1100, AA1100-16 vol.% B<sub>4</sub>C, and AA1100-30 vol.% B<sub>4</sub>C in a 3.5 g/L NaCl solution in the presence and absence of 0.05M of BTAH.

| Material<br>(% B <sub>4</sub> C) | 3.5 g/L NaCl                           |                    |  | 3.5 g/L NaCl + 0.05M<br>BTAH           |                    |  | IE<br>(%) |
|----------------------------------|--|--------------------|--|--|--------------------|--|-----------|
|                                  | $j_{corr}$<br>( $\mu\text{Acm}^{-2}$ ) | $E_{corr}$<br>(mV) | $R_p$<br>( $\text{k}\Omega\text{cm}^2$ ) | $j_{corr}$<br>( $\mu\text{Acm}^{-2}$ ) | $E_{corr}$<br>(mV) | $R_p$<br>( $\text{k}\Omega\text{cm}^2$ ) |           |
| 0                                | 0.76                                   | -584.6             | 42.0                                     | 0.49                                   | -665.3             | 55.8                                     | 29.0      |
| 16                               | 1.77                                   | -471.2             | 7.1                                      | 0.89                                   | -562.0             | 44.1                                     | 49.7      |
| 30                               | 16.46                                  | -519.4             | 1.1                                      | 4.66                                   | -554.8             | 5.25                                     | 71.7      |

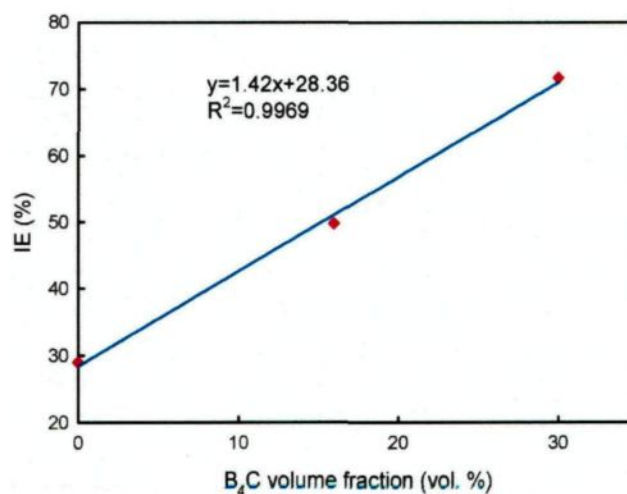


Figure 6.5 Plot showing the inhibition efficiency of 0.05 M of BTAH in a 3.5g/L NaCl solution as a function of the B<sub>4</sub>C particles volume fraction.

### 6.3.3 Effect of Immersion Time

Figure 6.6a and Figure 6.6b respectively present the polarization curves obtained in a NaCl solution without and with 0.05 M of BTAH after 1, 3, 18, 24, 72 and 120 hours of immersion. Electrochemical parameters derived from these curves are listed in Table 6.4 and in Table 6.5.

In the solution without BTAH, the  $j_{\text{corr}}$  increases gradually from 1.77 to 5.06  $\mu\text{Acm}^{-2}$  within the first 18 hours, then gradually decreases to 1.42  $\mu\text{A.cm}^{-2}$  as the time is prolonged to 120 hours. This decrease may be due to the passivation of the composite surface after a long immersion time. The  $E_b-E_{\text{corr}}$  values in this solution were found to increase slightly with the immersion time, indicating that a long immersion time results in a decrease in the pitting corrosion susceptibility of the composite and therefore reinforces the passivation hypothesis. Whilst in the solution with BTAH, the  $j_{\text{corr}}$  variation with time is contrary, *i.e.*  $j_{\text{corr}}$  decreases from 0.89 to 0.49  $\mu\text{A.cm}^{-2}$  in the first 18 hours due to the progressive adsorption of BTAH on the composite surface. Referring to the values obtained in the solution free of BTAH for the same 18-hour immersion time, the inhibition efficiency calculated was observed to increase from 49.3% to 90.3%. However, further extending the immersion time leads to an increase in the  $j_{\text{corr}}$  and consequently to a decrease in the inhibition efficiency. It is worthwhile mentioning that an inhibition efficiency of 40.1% was still obtained even after 120 hours of immersion in the solution, which suggests that BTAH is an efficient corrosion inhibitor for Al-B<sub>4</sub>C composites in the NaCl solution. The decrease in inhibition efficiency after 18 hours of immersion may be ascribed to the desorption of the BTAH species on the composite surface, which indicates that the BTAH species may

inhibit the corrosion of the composite in a 3.5 g/L NaCl solution through a physical adsorption process. [25]

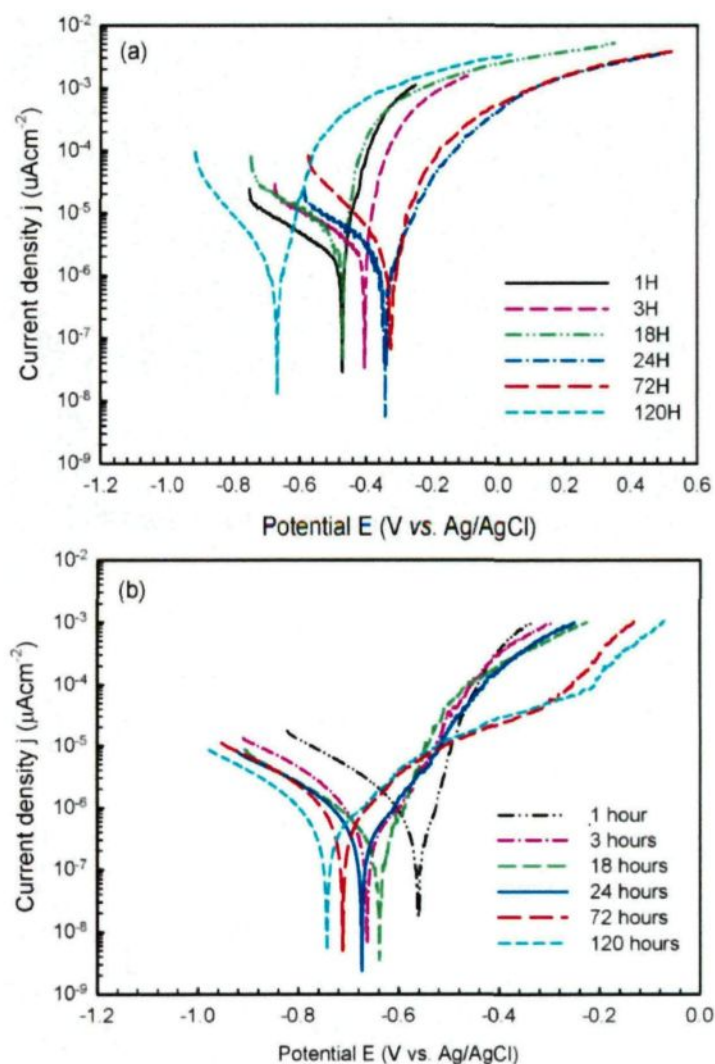


Figure 6.6 Potentiodynamic polarization curves of AA1100-16 vol.% B<sub>4</sub>C in (a) 3.5 g/L NaCl and (b) 3.5 g/L NaCl +0.05M of BTAH with different immersion times.

Interestingly, the  $E_b-E_{corr}$  values calculated in the solution with BTAH were found to increase with the immersion time and, as illustrated in Figure 6.7, the relationship between these parameters is linear. Comparing with the  $E_b-E_{corr}$  values obtained from the same immersion time in the solution free of BTAH, it is found that the  $E_b-E_{corr}$  increases

substantially after inhibition with BTAH, which means that the addition of BTAH to the solution decreases the pitting corrosion susceptibility of the composite to a great extent.

Table 6.4 Electrochemical parameters obtained from PDP measurement of AA1100-16 vol.% B<sub>4</sub>C in a 3.5 g/L NaCl solution with different immersion times.

| Immersion time<br>(hour) | $j_{\text{corr}}$<br>( $\mu\text{Acm}^{-2}$ ) | $E_{\text{corr}}$<br>(mV) | $E_{\text{b}}-E_{\text{corr}}$<br>(mV) | $R_{\text{p}}$<br>( $\text{k}\Omega\text{cm}^2$ ) |
|--------------------------|---|---------------------------|--|---|
| 1                        | 1.77  | -472.1                    | 11.1                                   | 7.1   |
| 3                        | 2.83  | -403.0                    | 13.4                                   | 3.9   |
| 18                       | 5.06  | -468.8                    | 24.1                                   | 3.12  |
| 24                       | 2.45  | -340.8                    | 32.6                                   | 23.1  |
| 72                       | 2.70  | -325.0                    | 33.2                                   | 12.9  |
| 120                      | 1.42  | -667.9                    | 45.3                                   | 17.8  |

Table 6.5 Electrochemical parameters obtained from PDP measurement of AA1100-16 vol.% B<sub>4</sub>C in a 3.5 g/L NaCl + 0.05M of BTAH solution with different immersion times.

| Immersion time<br>(hour) | $j_{\text{corr}}$<br>( $\mu\text{Acm}^{-2}$ ) | $E_{\text{corr}}$<br>(mV) | $E_{\text{b}}-E_{\text{corr}}$<br>(mV) | $R_{\text{p}}$<br>( $\text{k}\Omega\text{cm}^2$ ) | IE<br>(%) |
|--------------------------|---|---------------------------|--|---|-----------|
| 1                        | 0.89  | -562.0                    | 15.8                                   | 44.1  | 49.7      |
| 3                        | 0.63  | -662.5                    | 68.7                                   | 56.8  | 77.7      |
| 18                       | 0.49  | -638.8                    | 120.7                                  | 94.8  | 90.3      |
| 24                       | 0.61  | -674.0                    | 139.1                                  | 67.3  | 75.1      |
| 72                       | 0.75  | -710.9                    | 401.8                                  | 47.0  | 72.1      |
| 120                      | 0.85  | -743.3                    | 524.2                                  | 63.9  | 40.1      |

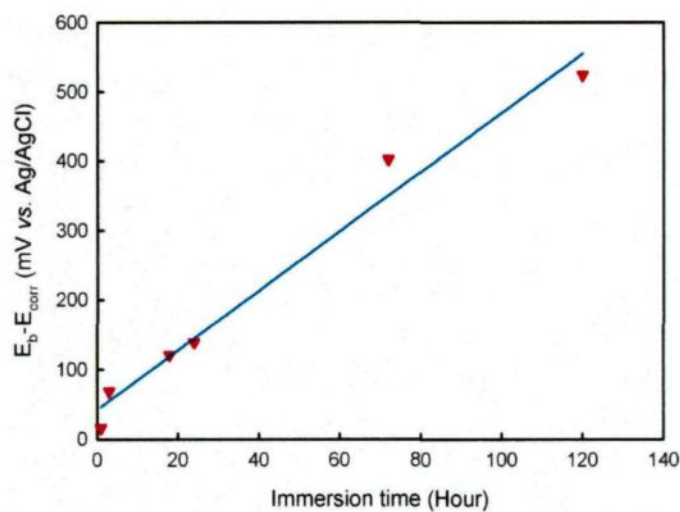


Figure 6.7 Plot showing that the  $E_b - E_{corr}$  obtained in the solution with BTAH has a linear relationship with the immersion times.

#### 6.3.4 Electrochemical Impedance Spectroscopy (EIS) Measurements

In order to gain more information concerning the corrosion inhibition phenomenon, electrochemical impedance spectroscopy measurements were carried out for the AA1100-16 vol.% B<sub>4</sub>C composite. Figure 6.8 presents Nyquist plots of AA1100-16 vol.% B<sub>4</sub>C in 3.5 g/L NaCl with different concentrations of BTAH.

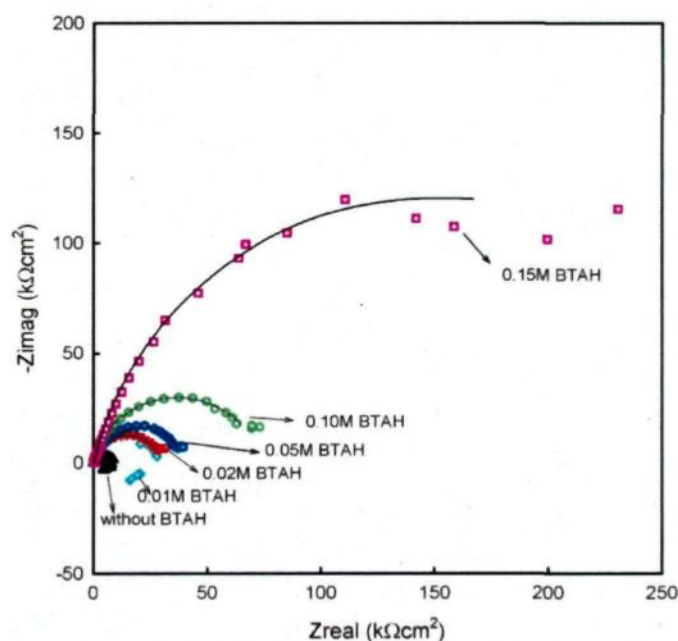


Figure 6.8 Nyquist plots of AA1100-16 vol.% B<sub>4</sub>C in 3.5 g/L NaCl with different concentrations of BTAH (experimental data and fitted curves are respectively presented by points and lines).

As can be seen from Figure 6.8, when the composite was immersed in a 3.5 g/L NaCl solution without or with very low concentrations of BTAH addition (*i.e.* 0.01 M), the Nyquist plot shows an inductive loop, indicating that the composite suffered pitting corrosion. When the added BTAH concentration reached 0.02 M or higher, the inductive loop was no longer observed, implying that no pitting occurred. Instead of the inductive loop, only a few low frequency data were recorded. These points, however, cannot be associated with a specific phenomenon due to the frequency limit (100 kHz ~ 0.01 Hz). Frequencies lower than 0.01 Hz were not used since the data acquisition time of the frequency response analyzer (FRA) would be very long, which would consequently have resulted in a significant dispersion of the impedance values.

In Figure 6.9, the Nyquist plot was interpreted with the equivalent circuit in by excluding the points at a low frequency. This approach, although not perfect, is expected to provide a good approximate to the experimental data fit and a representation of the physical reality. In this equivalent circuit,  $R_s$  is the solution resistance,  $R_{ct}$  is the charge transfer resistance at the solution/composite surface and CPE represents the constant phase element. Here, the CPE is substituted for the double layer capacitance  $C_{dl}$  to give a more accurate fit. Since in most cases the capacitive loops are depressed semicircles rather than the ideal semicircles due to their surface roughness, heterogeneities, anion adsorption, non-uniform potential, current profile, *etc.*<sup>[26]</sup>, Zoltowski<sup>[27]</sup> gave the CPE impedance as:

$$Z_{CPE} = \frac{1}{Q_a(j\omega)^\alpha}$$

$j = \sqrt{-1}$  and  $\omega$  was the angular frequency ( $\omega = 2\pi f$ ,  $f$  being the frequency). The double layer capacitance quantity (proportional to the active area) was  $Q_a$ , and  $\alpha$  was the CPE power with  $-1 \leq \alpha \leq 1$ . When  $\alpha = 1$ , the CPE represented a pure capacitance; when  $\alpha = 0$ , the CPE was considered as a pure resistance. When  $\alpha = -1$ , the CPE was regarded as a pure inductance. In this case, the CPE became an extremely flexible fitting parameter, but its physical significance and relationship with the distribution of time constants is not clear.

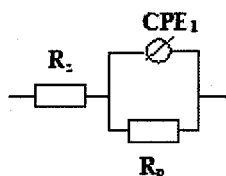


Figure 6.9 The equivalent circuit used to interpret the experimental data obtained in a 3.5 g/L solution in the presence of BTAH at different concentrations.

The impedance parameters derived from the Nyquist plots are listed in Table 6.6. It is observed that the values of solution resistance  $R_s$  and the polarization resistance  $R_p$  increase with the BTAH concentration. The CPE values decrease with the increasing BTAH concentration when the added  $C_{\text{BTAH}}$  is higher than 0.02 M, i.e., the concentration at which BTAH efficiently acts as a pitting corrosion inhibitor. These observations suggest that the BTAH species adsorb on the composite surface, consequently block the charge transfer process at the composite/solution interface, and therefore increase the polarization resistance. <sup>[28]</sup> The decrease in the CPE indicates that adsorption of the BTAH species at the composite surface increases the thickness of the electrical double layer by adding an extra layer of BTAH to the existing layer. It also decreases the local dielectric constant through the relative inactivity of an organic compound within an ionic and highly conductive double layer. <sup>[29, 30]</sup> The  $R_p$  values presently obtained are well agreeable with those obtained from the polarization results.

Table 6.6 Electrochemical parameters obtained from EIS measurements of Al composites in a 0.35 % NaCl solution with different BTAH concentrations.

| Solution                 | $R_s$<br>( $k\Omega\text{cm}^2$ ) | $R_p$<br>( $k\Omega\text{cm}^2$ ) | CPE<br>( $\mu\text{Fcm}^{-2}$ ) | $\alpha_1$ |
|--------------------------|-----------------------------------|-----------------------------------|---------------------------------|------------|
| 3.5 g/L NaCl             | 118.8                             | 10.0                              | 55.8                            | 0.66       |
| 3.5 g/L NaCl+0.01 M BTAH | 117.9                             | 30.0                              | 38.5                            | 0.85       |
| 3.5 g/L NaCl+0.02 M BTAH | 143.5                             | 30.1                              | 90.1                            | 0.89       |
| 3.5 g/L NaCl+0.05 M BTAH | 149.1                             | 40.1                              | 65.2                            | 0.87       |
| 3.5 g/L NaCl+0.10 M BTAH | 152.0                             | 73.6                              | 45.3                            | 0.87       |
| 3.5 g/L NaCl+0.15 M BTAH | 153.0                             | 301.2                             | 31.5                            | 0.88       |

### 6.3.5 Infrared Reflection Absorption Spectroscopy (IRRAS)

In order to evidence the presence of adsorbed BTAH species on the composite surface, the IRRAS technique was employed. When increasing the BTAH concentration in the solution, it was expected to observe the main absorption bands for BTAH at  $1208\text{ cm}^{-1}$  (C-H in-plane bending), and at  $775$ ,  $745$ ,  $739\text{ cm}^{-1}$  (all three related to C-H out-of-plane bending).<sup>[31]</sup> However, from the baseline corrected IR spectra shown in Figure 6.10, the  $1200$  to  $700\text{ cm}^{-1}$  spectral region shows major absorption interferences due to strong Al-OH stretching bands associated to bayerite  $\text{Al}(\text{OH})_3$ . Furthermore, according to the corrosion inhibition mechanism by BTAH evidenced in previous sections, the BTAH species would preferentially adsorb onto  $\text{B}_4\text{C}$  particles which are semi-conducting materials that do not respond well to the IRRAS effect. As a result, the C-H bending vibrations of BTAH were not specifically observed. Interestingly, the intensity of the broad IR absorption band centered at about  $3500\text{ cm}^{-1}$ , commonly assigned to the O-H stretching vibrations in bayerite  $\text{Al}(\text{OH})_3$ , was found to decrease when increasing the BTAH concentration.<sup>[32, 33]</sup> The peaks representing the Al-OH vibrations in the  $\sim 900$  and  $\sim 750\text{ cm}^{-1}$  range were also found to decrease in intensity as the BTAH concentration increased.<sup>[34, 35]</sup> Figure 6.11 illustrates that the  $\text{Al}(\text{OH})_3$  band area centered at  $3500\text{ cm}^{-1}$  decreases linearly when the calculated inhibition efficiency increases. This trend indicates that the addition of BTAH to the solution hinders the production of  $\text{Al}(\text{OH})_3$ , most likely by inhibiting the cathodic reaction that promotes aluminum dissolution and the consequent  $\text{Al}(\text{OH})_3$  formation. This result is also agreeable with the polarization and impedance results that provide direct

evidence of BTAH adsorption on the composite surface, thus preventing the aluminum matrix from excessive corrosion.

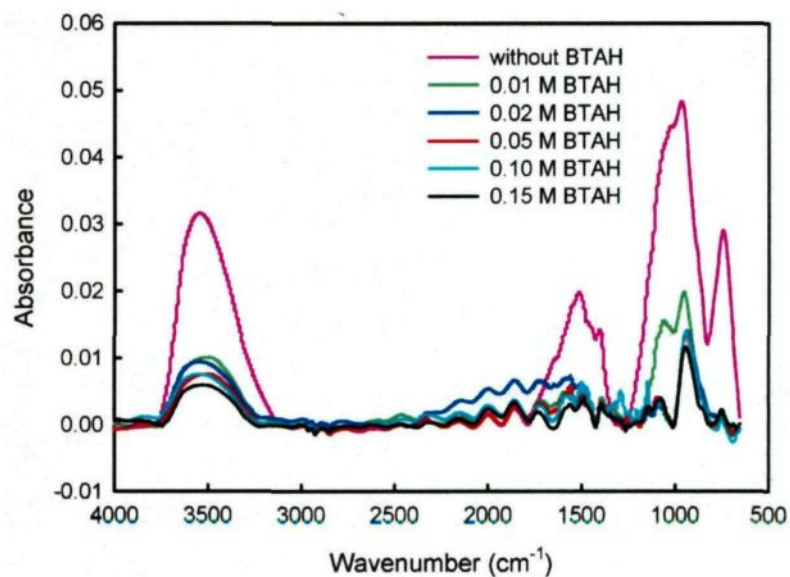


Figure 6.10 IRRAS spectra of AA1100-16 vol.% B<sub>4</sub>C MMCs obtained after immersion in a 3.5 g/L NaCl with different BTAH concentrations.

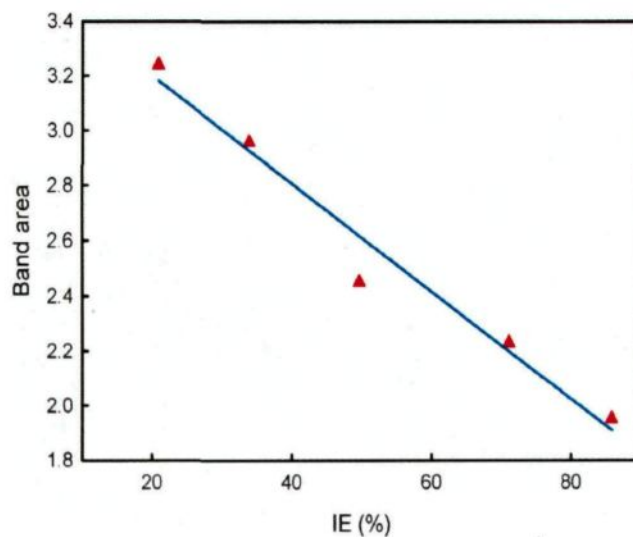


Figure 6.11 Band area of Al(OH)<sub>3</sub> centered at 3500 cm<sup>-1</sup> as a function of inhibition efficiency.

### 6.3.6 Adsorption Isotherm

The level of spontaneity associated to the Al-B<sub>4</sub>C corrosion inhibition by BTAH was investigated using adsorption isotherms. Surface coverage values ( $\theta$ ) calculated for the composite at various BTAH concentrations in a 3.5 g/L NaCl solution were derived from the potentiodynamic polarization results listed in Table 6.2. As presented in Figure 6.12, the Freundlich adsorption isotherm, previously employed to thermodynamically describe the corrosion inhibition phenomena, was found to accurately describe the BTAH adsorption behavior onto the Al-B<sub>4</sub>C composite. [22] According to this adsorption isotherm, the surface coverage by the BTAH ( $\theta$ ) is related to its equilibrium adsorption constant ( $K$ ) and concentration in solution ( $C$ ) by the following equation:

$$\theta = KC^n$$

where  $0 < n < 1$ . In logarithmic form, this equation can be rewritten as:

$$\log \theta = \log K + n \log C$$

This equation predicts that  $\log \theta$  vs.  $\log C$  yields to a linear relationship, as observed in Figure 6.12 ( $R^2 = 0.9929$ ).

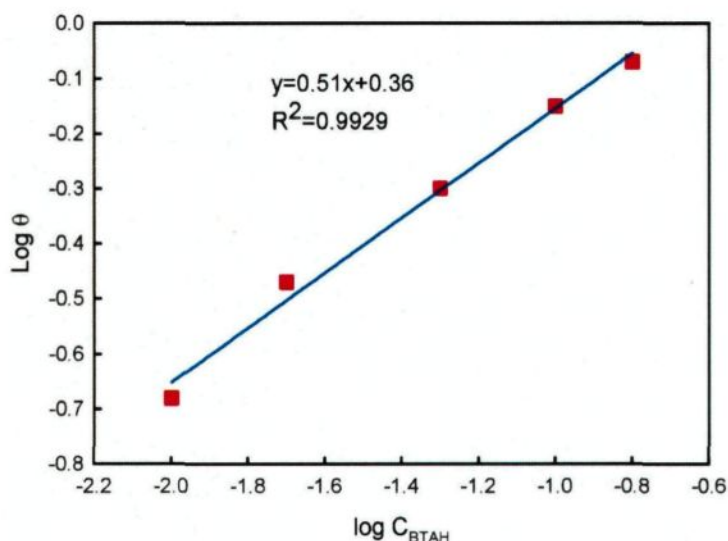


Figure 6.12 Plot of  $\log \theta$  vs  $\log C_{\text{BTAH}}$  (Freundlich adsorption isotherm) obtained from the BTAH surface coverage values presented in Table 6.2.

The free energy of adsorption for BTAH onto the composite surface ( $\Delta G_{\text{ads}}$ ,  $\text{kJ mol}^{-1}$ ) was calculated using the following equation: <sup>[36]</sup>

$$\Delta G_{\text{ads}} = -RT \ln \left[ \frac{55.5\theta}{C(1-\theta)} \right]$$

where  $C$  is the BTAH concentration (mol/L), 55.5 is the water concentration in the solution (mol/L),  $R$  is the gas constant ( $8.3145 \text{ J K}^{-1} \text{ mol}^{-1}$ ) and  $T$  is the absolute temperature (K). <sup>[37]</sup> Using the equation above, a free energy of adsorption of  $-18 \text{ kJ mol}^{-1}$  was calculated for the  $\text{BTAH}_{(\text{aq})}/\text{NaCl}_{(\text{aq})}/\text{Al-B}_4\text{C}$  system. The negative value suggests that BTAH spontaneously adsorbs onto the composite surface, <sup>[38]</sup> while the value  $\Delta G_{\text{ads}} > -40 \text{ kJ mol}^{-1}$  indicates that the BTAH species interact with the composite surface through a physisorption rather than chemisorption mechanism.

## 6.4 Conclusions

In the present study, benzotriazole was used for the first time to inhibit the corrosion of Al-B<sub>4</sub>C composites in a sodium chloride solution. Its corrosion inhibition effect as a function of BTAH concentration, volume fraction of B<sub>4</sub>C particles and immersion time was systematically investigated. According to the results obtained, the following conclusions could be drawn:

(1) Both polarization and impedance results show that BTAH is an efficient corrosion inhibitor for the Al-B<sub>4</sub>C composites in a 3.5g/L NaCl solution, and its inhibition efficiency increases with its concentration. This result is also evidenced by the IRRAS characterization of inhibited surface.

(2) The B<sub>4</sub>C particles play a positive role on the inhibition efficiency of benzotriazole for the composite in a NaCl solution. Increasing the B<sub>4</sub>C volume fraction in the composite results in a linear increase in the corrosion inhibition efficiency.

(3) The corrosion inhibition efficiency of benzotriazole on the AA1100-16 vol.% B<sub>4</sub>C composite in a NaCl solution is influenced by the immersion time. Within the first 18 hours, the inhibition efficiency increases progressively with the immersion time, attains the maximum value of 90.3%, and then gradually decreases to 40.1% with the immersion time prolonged to 120 hours.

(4) Benzotriazole is an inhibitor with a cathodic character and it inhibits the corrosion of the composite by adsorbing physically onto the B<sub>4</sub>C particles at the composite surface. The adsorption behavior obeys the Freundlich adsorption isotherm.

## References

- [1] X.-G. Chen, "Application of Al-B<sub>4</sub>C Metal Matrix Composites in the Nuclear Industry for Neutron Absorber Materials", in: *Proceedings of the Symposium on Solidification Processing of Metal Matrix Composites*, W.H. Hunt and N. Gupta (Eds.), TMS, 2006, pp. 343-350.
- [2] X.-G. Chen, R. Hark, "Development of Al-30%B<sub>4</sub>C Metal Matrix Composites for Neutron Absorber Material", in: *Proceedings of Aluminium Alloys: Fabrication, Characterization and Applications* W. Yin and S.K. Das (Eds.), TMS, 2008, pp. 3-9.
- [3] G. Bonnet, V. Rohr, X.-G. Chen, J.L. Bernier, R. Chiocca, H. Issard, "Use of Alcan's Al-B<sub>4</sub>C Metal Matrix Composites as Neutron Absorber Material in TN International's Transportation and Storage Casks", *Packaging, Transport, Storage and Security of Radioactive Material*, 20 (2009) 98-102.
- [4] Y. Han, D. Gallant, X.-G. Chen, "Corrosion Behavior of Al-B<sub>4</sub>C Metal Matrix Composites in H<sub>3</sub>BO<sub>3</sub>, K<sub>2</sub>SO<sub>4</sub> and NaCl Solutions", in: *Light Metal Proceedings*, M. Fafard and G. Dufour (Eds.), MetSoc, 2011, pp. 415-425.
- [5] Y. Han, D. Gallant, X.-G. Chen, "Investigation on Corrosion Behavior of the Al-B<sub>4</sub>C Metal Matrix Composite in a Mildly Oxidizing Aqueous Environment", *Corrosion*, 67 (2011) No. 115005.
- [6] S. Lin, H. Greene, H. Shih, F. Mansfeld, "Corrosion Protection of Al/SiC Metal Matrix Composites by Anodizing", *Corrosion*, 48 (1992) 61-67.
- [7] H.J. Greene, F. Mansfeld, "Corrosion Protection of Aluminum Metal-Matrix Composites", *Corrosion (Houston)*, 53 (1997) 920-927.
- [8] F. Mansfeld, S.L. Jeanjaquet, "The Evaluation of Corrosion Protection Measures for Metal Matrix Composites", *Corrosion Science*, 26 (1986) 727-734.
- [9] A.K. Mishra, R. Balasubramaniam, S. Tiwari, "Corrosion Inhibition of 6061-SiC by Rare Earth Chlorides", *Anti-Corrosion Methods and Materials*, 54 (2007) 37-46.
- [10] Z. Ahmad, B.J.A. Aleem, "The Effect of Inhibitors on the Susceptibility of Al 6013/SiC Interface to Localized Corrosion", *Journal of Materials Engineering and Performance*, 18 (2009) 129-136.
- [11] K.D. Ralston, S. Chrisanti, T.L. Young, R.G. Buchheit, "Corrosion Inhibition of Aluminum Alloy 2024-T3 by Aqueous Vanadium Species", *Journal of the Electrochemical Society*, 155 (2008) C350-C359.
- [12] G. Bereket, A. Pinarbaşı, "Electrochemical Thermodynamic and Kinetic Studies of the Behaviour of Aluminium in Hydrochloric Acid Containing Various Benzotriazole Derivatives", *Corrosion Engineering Science and Technology*, 39 (2004) 308-312.

- [13] V. Branzoi, F. Golgovici, F. Branzoi, "Aluminium Corrosion in Hydrochloric Acid Solutions and the Effect of Some Organic Inhibitors", *Materials Chemistry and Physics*, 78 (2003) 122-131.
- [14] Z. Grubač, R. Babić, M. Metikoš-Huković, "Application of Substituted N-arylpyrroles in the Corrosion Protection of Aluminium in Hydrochloric Acid", *Journal of Applied Electrochemistry*, 32 (2002) 431-438.
- [15] M. Abdallah, "Antibacterial Drugs As Corrosion Inhibitors For Corrosion of Aluminium in Hydrochloric Solution", *Corrosion Science*, 46 (2004) 1981-1996.
- [16] K.F. Khaled, M.M. Al-Qahtani, "The Inhibitive Effect of Some Tetrazole Derivatives Towards Al Corrosion in Acid Solution: Chemical, Electrochemical and Theoretical Studies", *Materials Chemistry and Physics*, 113 (2009) 150-158.
- [17] T. Kosec, I. Milošev, B. Pihlar, "Benzotriazole As An Inhibitor of Brass Corrosion in Chloride Solution", *Applied Surface Science*, 253 (2007) 8863-8873.
- [18] F.M. Bayoumi, A.M. Abdullah, B. Attia, "Kinetics of Corrosion Inhibition of Benzotriazole to Copper in 3.5% NaCl", *Materials and Corrosion*, 59 (2008) 691-696.
- [19] K. Babić-Samardžija, N. Hackerman, "Triazole, Benzotriazole and Substituted Benzotriazoles as Corrosion Inhibitors of Iron in Aerated Acidic Media", *Journal of Solid State Electrochemistry*, 9 (2005) 483-497.
- [20] J.L. Yao, B. Ren, Z.F. Huang, P.G. Cao, R.A. Gu, Z.Q. Tian, "Extending Surface Raman Spectroscopy to Transition Metals for Practical Applications IV. A Study on Corrosion Inhibition of Benzotriazole on Bare Fe Electrodes", *Electrochimica Acta*, 48 (2003) 1263-1271.
- [21] V. Palanivel, Y. Huang, W.J. Van Ooij, "Effects of Addition of Corrosion Inhibitors to Silane Films on the Performance of AA2024-T3 in a 0.5 M NaCl Solution", *Progress in Organic Coatings*, 53 (2005) 153-168.
- [22] G.M. Pinto, J. Nayak, A.N. Shetty, "Corrosion Inhibition of 6061 Al-15 vol. pct. SiC(p) Composite and its Base Alloy in a Mixture of Sulphuric Acid and Hydrochloric Acid by 4-(N,N-dimethyl amino) Benzaldehyde Thiosemicarbazone", *Materials Chemistry and Physics*, 125 (2011) 628-640.
- [23] W.H. Li, Q. He, S.T. Zhang, C.L. Pei, B.R. Hou, "Some New Triazole Derivatives as Inhibitors for Mild Steel Corrosion in Acidic Medium", *Journal of Applied Electrochemistry*, 38 (2008) 289-295.
- [24] R. Rosliza, W.B. Wan Nik, "Improvement of Corrosion Resistance of AA6061 Alloy by Tapioca Starch in Seawater", *Current Applied Physics*, 10 (2010) 221-229.
- [25] R.P.D. Kumari, J. Nayak, A.N. Shetty, "3-Methyl-4-Amino-5-Mercapto-1,2,4-Triazole as Corrosion Inhibitor for 6061 Al Alloy in 0.5 M Sodium Hydroxide Solution", *Journal of Coatings Technology Research*, 8 (2011) 685-695.

- [26] J.B. Jorcin, M.E. Orazem, N. Pébère, B. Tribollet, "CPE analysis by local electrochemical impedance spectroscopy", *Electrochimica Acta*, 51 (2006) 1473-1479.
- [27] P. Zoltowski, "On the Electrical Capacitance of Interfaces Exhibiting Constant Phase Element Behaviour", *Journal of Electroanalytical Chemistry*, 443 (1998) 149-154.
- [28] Z. Shahnavaaz, W.J. Basirun, S.M. Zain, "Aluminium Corrosion Inhibition Using Benzene-1,2,4,5-Tetracarboxylic Dianhydride (PMDH)", *Anti-Corrosion Methods and Materials*, 57 (2010) 21-27.
- [29] F. Bentiss, M. Lagrenee, M. Traisnel, J.C. Hornez, "The Corrosion Inhibition of Mild Steel in Acidic Media by a New Triazole Derivative", *Corrosion Science*, 41 (1999) 789-803.
- [30] A.K. Satpati, P.V. Ravindran, "Electrochemical Study of the Inhibition of Corrosion of Stainless Steel by 1,2,3-Benzotriazole in Acidic Media", *Materials Chemistry and Physics*, 109 (2008) 352-359.
- [31] K. Dokken, L.C. Davis, L.E. Erickson, S. Castro, "Fourier-Transform Infrared Spectroscopy as a Tool to Monitor Changes in Plant Structure in Response to Soil Contaminants", in: *Proceedings of the Conference on Application of Waste Remediation Technologies to Agricultural Contamination of Water Resources*, L.E. Erickson and J. Gulliford (Eds.), 2002, pp.
- [32] S.L. Nail, J.L. White, S.L. Hem, "Comparison of IR Spectroscopic Analysis and X-Ray Diffraction of Aluminum Hydroxide Gel", *Journal of Pharmaceutical Sciences*, 64 (1975) 1166-1169.
- [33] A. Violante, P.M. Huang, "Influence of Inorganic and Organic Ligands on the Formation of Aluminium Hydroxides and Oxyhydroxides", *Clays & Clay Minerals*, 33 (1985) 181-192.
- [34] R. Frost, J.T. Kloprogge, S.C. Russell, J. Sztetu, "Dehydroxylation of Aluminum (Oxo)hydroxides Using Infrared Emission Spectroscopy. Part II: Boehmite", *Applied Spectroscopy*, 53 (1999) 572-582.
- [35] A.C. Geiculescu, T.F. Strange, "A Microstructural Investigation of Low-Temperature Crystalline Alumina Films Grown on Aluminum", *Thin Solid Films*, 426 (2003) 160-171.
- [36] F. Altaf, R. Qureshi, S. Ahmed, "Surface Protection of Copper by Azoles in Borate Buffers-Voltammetric and Impedance Analysis", *Journal of Electroanalytical Chemistry*, 659 (2011) 134-142.
- [37] D.M. Bastidas, P.P. Gómez, E. Cano, "The Isotherm Slope. A Criterion for Studying the Adsorption Mechanism of Benzotriazole on Copper in Sulphuric Acid", *Revista de Metalurgia (Madrid)*, 41 (2005) 98-106.

- [38] E. Cano, J.L. Polo, A. Laglesia, J.M. Bastidas, "A Study on the Adsorption of Benzotriazole on Copper in Hydrochloric Acid Using the Inflection Point of the Isotherm", *Adsorption*, 10 (2004) 219-225.

## **CHAPTER 7**

### **GALVANIC CORROSION ASSOCIATED WITH Al-B<sub>4</sub>C COMPOSITES/SS304 AND Al-B<sub>4</sub>C COMPOSITES/AA6061 COUPLES IN NaCl AND H<sub>3</sub>BO<sub>3</sub> SOLUTIONS**

## CHAPTER 7

### GALVANIC CORROSION ASSOCIATED WITH Al-B<sub>4</sub>C COMPOSITES/SS304 AND Al-B<sub>4</sub>C COMPOSITES/AA6061 COUPLES IN NaCl AND H<sub>3</sub>BO<sub>3</sub> SOLUTIONS

#### Abstract

As neutron absorber materials used in the nuclear industry, Al-B<sub>4</sub>C composites are often assembled to structural materials AA6061 or SS304, thus making galvanic corrosion likely to occur, especially in the wet storage application. The present study investigates the galvanic corrosion behavior that may occur between Al-B<sub>4</sub>C composites and AA6061 or SS304 in NaCl and H<sub>3</sub>BO<sub>3</sub> solutions using a zero resistance ammeter (ZRA). Effects of dissimilar materials (*e.g.*, B<sub>4</sub>C content), immersion solution, and area ratio of the coupled materials are reported. In NaCl solution, whether it is coupled to SS304 or AA6061, the composite or base alloy always acts as an anode and galvanic currents measured are directly proportional to the cathode area. On the other hand, in H<sub>3</sub>BO<sub>3</sub> solution, composites preferentially dissolve when they are coupled to SS304, while AA6061 galvanically protects metal matrix composites from dissolution. Although galvanic corrosion is controlled by oxygen diffusion at the cathode in both NaCl and H<sub>3</sub>BO<sub>3</sub> solutions, its intensity is appreciably smaller in H<sub>3</sub>BO<sub>3</sub> solution than in NaCl solution. The B<sub>4</sub>C content

is also found to play a key role in galvanic corrosion, its influence being modulated by the solution composition and materials to which the composite is galvanically coupled.

## 7.1 Introduction

Al-B<sub>4</sub>C metal matrix composites (MMCs) have received considerable attention due to their light weight, superior thermal conductivity, high stiffness and hardness. <sup>[1]</sup> They are also very attractive since they can incorporate high concentrations of B<sub>4</sub>C particles and still have a good formability for the extrusion and rolling manufacturing processes. Owing to the special capturing neutron ability of isotope B<sup>10</sup>, Al-B<sub>4</sub>C MMCs have been increasingly used as excellent neutron absorber materials to fabricate the inside basket of transport and storage casks for spent nuclear fuels in the nuclear industry. <sup>[2, 3]</sup>

However, AA1100-B<sub>4</sub>C MMCs have recently been reported to be less corrosion resistant than their base Al alloys, and the corrosion resistance was found to be decreased with increased B<sub>4</sub>C particle volume fraction. <sup>[4]</sup> This behavior was attributed to the fact that B<sub>4</sub>C particles in aluminum matrix break the continuity of the protective aluminum oxide film, and thus increase the number of potential sites where corrosion could be initiated. Besides, some reaction-induced intermetallic phases such as TiB<sub>2</sub>, Al<sub>3</sub>BC and AlB<sub>2</sub> around Al/B<sub>4</sub>C interfaces <sup>[5, 6]</sup> may preferentially allow the oxygen reduction reaction to take place, leading to a local increase in pH in the vicinity B<sub>4</sub>C particles, which promotes dissolution of Al matrix. In addition, B<sub>4</sub>C particles can form galvanic couples with the Al matrix, and these galvanic couples accelerate the dissolution of the matrix, especially in the vicinity of particles. <sup>[7]</sup>

As non-structural neutron absorber materials gaining popularity in the nuclear industry, AA1100-B<sub>4</sub>C MMCs are often assembled to structural materials AA6061 aluminum alloy or SS304 stainless steel. Consequently, AA1100-B<sub>4</sub>C MMCs may become galvanically coupled to AA6061 or SS304, which potentially accelerates the corrosion of the less noble material. Such galvanic corrosion phenomenon is especially at risk when assemblies are used in the wet storage of spent nuclear fuels that implies immersion in a mildly corrosive reactor pool water containing boric acid with B concentration of ~ 2500 ppm. However, there is no study that highlights galvanic corrosion processes that characterize AA1100-B<sub>4</sub>C MMCs/SS304 and AA1100-B<sub>4</sub>C MMCs/AA6061 couples immersed in a boric acid solution. Therefore, this paper aims at investigating the galvanic corrosion behavior of AA1100-B<sub>4</sub>C MMCs containing different B<sub>4</sub>C levels (16 and 30 vol.%) and coupled to AA6061 or SS304 in a 2500 ppm boron-containing H<sub>3</sub>BO<sub>3</sub> and common 3.5% NaCl solutions, considering the effect of dissimilar materials and area ratios of coupled materials.

## **7.2 Experimental Procedure**

### **7.2.1 Sample Preparation**

Materials investigated are AA1100-B<sub>4</sub>C metal matrix composites with 16 and 30 vol.% B<sub>4</sub>C particles as well as the AA1100 base alloy in the form of rolled sheets, supplied by Rio Tinto Alcan (Saguenay, Quebec, Canada). The designate chemical composition of the base alloy is listed in Table 7.1. During the galvanic coupling tests, the investigated materials are coupled to AA6061 or SS304. Prior to immersion, all aluminum-based

specimens were sanded with 3M Scotch-Brite™ MMM69412 surface conditioning disc (5 inches in diameter, extra-fine surface finish), then degreased with acetone and rinsed with deionized water. Finally, all specimens were dried with clean compressed air. SS304 material was simply acetone degreased.

Table 7.1 Chemical composition of the base alloy AA1100.

| Elements            | Al          | Cu           | Mn           | Si+Fe       | Zn          | other       |
|---------------------|-------------|--------------|--------------|-------------|-------------|-------------|
| Composition (wt. %) | $\geq 99.0$ | 0.050 - 0.20 | $\leq 0.050$ | $\leq 0.95$ | $\leq 0.10$ | $\leq 0.15$ |

### 7.2.2 Galvanic Coupling Measurement

Galvanic corrosion measurements were performed in 3.5% NaCl and 2500 ppm B-containing  $H_3BO_3$  solutions at ambient temperature (around 21°C) and in open to air conditions. Samples were exposed to the solution in a 300 cm<sup>3</sup> - EG&G PAR flat cell (London Scientific, London, ON, Canada). For corrosion data acquisition, a Reference 600 instrument potentiostat was used in the zero resistance ammeter (ZRA) mode (Gamry Instruments, Warminster, PA, USA). Variations in galvanic current  $I_g$  and galvanic potential  $\phi_g$  were recorded continuously for 24 hours. In the galvanic corrosion test, investigated materials (AA1100 base alloy or AA1100-B<sub>4</sub>C composites) are used as working electrode #1 (W1), and AA6061 or SS304 as working electrode #2 (W2). Using this convention, a positive galvanic current means that working electrode #1 preferentially corrodes, while a negative current indicates the preferential dissolution of working electrode #2. In addition, the open circuit potential ( $\phi_{ocp}$ ) of uncoupled materials was measured in 3.5% NaCl and 2500 ppm B-containing  $H_3BO_3$  solutions. Stable  $\phi_{ocp}$  were

obtained when uncoupled materials were immersed for 1 hour in NaCl solution and for 3 hours in H<sub>3</sub>BO<sub>3</sub> solution. The potential differences  $\Delta\phi^S$  reported in this paper are calculated as  $\Delta\phi^S = \phi_{ocp}^{W1} - \phi_{ocp}^{W2}$ . The exposure area of the sample is 1 cm<sup>2</sup>, except where otherwise stated. All potentials measured are referred to the Ag/AgCl reference electrode. Magnetic stirring was employed at the cell bottom to increase mass transfer at the electrodes surface.

### 7.3 Results and Discussion

#### 7.3.1 Open Circuit Potentials of Uncoupled Materials

Table 7.2 lists the open circuit potential of uncoupled materials. It is observed that for a same aluminum-based material, the open circuit potential measured in H<sub>3</sub>BO<sub>3</sub> solution is nobler than that determined in the NaCl solution, indicating that aluminum materials are less active in H<sub>3</sub>BO<sub>3</sub> solution than in NaCl solution. For composites immersed in the H<sub>3</sub>BO<sub>3</sub> solution, the open circuit potential remarkably shifts in the noble direction with increasing B<sub>4</sub>C volume percent. This shift can be explained by the mixed potential theory, B<sub>4</sub>C particles being cathodic to the aluminum matrix. [8] In the aggressive NaCl solution, addition of B<sub>4</sub>C to the AA1100 alloy also makes nobler the open circuit potential, as predicted by the mixed potential theory. However, due to the aggressive character of the NaCl solution that promotes Al-B<sub>4</sub>C galvanic coupling within the MMC, the composite becomes more active with B<sub>4</sub>C content increasing in the composite, explaining why a more negative  $\phi_{ocp}$  value is measured for the 30 vol.% B<sub>4</sub>C composite. For the SS304 stainless

steel material, regardless of the solution,  $\varphi_{ocp}$  values measured are all anodic to those reported for aluminum materials. Finally, AA6061 alloy is characterized by an open circuit potential similar to that of AA1100 alloy in the boric acid solution, while AA1100 alloy has a more negative open circuit potential than AA6061 alloy in the NaCl solution.

Table 7.2 Open circuit potential ( $\varphi_{ocp}$ ) of materials investigated in 3.5% NaCl and 2500 ppm B-containing  $H_3BO_3$  solutions.

| Materials              | $\varphi_{ocp}$ (mV vs. Ag/AgCl) |                      |
|------------------------|----------------------------------|----------------------|
|                        | 3.5% NaCl                        | 2500 ppm B $H_3BO_3$ |
| AA1100                 | -665                             | -457                 |
| AA1100-16 vol.% $B_4C$ | -570                             | -337                 |
| AA1100-30 vol.% $B_4C$ | -613                             | -26                  |
| SS304                  | 62                               | 200                  |
| AA6061                 | -607                             | -488                 |

As generally recognized, the potential difference ( $\Delta\varphi^s$ ) between two materials electrically coupled in an electrolyte is considered to be the driving force of the galvanic corrosion.<sup>[9]</sup> Hence, the parameter  $\Delta\varphi^s$  is often used to estimate the extent of corrosion that may result from the galvanic coupling of these two materials,<sup>[10, 11]</sup> although this thermodynamic quantity does not take into account surface phenomena that could limit the corrosion reaction rate. According to open circuit potential values of uncoupled dissimilar materials listed in Table 7.2. In both solutions, SS304 is expected to act as a cathode when it is coupled to the composite or the base alloy. Its acceleration effect on the corrosion should be:

In  $H_3BO_3$  solution:

AA1100/SS304 > AA1100-16 vol.% B<sub>4</sub>C/SS304 > AA1100-30 vol.% B<sub>4</sub>C/SS304

In NaCl solution:

AA1100/SS304 > AA1100-30 vol.% B<sub>4</sub>C/SS304 > AA1100-16 vol.% B<sub>4</sub>C/SS304.

When the investigated material is coupled to AA6061, AA6061 is expected to act as a cathode or an anode, depending on the potential difference polarity:

In H<sub>3</sub>BO<sub>3</sub> solution:

AA6061 always acts as the anode regardless of materials it is coupled to.

In NaCl solution:

AA6061 acts as the cathode when it is coupled to AA1100 or AA1100-30 vol.% B<sub>4</sub>C.

AA6061 acts as the anode when it is coupled to AA1100-16 vol.% B<sub>4</sub>C.

### 7.3.2 Effect of Dissimilar Materials

Typical time behavior of galvanic current ( $I_g$ ) for AA1100/SS304 and AA1100/AA6061 couples in 3.5% NaCl solutions are shown in Figure 7.1. For both couples, it is observed that  $I_g$  values are positive, which means, by convention, that the base alloy AA1100 acts as an anode and preferentially dissolves. This result is as predicted by the open circuit potential values listed in Table 7.2. The average galvanic current  $\bar{I}_g$  measured when AA1100 is coupled to SS304 is 31.4  $\mu\text{A}$ , which is more than one order of magnitude greater than when it is coupled to AA6061 (2.1  $\mu\text{A}$ ). For the AA1100/SS304 couple,  $I_g$  decreases substantially from 180 to 20  $\mu\text{A}$  during the first 12 hours and then

remains virtually constant. On the other hand, when AA1100 is coupled to AA6061 alloy, the galvanic current abruptly increases from less than  $0.001 \mu\text{A}$  to a current range of  $0.5 \sim 1.0 \mu\text{A}$ , where it also stabilizes after 12 hours of immersion. In this case, the initial increase in galvanic current was reported to be related to the roughening of the sample surface caused by corrosion. [12]

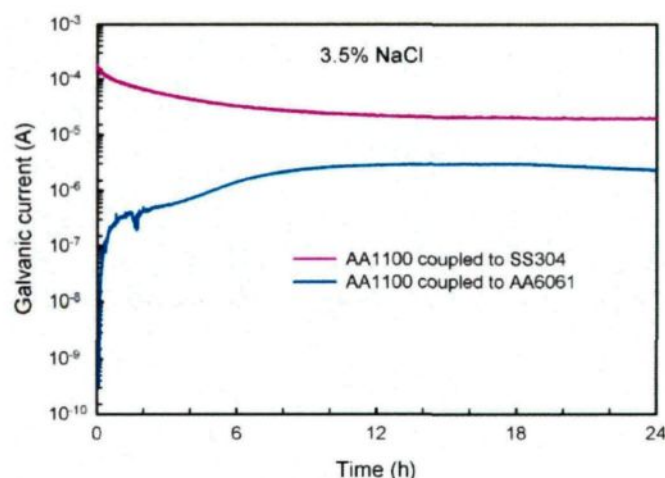


Figure 7.1 Time behavior of galvanic current  $I_g$  for AA1100 coupled to SS304 and AA6061 in 3.5% NaCl.

Figure 7.2 and Figure 7.3 present time behavior of galvanic currents recorded for AA1100-16 vol.%  $\text{B}_4\text{C}$  and AA1100-30 vol.%  $\text{B}_4\text{C}$  composites, respectively, coupled to SS304 and AA6061 in a 3.5% NaCl solution. Similarly to the AA1100/SS304 and AA1100/AA6061 couples, the galvanic activity is more intense in couples containing SS304. However, in the presence of Al- $\text{B}_4\text{C}$  materials, the galvanic activity does not tend to stabilize over time, as it was observed with  $\text{B}_4\text{C}$ -free AA1100 material. Indeed, for couples involving SS304,  $I_g$  slowly decreases with time. For composites coupled to AA6061, a maximum  $I_g$  value is rapidly obtained after 6 hours, and  $I_g$  importantly decreases thereafter. Interestingly, Figure 7.2 and Figure 7.3 present oscillations of the galvanic

currents that can be attributed to competitive passivation and pitting processes, the latter being encouraged by the presence of  $B_4C$  particles. <sup>[10]</sup>

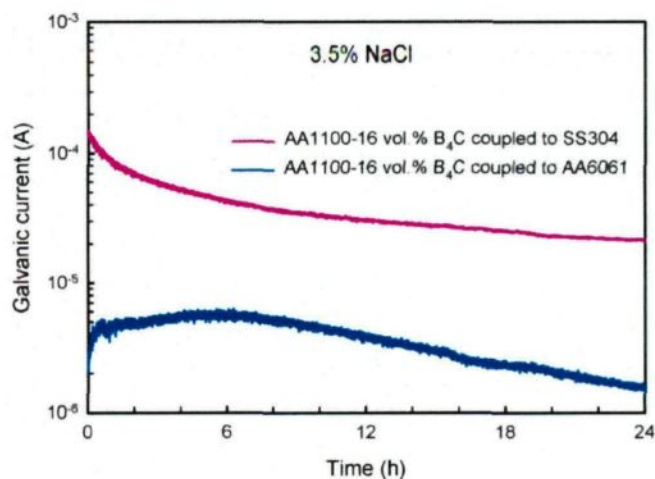


Figure 7.2 Time behavior of galvanic current  $I_g$  for AA1100-16 vol.%  $B_4C$  coupled to SS304 and AA6061 in 3.5% NaCl.

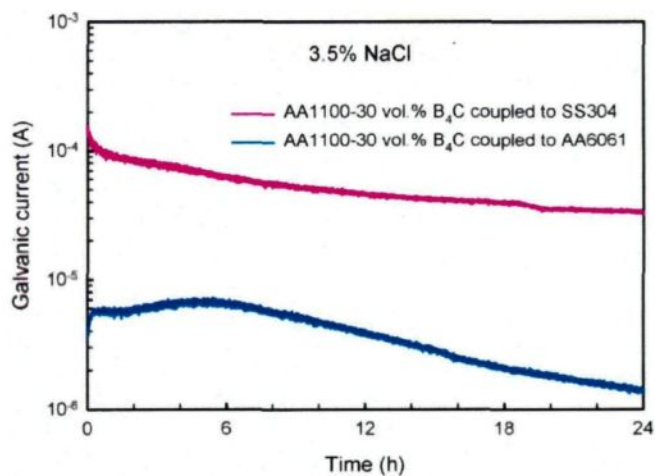


Figure 7.3 Time behavior of galvanic current  $I_g$  for AA1100-30 vol. %  $B_4C$  coupled to SS304 and AA6061 in 3.5% NaCl.

The average galvanic currents  $\overline{I_g}$  associated to couples investigated in NaCl solution are listed in Table 7.3. It is observed that  $\overline{I_g}$  increases with increasing  $B_4C$  vol.% when the composite are coupled to SS304 or AA6061 in NaCl solution. Indeed,  $\overline{I_g}$  progressively

increases from 31.4 to 52.8  $\mu\text{A}$  when the composite is coupled to SS304, and also increases, but to a less extent (from 2.1 to 4.0  $\mu\text{A}$ ) when the composite is coupled to AA6061. Concerning the relationship between galvanic currents recorded and corrosion potential differences previously calculated, results reported in Table 7.3 globally show that large  $\Delta\phi^s$  values assigned to SS304-containing couples are related to high  $\bar{I}_g$ , although there is no linear trend between the two parameters. For AA6061 coupled to AA1100-16 vol.% B<sub>4</sub>C and AA1100-30 vol.%B<sub>4</sub>C, corrosion potential differences are very low, as well as average galvanic currents recorded. On the basis of individual corrosion potentials measured, it was first considered that AA6061 should be the anode when coupled to AA1100-16 vol.% B<sub>4</sub>C (by only 37 mV). However, galvanic tests results show that AA6061 is the cathode, which can be explained by a fast change in polarity due to a polarization effect at the very beginning of the immersion. As presented in the next section, cathode-to-anode inversions have frequently been observed in boric acid solution.

Table 7.3 Average galvanic current  $\bar{I}_g$  of different couples and potential difference  $\Delta\phi^s$  of uncoupled dissimilar material in 3.5% NaCl solution.

| Couples                                | $\bar{I}_g$ ( $\mu\text{A}$ ) | $\Delta\phi^s$ (mV) |
|--|-------------------------------|---------------------|
| AA1100/SS304                           | 31.4                          | -727                |
| AA1100-16 vol.%B <sub>4</sub> C/SS304  | 38.1                          | -632                |
| AA1100-30 vol.%B <sub>4</sub> C/SS304  | 52.8                          | -675                |
| AA1100/AA6061                          | 2.1                           | -58                 |
| AA1100-16 vol.%B <sub>4</sub> C/AA6061 | 3.7                           | 37                  |
| AA1100-30 vol.%B <sub>4</sub> C/AA6061 | 4.0                           | -6                  |

### 7.3.3 Effect of Solution

Results presented in the previous section were obtained in a 3.5% NaCl, which is a common solution typically used in studying the galvanic corrosion of aluminum-based composites. However, in the wet storage of spent nuclear fuels, AA1100-B<sub>4</sub>C composites and structural materials are immersed in circulating 2500 ppm boron-containing boric acid. Therefore, it becomes of significance to study the galvanic corrosion between AA1100-B<sub>4</sub>C composites and AA6061 or SS304 in boric acid solution.

Figure 7.4, Figure 7.5 and Figure 7.6 show typical galvanic currents recorded over time for AA1100, AA1100-16 vol.%B<sub>4</sub>C and AA1100-30 vol.% B<sub>4</sub>C composites coupled to AA6061 and SS304 in a 2500 ppm B-containing H<sub>3</sub>BO<sub>3</sub> solution, respectively. Results obtained in H<sub>3</sub>BO<sub>3</sub> solution are clearly different from those obtained in 3.5% NaCl solution. In NaCl solution, galvanic currents are high and, in all cases, the base alloy AA1100 and its composites (16 or 30 vol.% B<sub>4</sub>C) are the anode ( $I_g > 0$ ). In H<sub>3</sub>BO<sub>3</sub> solution, galvanic currents are negligibly low and the investigated materials (W1, AA1100 or AA1100-B<sub>4</sub>C composites) act as anode or cathode, depending on the coupling condition. As an example, for the couple AA1100/SS304, the galvanic current after a 24-hour immersion is of 1.5  $\mu$ A in H<sub>3</sub>BO<sub>3</sub> solution, while it is of 20  $\mu$ A in NaCl solution. In H<sub>3</sub>BO<sub>3</sub> solution, a sudden drop in the galvanic current was observed at the beginning of the test when investigated materials are coupled to SS304. Interestingly, this drop is found to correspond to an increase in the galvanic potential presented in Figure 7.7, which indicates that a passive layer forms on the composite surface during this period in H<sub>3</sub>BO<sub>3</sub> solution. The following

increase in galvanic current is found to be associated with the progressive decrease of the galvanic potential, implying that the passive layer formed on the composite surface gradually dissolves. <sup>[10]</sup> Finally, no galvanic current oscillation is observed in  $H_3BO_3$ , which means, as shown in Figure 7.8, that pitting does not occur in this solution while pits develop in NaCl solution.

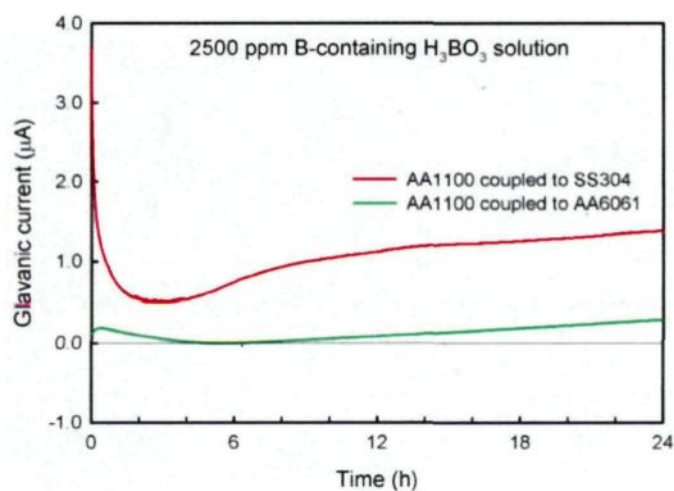


Figure 7.4 Time behavior of galvanic current  $I_g$  for AA1100 coupled to SS304 and AA6061 in 2500 ppm B-containing  $H_3BO_3$ .

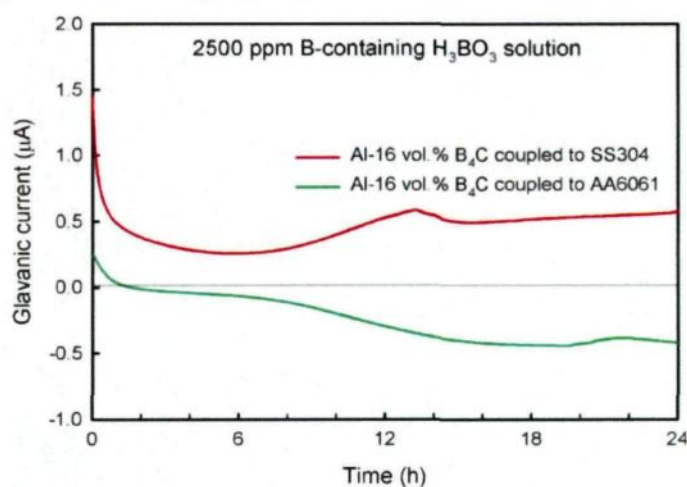


Figure 7.5 Time behavior of galvanic current  $I_g$  for AA1100-16 vol. %  $B_4C$  coupled to SS304 and AA6061 in 2500 ppm B-containing  $H_3BO_3$ .

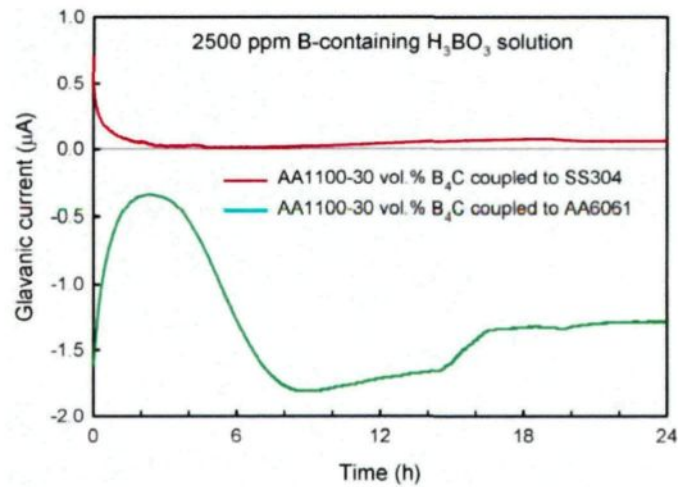


Figure 7.6 Time behavior of galvanic current  $I_g$  for AA1100-30 vol.%  $B_4C$  coupled to SS304 and AA6061 in 2500 ppm B-containing  $H_3BO_3$ .

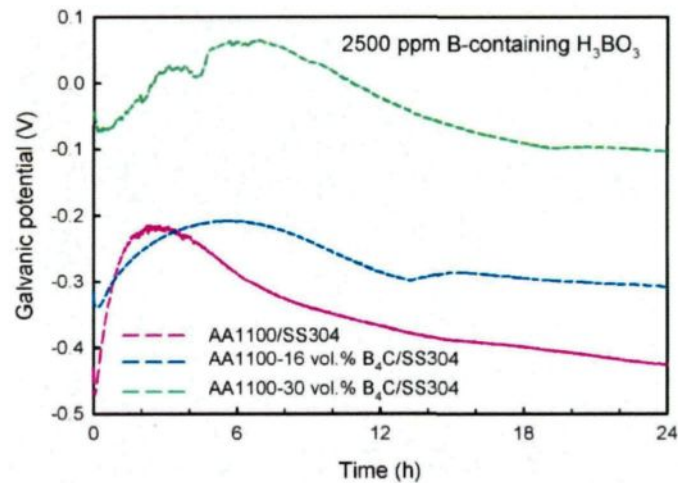


Figure 7.7 Time behavior of galvanic potential for AA1100, AA1100-16 vol.%  $B_4C$  and AA1100-30 vol.%  $B_4C$  composites coupled to SS304 in 2500 ppm B-containing  $H_3BO_3$  solution.

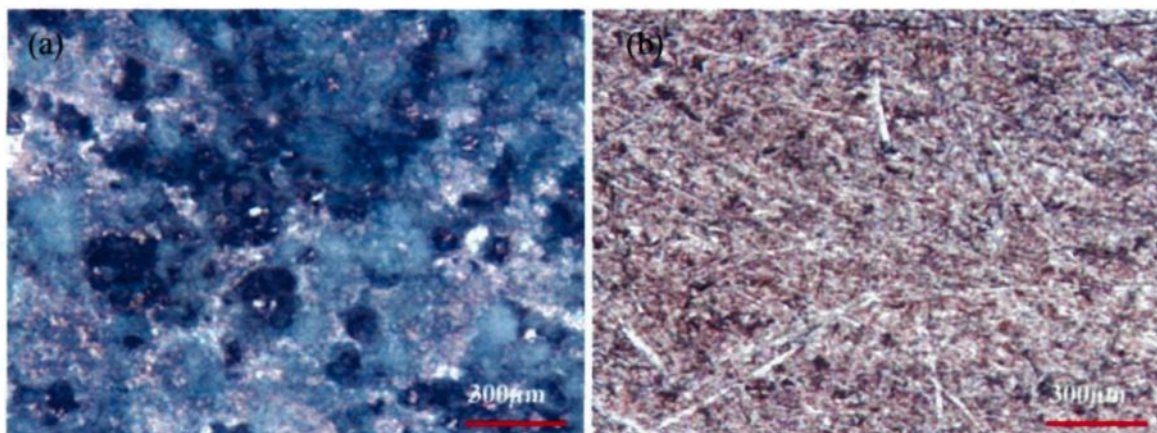


Figure 7.8 Surface morphology of the AA1100-16 vol.% B<sub>4</sub>C composite coupled to SS304 after 24 h immersion in (a) 3.5% NaCl and (b) 2500 ppm B-containing H<sub>3</sub>BO<sub>3</sub> solution (100×).

Table 7.4 lists potential differences ( $\Delta\phi^S$ ) of uncoupled dissimilar materials in the H<sub>3</sub>BO<sub>3</sub> solution as well as average galvanic currents ( $\bar{I}_g$ ) for the different galvanic couples presented in Figure 7.4, Figure 7.5 and Figure 7.6. Unlike in NaCl solution, both  $\bar{I}_g$  and  $\Delta\phi^S$  decrease with increasing B<sub>4</sub>C vol.% in the composite when investigated materials are coupled to SS304. Indeed,  $\bar{I}_g$  decreases from 1.04 to 0.05  $\mu\text{A}$  and  $\Delta\phi^S$  decreases from -657 to -226 mV with B<sub>4</sub>C content increasing from 0 to 30% volume fraction. On the basis of mixed potential theory, increasing B<sub>4</sub>C content in the composite results in the shift of potential in positive direction, which consequently decreases the potential difference between composite and SS304. As a result, a decrease in average galvanic current is measured. When investigated materials are coupled to AA6061, the absolute value of  $\bar{I}_g$  is found to increase with increasing potential difference. As presented in Figure 7.5 and Figure 7.6,  $\bar{I}_g$  is negative for AA1100-16 vol.% B<sub>4</sub>C/AA6061 and AA1100-30 vol.% B<sub>4</sub>C/AA6061 couples, which indicates that the MMC composite acts as a cathode in

these couples and the measured current is related to the dissolution of AA6061, as expected from open circuit potential measurements presented in Section 7.3.1. As reported in previous studies, <sup>[7, 13]</sup> B<sub>4</sub>C particles are of cathodic character with respect to the base alloy AA1100. Therefore, for the two couples with negative galvanic currents, increasing B<sub>4</sub>C volume fraction in the composite means increasing the effective cathodic area. Consequently, as long as the reaction is under cathodic control, this increase in MMC B<sub>4</sub>C content leads to an increase in the dissolution current of anode (AA6061). The effect of cathode/anode area ratio will be discussed in detail in the following section.

Table 7.4 Average galvanic current  $\overline{I}_g$  of different couples and potential difference  $\Delta\phi^s$  of uncoupled dissimilar materials in 2500 ppm B-containing H<sub>3</sub>BO<sub>3</sub> solution.

| Couples                                | $\overline{I}_g$ ( $\mu\text{A}$ ) | $\Delta\phi^s$ (mV) |
|--|------------------------------------|---------------------|
| AA1100/SS304                           | 1.04                               | -657                |
| AA1100-16 vol.%B <sub>4</sub> C/SS304  | 0.45                               | -537                |
| AA1100-30 vol.%B <sub>4</sub> C/SS304  | 0.05                               | -226                |
| AA1100/AA6061                          | 0.12                               | 31                  |
| AA1100-16 vol.%B <sub>4</sub> C/AA6061 | -0.25                              | 151                 |
| AA1100-30 vol.%B <sub>4</sub> C/AA6061 | -1.30                              | 462                 |

Results listed in Table 7.4, which presents  $\overline{I}_g$  and  $\Delta\phi^s$  measured in H<sub>3</sub>BO<sub>3</sub> solution, are illustrated in Figure 7.9. Regardless of the materials coupled, it is observed that  $\overline{I}_g$  varies almost linearly with  $\Delta\phi^s$  parameter calculated for the combination. However, such a trend is unlikely in NaCl solution. Indeed, in NaCl solution, galvanic corrosion occurring between AA1100 matrix and B<sub>4</sub>C particles (within the MMC material) importantly influences the galvanic coupling between the MMC and AA6061 or SS304. As a

consequence, the higher the  $B_4C$  content is, the higher the galvanic corrosion is measured between the MMC and SS304. Since  $H_3BO_3$  solution is a non aggressive and weak acid ( $K_a = 5.81 \times 10^{-10}$ ), galvanic coupling between  $B_4C$  particles and the matrix is minor, thus making the potential shift easily explained by the mixed potential theory. For galvanic couples containing SS304, which is the cathode, increasing the content in noble  $B_4C$  particles makes more positive the composite potential, thus decreasing the potential difference between the MMC and SS304. Consequently, a small galvanic current is recorded between SS304 and AA1100-30 vol.%  $B_4C$  materials. On the other hand, when AA6061 is galvanically coupled to the MMC, AA6061 material is the anode and its dissolution is favored when it is coupled to the more noble MMC (30 vol.%  $B_4C$ ).

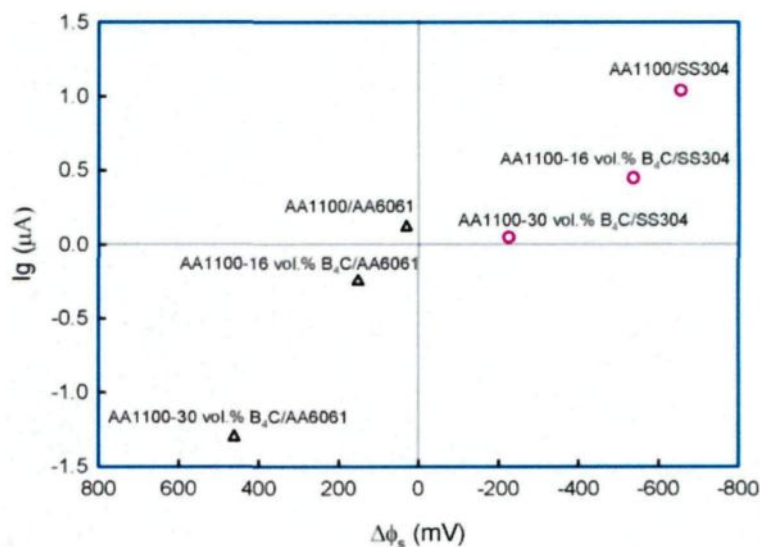


Figure 7.9 Average galvanic current density  $\overline{I_g}$  as function of  $\Delta\phi^s$  of uncoupled dissimilar materials in 2500 ppm B-containing  $H_3BO_3$  solution.

### 7.3.4 Effect of Area Ratio

The extent of galvanic corrosion between two or more dissimilar materials also depends on the effective area ratio of coupled dissimilar materials and other factors. [11, 14-17]

Results presented in previous sections were all carried out for an area ratio of  $A^C / A^A = 1$  (equal areas of anode  $A^A$  and cathode  $A^C$ ). In practice, the area ratio  $A^C / A^A$  is usually different from the unit. For this reason, the effect of area ratio on the galvanic current of AA1100-16 vol. % B<sub>4</sub>C/SS304 couple was studied in 3.5% NaCl and 2500 ppm B-containing H<sub>3</sub>BO<sub>3</sub> solutions. This material combination was selected since it is characterized by intermediate galvanic currents in both solutions. Two area ratios of  $A^C / A^A = 1:12.6$  and  $12.6:1$  were used, and the results were compared with previous results obtained for  $A^C / A^A = 1:1$ . For area ratios 1:1 or 1:12.6, the area of the SS304 electrode (cathode) was kept constant at 1 cm<sup>2</sup>, while for  $A^C / A^A = 12.6:1$  the area of SS304 electrode was 12.6 cm<sup>2</sup>.

Figure 7.10 and Figure 7.11 show  $I_g$  and  $\phi_g$ , respectively, as function of time for AA1100-16 vol. % B<sub>4</sub>C coupled to SS304 in 3.5% NaCl with different area ratios. It is observed that  $I_g$  is independent of area ratio for  $A^C / A^A = 1:1$  and  $1:12.6$ , but increases by about a factor of 12.6 for  $A^C / A^A = 12.6:1$ . This result shows that the galvanic current in NaCl solution is proportional to the cathode geometric area and further indicates that the galvanic corrosion in this couple is governed by the reduction reactions at the cathode surface (SS304). For its part, galvanic potential shows nearly the same values when the area ratio equals to 1:1 and 1:12.6, while it shifts toward positive direction from  $\sim -0.70$  V to  $\sim -0.42$  V when the area ratio is raised to 12.6:1. Under this condition, the system becomes more polarized toward the cathode, *i.e.* the active material potential shifts in the direction of anodic polarization, thus supporting the increased dissolution rate observed. The same

phenomenon was observed by Mansfeld and Kenkel [18, 19] when they studied the effect of area ratio on galvanic corrosion of Al alloys with dissimilar materials.

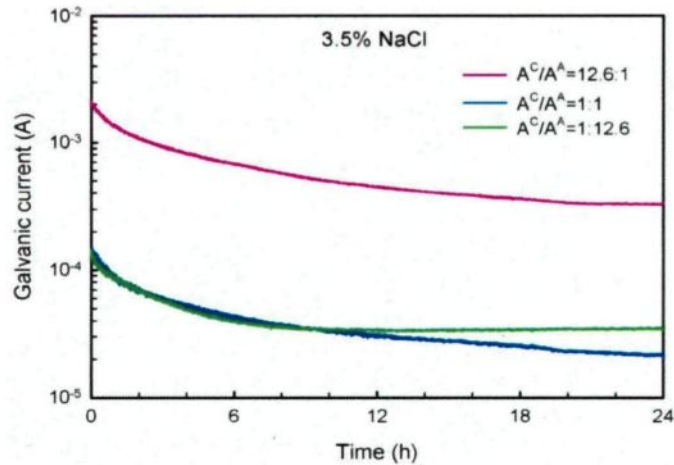


Figure 7.10 Galvanic current  $I_g$  as function of time and area ratio  $A^C / A^A$  for AA1100-16 vol. % B<sub>4</sub>C coupled to SS304 in 3.5% NaCl solution.

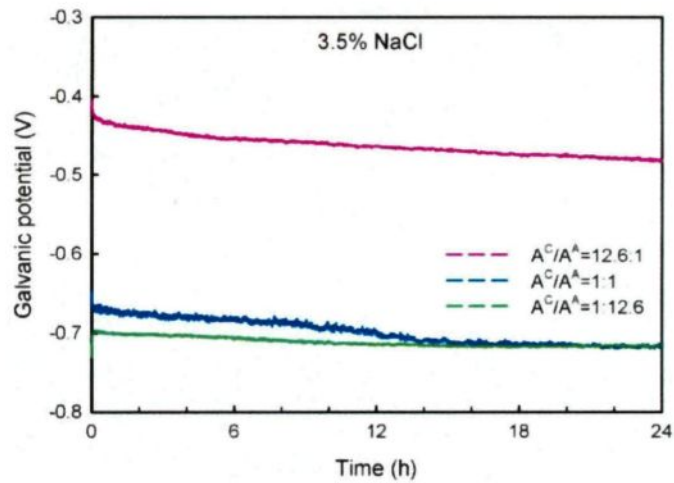


Figure 7.11 Galvanic potential  $\phi_g$  as function of time for AA1100-16 vol. % B<sub>4</sub>C/SS304 couple with different area ratios in 3.5% NaCl solution.

The relationship between galvanic current  $I_g$  and galvanic potential  $\phi_g$  is given by

Oldham and Mansfeld: [20]

$$I_g = I_{corr}^A \cdot \exp\left\{\frac{\phi_g - \phi_{corr}^A}{0.434b_a}\right\} - I_{corr}^C \cdot \exp\left\{\frac{\phi_{corr}^C - \phi_g}{0.434b_c}\right\} \quad (\text{Equation 7.1})$$

where  $I_{corr}^A$  and  $\phi_{corr}^A$  are the dissolution current and the corrosion potential, respectively, of the uncoupled anode, while  $b_c$  and  $b_a$  are the cathodic and anodic Tafel slopes obtained from the potentiodynamic polarization curve of uncoupled materials. In a previous study, [7] it is reported that the corrosion process of AA1100-16 vol.% B<sub>4</sub>C in NaCl solution is under oxygen diffusion controlled, so the cathodic Tafel slope  $b_c = \infty$ . Taking this condition into Equation 7.1, the relationship between galvanic current and galvanic potential  $\phi_g$  can be simplified as:

$$\ln\left(1 + \frac{I_g}{I_{corr}^A}\right) = \frac{\phi_g - \phi_{corr}^A}{0.434b_a} \quad (\text{Equation 7.2})$$

$$i.e. \phi_g = \phi_{corr}^A + b_a \log\left(1 + \frac{I_g}{I_{corr}^A}\right) \quad (\text{Equation 7.3})$$

In Equation 7.3, parameters  $\phi_{corr}^A$ ,  $b_a$  and  $I_{corr}^A$  are constant, thus galvanic potential  $\phi_g$  increases with  $I_g$ , which is proportional to the cathodic area. Results presented in Figure 7.10 and Figure 7.11 are in agreement with this relationship.

In the present research, to testify whether the galvanic corrosion of Al-B<sub>4</sub>C MMCs/SS304 couple is oxygen diffusion controlled or not, pure argon was purged into the 3.5% NaCl during the galvanic corrosion test, and the result is shown in Figure 7.12. It is observed that when argon is purged into the solution after 3 hours of immersion in open to air conditions, the galvanic current decreased immediately from 25  $\mu$ A to a negligible value, which clearly shows that the galvanic corrosion of AA1100-16 vol. % B<sub>4</sub>C/ SS304 couple is oxygen diffusion controlled.

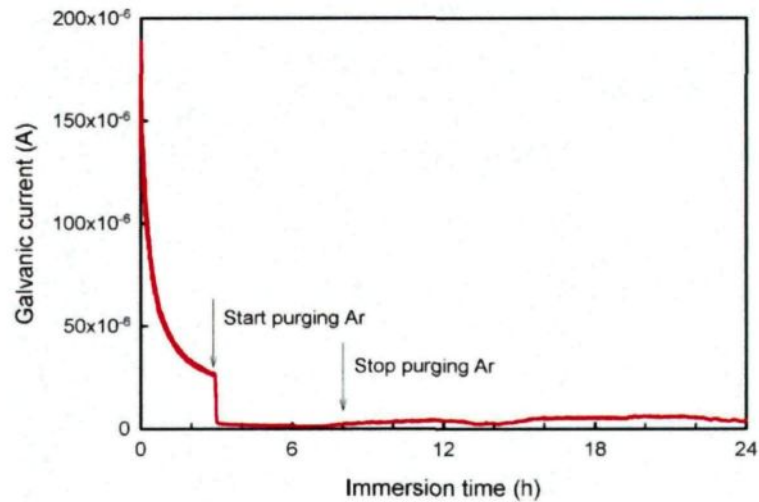


Figure 7.12 Galvanic current  $I_g$  as function of time with oxygen purging during the test for AA1100-16 vol. %  $B_4C$ /SS304 couple in 3.5% NaCl solution ( $A^C / A^A = 1:1$ ).

Formally, the anodic dissolution current  $I_a^A$  of the Al matrix in the composite equals to the sum of reduction currents at  $B_4C$  particles ( $I_c^A$ ) and SS304 surface ( $I_c^C$ ) (Equation 7.4). Also, the galvanic current  $I_g$  measured here equals the difference between anodic dissolution current  $I_a^A$  and reduction current  $I_c^A$  at the anode (Equation 7.5).

$$I_a^A = I_c^A + I_c^C \quad (\text{Equation 7.4})$$

$$I_g = I_a^A - I_c^A \quad (\text{Equation 7.5})$$

By summing up Equations 7.4 and 7.5, we obtain:

$$I_g = I_c^C \quad (\text{Equation 7.6})$$

Since the galvanic corrosion is oxygen diffusion controlled, the cathodic current density at the cathode equals to the oxygen diffusion current density at the cathode, which is a constant (see Equation 7.7).

$$i_c^C = i_{O_2}^{L,C} \quad (\text{Equation 7.7})$$

By combining Equations 7.6 and 7.7, we obtain:

$$I_g = I_c^C = i_{O_2}^{L,C} A^C \quad (\text{Equation 7.8})$$

Equation 7.6 shows that the galvanic current is controlled by the cathodic reaction at the cathode, which accords with the previous conclusion deduced from Figures 7.10 to 7.12. Equation 7.8 evidences that the galvanic current  $I_g$  is proportional to geometric area of the cathode electrode and this explains why  $I_g$  is independent of area ratio for  $A^C / A^A = 1:1$  and 1:12.6. By using Equation 7.8, the galvanic current densities with respect to anode  $i_g^A$  and cathode  $i_g^C$  are calculated as follow:

$$i_g^A = i_{O_2}^{L,C} \frac{A^C}{A^A} \quad (\text{Equation 7.9})$$

$$i_g^C = \frac{I_g}{A^C} = i_{O_2}^{L,C} = \text{const} \quad (\text{Equation 7.10})$$

According to Equation 7.9, the galvanic current density with respect to anode  $i_g^A$  is proportional to the area ratio  $A^C / A^A$ , which is qualitatively confirmed by data in Figure 7.13. Equation 7.10 shows that the galvanic current density with respect to cathode  $i_g^C$  is constant and independent of area ratio, which is proved in Figure 7.14.

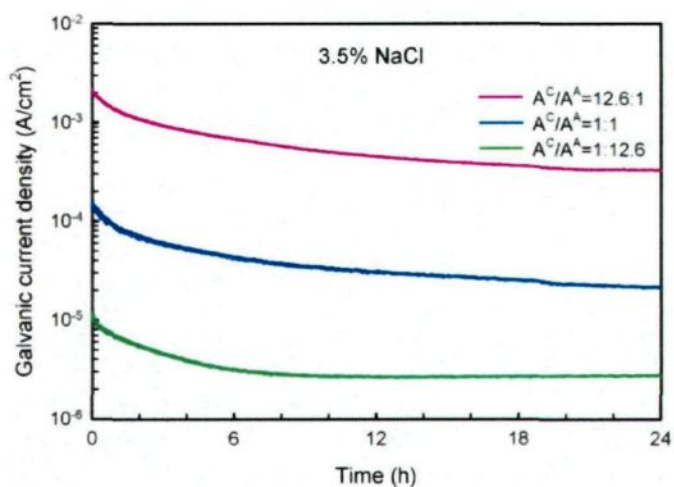


Figure 7.13 Galvanic current density  $i_g^A$  with respect to anode (AA1100-16 vol. % B<sub>4</sub>C) as function of time and area ratio for AA1100-16 vol. % B<sub>4</sub>C/SS304 couple in 3.5% NaCl solution.

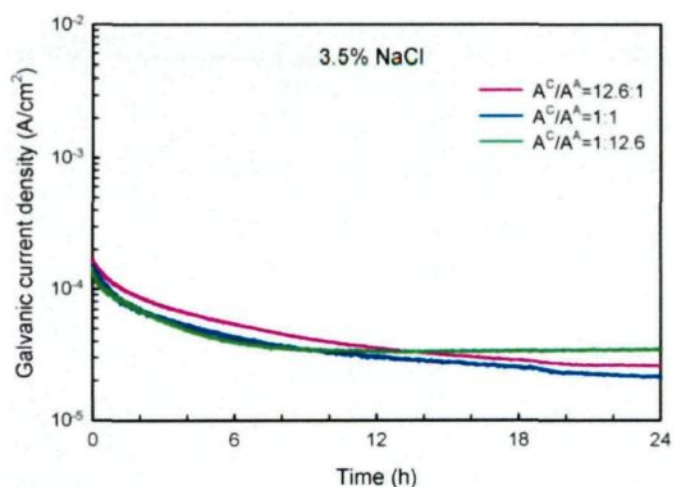


Figure 7.14 Galvanic current density  $i_g^C$  with respect to cathode (SS304) as function of time and area ratio for AA1100-16 vol. % B<sub>4</sub>C/ SS304 couple in 3.5% NaCl solution.

In Figure 7.15, when the average  $i_g^A$  is plotted as function of area ratio in a log-log configuration, a linear regression characterized by a slope close to one (*i.e.* 1.02) can be drawn. From the intersection point between the regression curve and the y-axis, a value of  $41.7 \mu\text{A}/\text{cm}^2$  was determined for the  $i_{O_2}^{L,C}$  parameter, which is virtually equals to the galvanic corrosion current density with respect to the cathode size  $i_g^C$  calculated for the

AA1100-16 vol. % B<sub>4</sub>C / SS304 couple in 3.5% NaCl solution (38.1  $\mu\text{A}/\text{cm}^2$ , as shown in Figure 7.14).

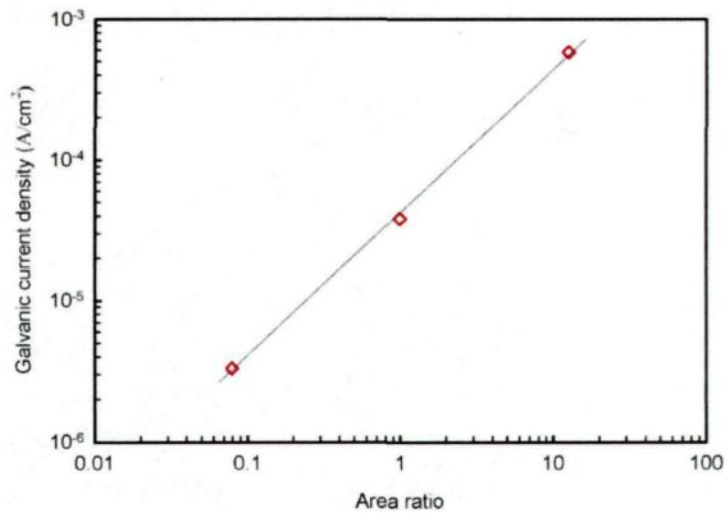


Figure 7.15 Dependence of  $i_s^A$  on area ratio  $A^C/A^A$  in 3.5% NaCl solution.

According to Equation 7.1, the total dissolution current density of the anode  $i_a^A$  could be derived as:

$$i_a^A = i_{O_2}^{L,A} + i_{O_2}^{L,C} \frac{A^C}{A^A} \quad (\text{Equation 7.12})$$

$i_{O_2}^{L,A}$  is the limiting oxygen diffusion current to the anode and its value is 8.39  $\mu\text{A}/\text{cm}^2$ , which is reported in a previous study. [4]

The corrosion rate  $r_A$  could be calculated by using Faraday's law

$$m = \frac{Q}{F} \frac{M}{z} \quad (\text{Equation 7.13})$$

$$r_A = \frac{i_a^A}{F} \frac{M}{z} \quad (\text{Equation 7.14})$$

where  $m$  is the mass of the dissolved Al in gram,  $Q$  is the total electric charge passed through the composite (C),  $F$  is the Faradic constant ( $96485 \text{ C mol}^{-1}$ ),  $M$  is the molar mass of Al ( $26.98 \text{ g.mol}^{-1}$ ),  $z$  is the valency number of  $\text{Al}^{3+}$  (3). The dependence of corrosion rate  $r_A$  on area ratio is plotted in Figure 7.16. As observed, the corrosion rate is linearly related to the cathode-to-anode ratio,  $A^C / A^A$ .

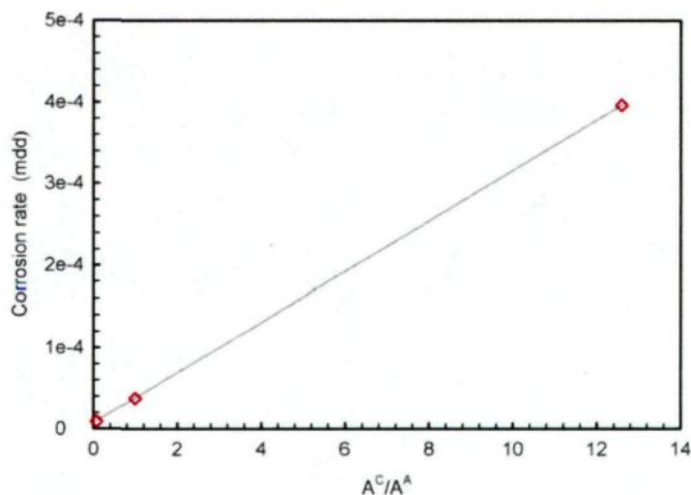


Figure 7.16 Dependence of corrosion rate  $r_A$  of AA1100-16 vol. %  $\text{B}_4\text{C}$  on area ratio  $A^C/A^A$  in 3.5% NaCl solution.

Figure 7.17 plots the galvanic current  $I_g$  as function of time and area ratio in  $\text{H}_3\text{BO}_3$  solution. It is observed that  $I_g$  is also independent of area ratio when  $A^C / A^A$  equals to 1:1 or 12.6:1. However, when the area ratio is increased to 12.6:1, the galvanic current increases by a factor of 2.0 rather than 12.6 as determined in NaCl solution. These results indicate that oxygen reduction reaction at cathode controls the galvanic corrosion in  $\text{H}_3\text{BO}_3$  solution, but the effect of area ratio is impaired by the weakness of boric acid ( $K_a = 5.81 \times 10^{-10}$ ). Figure 7.18 shows the time behavior of galvanic potential of AA1100-16 vol.%  $\text{B}_4\text{C}/\text{SS304}$  couple with different area ratios in  $\text{H}_3\text{BO}_3$  solution. It is observed that the

galvanic potential of the couple with area ratio of 12.6:1 is much nobler than that of couples with 1:1 and 1:12.6 ratios (also observed in NaCl solution). The galvanic potential increases during the first 6 hours for the couples with area ratios of 1:1 and 1:12.6, while in the first 3 hours for the couple with area ratio of 12.6:1. This increase in potential is found to correspond to the galvanic current drop, which means that passivation behavior occurs in this solution.

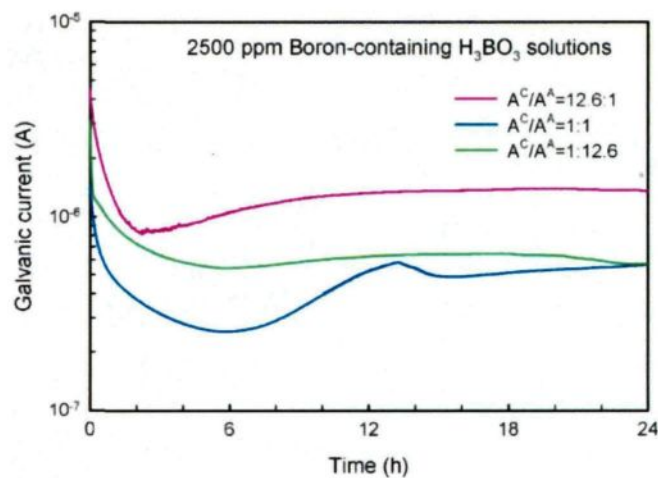


Figure 7.17 Galvanic current  $I_g$  as function of time and area ratio  $A^C / A^A$  for Al-16 vol. %  $B_4C$  coupled to SS304 in 2500 ppm B-containing  $H_3BO_3$  solution.

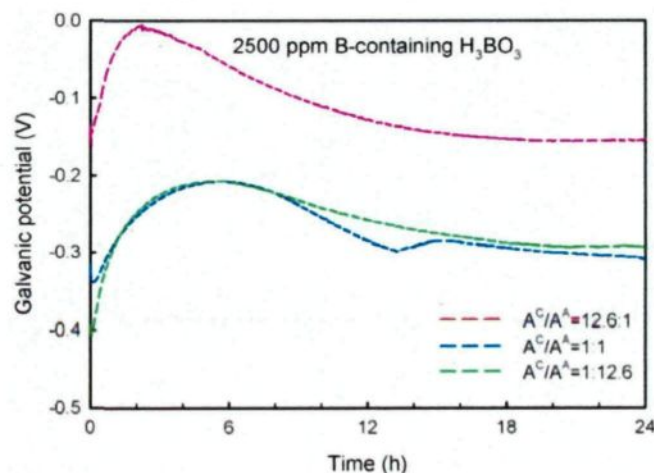


Figure 7.18 Galvanic potential as function of time for Al-16 vol. %  $B_4C$ /SS304 couple with different area ratios in 2500 ppm B-containing  $H_3BO_3$  solution.

## 7.4 Conclusions

As neutron absorber materials used in the nuclear industry, Al-B<sub>4</sub>C composites are often assembled to structural materials AA6061 aluminum alloy or SS304 stainless steel. Due to the combination of dissimilar materials, galvanic corrosion is likely to occur, especially in the wet storage application. The present study investigated for the first time the galvanic corrosion between Al-B<sub>4</sub>C composite with different B<sub>4</sub>C levels and AA6061 or SS304 in NaCl and H<sub>3</sub>BO<sub>3</sub> solutions using a zero resistance ammeter (ZRA). The influence of area ratio of assembled dissimilar materials was also determined. Based on the results obtained, the following conclusions could be drawn:

1. In NaCl solution, whether it is coupled to SS304 or AA6061, the AA1100-B<sub>4</sub>C composites or the base alloy always acts as an anode and galvanic current increases with increasing B<sub>4</sub>C content in the composite. For the same investigated material, a higher galvanic current is obtained when it is coupled to SS304.
2. In H<sub>3</sub>BO<sub>3</sub> solution, when it is coupled to SS304, the AA1100-B<sub>4</sub>C composites or the base alloy acts as an anode and galvanic current decreases linearly with increasing B<sub>4</sub>C content in the composite. However, when it is coupled to AA6061, the AA1100-16 vol.% B<sub>4</sub>C and AA1100-30 vol.% B<sub>4</sub>C composites act as a cathode, thus the measured galvanic current is related with the dissolution of AA6061. With increased B<sub>4</sub>C content in the composites (cathode), the galvanic current increases.
3. In NaCl solution, galvanic corrosion is controlled by oxygen diffusion at cathode (SS304). Consequently, the galvanic current measured in NaCl solution is

proportional to the cathodic geometric area. The galvanic current density with respect to the composite (anode)  $i_g^A$  increases linearly with the area ratio of  $A^C/A^A$  and the galvanic current density with respect to SS304 (cathode), is constant in spite of variation of area ratio. In addition, the galvanic potential shifts in the positive direction with galvanic current increasing.

4. In  $H_3BO_3$  solution, galvanic corrosion is also controlled by oxygen diffusion at cathode (SS304). However, the galvanic current is appreciably smaller than that in NaCl solution and is not proportional to the cathodic geometric area. In addition, passivation occurs on the composite surface in  $H_3BO_3$  solution.

## References

- [1] X.-G. Chen, "Application of Al-B<sub>4</sub>C Metal Matrix Composites in the Nuclear Industry for Neutron Absorber Materials", in: *Proceedings of the Symposium on Solidification Processing of Metal Matrix Composites*, W.H. Hunt and N. Gupta (Eds.), TMS, 2006, pp. 343-350.
- [2] X.-G. Chen, R. Hark, "Development of Al-30%B<sub>4</sub>C Metal Matrix Composites for Neutron Absorber Material", in: *Proceedings of Aluminium Alloys: Fabrication, Characterization and Applications* W. Yin and S.K. Das (Eds.), TMS, 2008, pp. 3-9.
- [3] G. Bonnet, V. Rohr, X.-G. Chen, J.L. Bernier, R. Chiocca, H. Issard, "Use of Alcan's Al-B<sub>4</sub>C Metal Matrix Composites as Neutron Absorber Material in TN International's Transportation and Storage Casks", *Packaging, Transport, Storage and Security of Radioactive Material*, 20 (2009) 98-102.
- [4] Y. Han, D. Gallant, X.-G. Chen, "Corrosion Behavior of Al-B<sub>4</sub>C Metal Matrix Composites in  $H_3BO_3$ ,  $K_2SO_4$  and NaCl Solutions", in: *Light Metal Proceedings*, M. Fafard and G. Dufour (Eds.), MetSoc, 2011, pp. 415-425.
- [5] Z. Zhang, X.G. Chen, A. Charette, "Fluidity and Microstructure of An Al-10% B<sub>4</sub>C Composite", *Journal of Materials Science*, 44 (2009) 492-501.
- [6] Z. Zhang, K. Fortin, A. Charette, X.G. Chen, "Effect of Titanium on Microstructure and Fluidity of Al-B<sub>4</sub>C Composites", *Journal of Materials Science*, 46 (2011) 3176-3185.

- [7] Y. Han, D. Gallant, X.-G. Chen, Corrosion Characterization of Al-B<sub>4</sub>C Metal Matrix Composites in NaCl Solutions, submitted to *Electrochimica Acta*, 2012.
- [8] Y.L. Cheng, Z.H. Chen, H.L. Wu, H.M. Wang, "The Corrosion Behaviour of the Aluminum Alloy 7075/SiCp Metal Matrix Composite Prepared by Spray Deposition", *Materials and Corrosion*, 58 (2007) 280-284.
- [9] S.D. Cramer, J. B.S. Covino, *ASM Handbook, Vol.13A: Corrosion: Fundamentals, Testing and Protection*, ASM International, 2003.
- [10] R. Moshrefi, M.G. Mahjani, A. Ehsani, M. Jafarian, "A study of the galvanic corrosion of titanium/L 316 stainless steel in artificial seawater using electrochemical noise (EN) measurements and electrochemical impedance spectroscopy (EIS)", *Anti-Corrosion Methods and Materials*, 58 (2011) 250-257.
- [11] Z.F. Yin, M.L. Yan, Z.Q. Bai, W.Z. Zhao, W.J. Zhou, "Galvanic Corrosion Associated With SM 80SS Steel and Ni-Based Alloy G3 Couples in NaCl Solution", *Electrochimica Acta*, 53 (2008) 6285-6292.
- [12] G. Song, B. Johannesson, S. Hapugoda, D. StJohn, "Galvanic Corrosion of Magnesium Alloy AZ91D in Contact With an Aluminium Alloy, Steel and Zinc", *Corrosion Science*, 46 (2004) 955-977.
- [13] Y. Han, D. Gallant, X.-G. Chen, "Investigation on Corrosion Behavior of the Al-B<sub>4</sub>C Metal Matrix Composite in a Mildly Oxidizing Aqueous Environment", *Corrosion*, 67 (2011) No. 115005.
- [14] S. Fangteng, E.A. Charles, "A Theoretical Approach to Galvanic Corrosion, Allowing for Cathode Dissolution", *Corrosion Science*, 28 (1988) 649-655.
- [15] R. Francis, "Galvanic Corrosion of High Alloy Stainless Steels in Sea Water", *British Corrosion Journal*, 29 (1994) 53-57.
- [16] F. Bellucci, "Galvanic Corrosion between Nonmetallic Composites and Metals. I. Effect of Metal and of Temperature", *Corrosion*, 47 (1991) 808-819.
- [17] F. Bellucci, "Galvanic Corrosion Between Nonmetallic Composites and Metals II. Effect of Area Ratio and Environmental Degradation", *Corrosion*, 48 (1992) 281-291.
- [18] F. Mansfeld, J.V. Kenkel, "Galvanic Corrosion of Al Alloys-III. The Effect of Area Ratio", *Corrosion Science*, 15 (1975) 239-250.
- [19] F. Mansfeld, "Galvanic Corrosion of Al Alloys", *Werkstoffe und Korrosion*, 25 (1974) 578-586.
- [20] K.B. Oldham, F. Mansfeld, "Corrosion Rates From Polarization Curves: A New Method", *Corrosion Science*, 13 (1973) 813-819.

## **CHAPTER 8**

### **CONCLUSIONS & RECOMMENDATIONS FOR FUTURE WORK**

## CHAPTER 8

### CONCLUSIONS & RECOMMENDATIONS FOR FUTURE WORK

#### 8.1 Conclusions

This research was carried out in order to study the corrosion behavior of Al-B<sub>4</sub>C MMCs. The corrosion susceptibility of Al-B<sub>4</sub>C metal matrix composites in 2500 ppm boron-containing H<sub>3</sub>BO<sub>3</sub> was studied referring to that in 0.5 M K<sub>2</sub>SO<sub>4</sub> and 35 g/L NaCl solutions. The effect of incorporated B<sub>4</sub>C particles in the composite was also studied. Since Al-B<sub>4</sub>C MMCs were corroded severely in NaCl solution, its corrosion characterization, corrosion mechanism and corrosion inhibition by benzotriazole was studied systematically for the first time by using potentiodynamic polarization (PDP) and electrochemical impedance spectroscopy (EIS) techniques. Besides, the corrosion product of the composite in 0.5 M K<sub>2</sub>SO<sub>4</sub> solution was identified in this study by employing IRRAS and XPS techniques.

AA1100-B<sub>4</sub>C MMCs are non-structural neutron absorber materials. As a result, this material is often assembled to structural materials AA6061 or SS304 in real application, which results in the galvanic coupling of the composite and AA6061 or SS304, accelerating the corrosion of less noble material. Accordingly, the galvanic corrosion of Al-B<sub>4</sub>C MMCs associated with AA6061 and SS304 in 35g/L NaCl and 2500 ppm boron-containing H<sub>3</sub>BO<sub>3</sub>

solutions were studied by using zero resistance ammetry techniques. Based on results from Chapter 4 to Chapter 7, the following conclusions could be drawn:

***Part 1: Corrosion susceptibility of Al-B<sub>4</sub>C metal matrix composite in 35g/L NaCl, 0.5 M K<sub>2</sub>SO<sub>4</sub> and 2500 ppm boron-containing H<sub>3</sub>BO<sub>3</sub>solutions***

- (1) Al-B<sub>4</sub>C metal matrix composites and base alloy are most corroded in 35 g/L NaCl solution, while least corroded in 2500 ppm boron-containing H<sub>3</sub>BO<sub>3</sub>. In NaCl solution, pitting occurs and preferably initiated at Al/B<sub>4</sub>C interfaces for the composite, while preferentially initiated at Al/Fe intermetallics interfaces for the base alloy. In other two solutions, (*i.e.* 0.5 M K<sub>2</sub>SO<sub>4</sub> and 2500 ppm boron-containing H<sub>3</sub>BO<sub>3</sub>), no pits were observed.
- (2) Increasing the volume fraction of B<sub>4</sub>C particles in the composite leads to a decrease in its corrosion resistance.

***Part 2: Corrosion behavior of Al-B<sub>4</sub>C metal matrix composite in 0.5 M K<sub>2</sub>SO<sub>4</sub> solution***

- (3) The B<sub>4</sub>C particles show a cathodic character with respect to the peripheral matrix. The associated anodic response is the dissolution of the aluminum matrix and the TiB<sub>2</sub> layer. The consequent corrosion product is bayerite Al(OH)<sub>3</sub>.
- (4) Surface defects such as porosities can significantly reduce the corrosion resistance of the composite and change the corrosion impedance spectra from one to two capacitive loops.

***Part 3: Corrosion inhibition of Al-B<sub>4</sub>C metal matrix composite in 3.5g/L NaCl solution by benzotriazole***

- (5) BTAH is an efficient corrosion inhibitor for the Al-B<sub>4</sub>C composites in 3.5g/L NaCl solution, and its inhibition efficiency increases with its concentration.
- (6) B<sub>4</sub>C particles play a positive role on the inhibition efficiency of benzotriazole for the composite in NaCl solution. Increasing B<sub>4</sub>C volume fraction in the composite results in a linear increase in the corrosion inhibition efficiency.
- (7) The corrosion inhibition efficiency of benzotriazole on AA1100-16 vol.% B<sub>4</sub>C composite in NaCl solution is influenced by the immersion time. Within the first 18 hours, IE increases progressively with the immersion time, attaining the maximum value of 90.3%, and then gradually decreases to 40.1% with immersion time prolonged to 120 hours.
- (8) Benzotriazole is an inhibitor with cathodic character and it inhibits the corrosion of the composite by adsorbing physically onto the B<sub>4</sub>C particles at the composite surface. The adsorption behavior obeys a Freundlich adsorption isotherm.

***Part 4: Galvanic corrosion associated with Al-B<sub>4</sub>C MMCs/AA6061 couples and Al-B<sub>4</sub>C MMCs/SS304 in 35 g/L NaCl and 2500 ppm boron-containing H<sub>3</sub>BO<sub>3</sub> solutions.***

- (9) In NaCl solution, whether it is coupled to SS304 or AA6061, the composite or base alloy always acts as an anode and galvanic current increases with increasing B<sub>4</sub>C content in the composite. For the same investigated material, a higher galvanic current is obtained when it is coupled to SS304.
- (10) In H<sub>3</sub>BO<sub>3</sub> solution, when it is coupled to SS304, the composite or base alloy acts as an anode and galvanic current decreases linearly with increasing B<sub>4</sub>C content in

the composite. However, when it is coupled to AA6061, composites AA1100-16 vol.% B<sub>4</sub>C and AA1100-30 vol.% B<sub>4</sub>C act as a cathode, thus the measured galvanic current is related with the dissolution of AA6061. With B<sub>4</sub>C content increasing in the composite (cathode), the galvanic current increases.

- (11) In NaCl solution, galvanic corrosion is controlled by oxygen diffusion at cathode (SS304). Consequently, the galvanic current measured in NaCl solution is proportional to the cathodic geometric area. The galvanic current density with respect to the composite (anode)  $i_g^A$  increases linearly with the area ratio of  $A^C/A^A$  and the galvanic current density with respect to SS304 (cathode), is constant in spite of variation of area ratio. In addition, the galvanic potential shifts in the positive direction with galvanic current increasing.
- (12) In H<sub>3</sub>BO<sub>3</sub> solution, even the galvanic corrosion is controlled by oxygen diffusion at cathode (SS304), the galvanic current is appreciably smaller than that in NaCl solution and is not proportional to the cathodic geometric area. In addition, passivation occurs on the composite surface in H<sub>3</sub>BO<sub>3</sub> solution.

## 8.2 Recommendations for Future Works

In the present study, the corrosion behavior of Al-B<sub>4</sub>C composites in three solutions (*i.e.* 2500 ppm boron-containing H<sub>3</sub>BO<sub>3</sub>, 0.5 M K<sub>2</sub>SO<sub>4</sub> and 35 g/L NaCl) was investigated. Consequently, the corrosion inhibition of the composite in NaCl solution was studied. Then the corrosion mechanism of the composite in mildly corrosive K<sub>2</sub>SO<sub>4</sub> solution was also investigated. The galvanic corrosion associated with AA1100-B<sub>4</sub>C MMCs/SS304 and

AA1100-B<sub>4</sub>C MMCs/AA6061 couples was also examined. However, AA1100-B<sub>4</sub>C composites are immersed in boric acid at elevated temperature in the real situation, which stimulates the corrosion of the composite and SS304 or AA6061 and augments the corrosion rate of both materials. Accordingly, the following research work is recommended:

- (1) Studying the corrosion behavior of Al-B<sub>4</sub>C composites in boric acid at elevated temperature;
- (2) Investigating the galvanic corrosion associated with Al-B<sub>4</sub>C MMCs/SS304 and Al-B<sub>4</sub>C MMCs/AA6061 couples in boric acid at elevated temperature.